MOLECULAR MRI OF NEUROVASCULAR INFLAMMATION AND ANGIOGENESIS

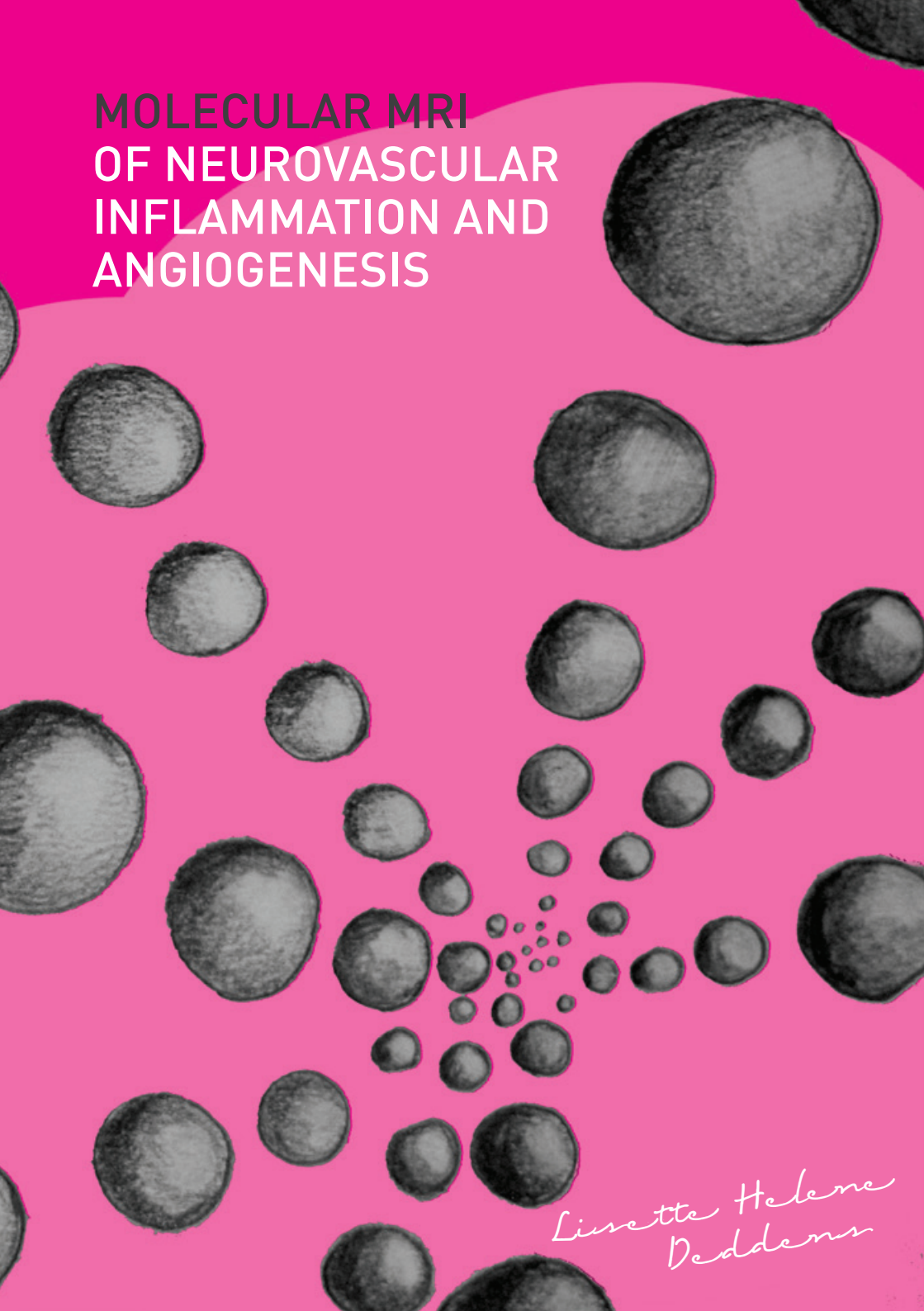

Lisette Helene Deddens

MOLECULAR MRI OF NEUROVASCULAR INFLAMMATION AND ANGIOGENESIS

Moleculaire MRI van neurovasculaire inflammatie en angiogenese
(met een samenvatting in het Nederlands)

PROEFSCHRIFT

ter verkrijging van de graad van doctor
aan de Universiteit Utrecht op gezag
van de rector magnificus, prof.dr. G.J.
van der Zwaan, ingevolge het besluit
van het college voor promoties in het
openbaar te verdedigen op donderdag
28 maart 2013 des middags te 2.30 uur

door

Lisette Helene Deddens

geboren op 3 juli 1983 te Enkhuizen.

Promotoren prof.dr.ir. M.A. Viergever
prof.dr. H.E. de Vries
Co-promotor dr. R.M. Dijkhuizen

Dit proefschrift werd (mede) mogelijk gemaakt met financiële steun van Stichting De Drie Lichten.

Love is patient,
love is kind. It does not envy,
it does not boast,
it is not proud. It does not
dishonor others, it is
not self-seeking,
it is not easily angered,
it keeps no record of wrongs.
Love does not delight in evil
but rejoices with
the truth. It always
protects, always **trusts**,
always **hopes**, always
perseveres.
Love never fails.

COLOFON

ISBN:

Printed by: GVO drukkers & vormgevers BV
Layout: Willemieke Slingerland
Illustrations: Samantha Deddens-Van Dalen

The research described in this thesis was funded by The Netherlands Organization for Scientific Research (NWO; VIDI 917.76.347), and the European Stroke Network (ESN; EU FP7/2007–2013: 201024, 202213).

TABLE OF CONTENTS

INTRODUCTION

Adapted from:
Lisette H. Deddens, Geralda A.F. Van Tilborg, Willem J.M. Mulder, Helga E. De Vries and Rick M. Dijkhuizen.
Imaging neuroinflammation after stroke: current status of cellular and molecular MRI strategies.
Cerebrovasc Dis **2012** 33:392-402

Peter R. Seevinck, Lisette H. Deddens and Rick M. Dijkhuizen.
Magnetic resonance imaging of brain angiogenesis after stroke.
Angiogenesis **2010** 13:101-111

01

1.1 MOLECULAR IMAGING

Molecular imaging allows direct monitoring and recording of the spatiotemporal distribution of molecular or cellular processes *in vivo*, and can give unique insights in fundamental biochemical and biological processes. Furthermore, it is also suitable for diagnostic and therapeutic applications [1]. Molecular imaging can be accomplished with a variety of imaging techniques, such as optical imaging, ultrasound, positron emission tomography (PET), single-photon emission computed tomography (SPECT), computed tomography (CT) and magnetic resonance imaging (MRI) [2]. These imaging techniques typically make a trade-off between resolution and sensitivity **(Figure 1.1)**.

CT provides good structural information, but with a relative low detection sensitivity and soft-tissue contrast. In combination with contrast-generating gold nanoparticles, CT can be used for molecular imaging purposes [3]. However, excessive radiation hampers the use of CT for extensive longitudinal studies.

Ultrasound provides proper spatial resolution, but the field of view is limited to the probe location and penetration depth, and with a basic ultrasound set-up, only 2D images are obtained from the target of interest. The development of targeted microbubbles has recently added this technique to the list of imaging techniques for molecular imaging [4].

On the other end of the spectrum are **PET** and **SPECT**, which provide high sensitivity, but accompanied with low spatial information. Molecular imaging with both PET and SPECT combined with radioactive tracers, has been implemented in the clinic for diagnostic purposes [5], nevertheless, high radiation dosage often limits their use for longitudinal studies.

Optical imaging encompasses fluorescence imaging and bioluminescence imaging methods, and renders a high sensitivity. With the use of near-infrared fluorescence, the penetration depth of optical imaging of tissue has become much deeper, in addition to a further improved sensitivity or structural contrast [6]. Molecular optical imaging is mainly used in basic research, for example to study target expression with use of reporter genes in transgenic animals [7]. These transgenic animals then express an optical probe when the reporter gene is encoded in relation to the target of interest, giving rise to signal from a fluorescent dye or luciferin-induced bioluminescence from specific cells. When induced in rodents, the penetration depth of the emitted probe is sufficient to perform a whole body scan. Other types of molecular optical imaging are restricted to *post mortem* scanning of excised tissue, or scanning of tissue locations close to the surface.

MRI is a technique that can provide proper spatial resolution with adequate sensitivity. Furthermore, MRI is a non-invasive technique that is not hampered by tissue penetration limits or restricted to 2D image acquisition, which can be used for extensive longitudinal studies [8]. MRI provides excellent soft-tissue contrast, can reach decent spatiatemporal resolutions, and provides good contrast agent sensitivity (single particle detection). Molecular MRI application is the principal topic of this thesis, and its basics will be discussed in the next paragraph.

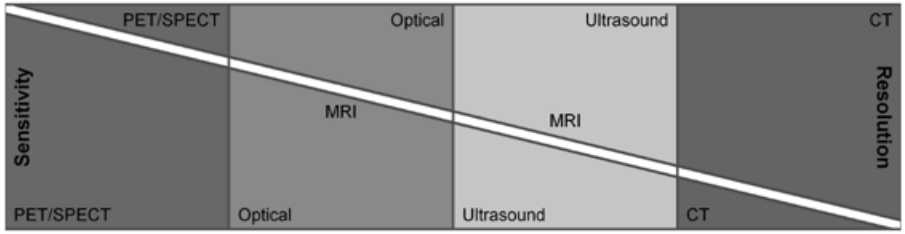

Figure 1.1
Schematic overview of relative sensitivity and resolution of different imaging techniques.

1.2 MRI

MRI, magnetic resonance imaging, is based on the phenomenon that nuclei which contain odd numbers of protons and/or neutrons have an intrinsic magnetic moment and spin angular momentum, i.e., a non-zero spin. When a group of these non-zero spins is placed in a magnetic field, they align to the magnetic field. Due to the occupation of higher and lower energy levels, there is a net magnetization vector. This net magnetization vector from a group of spins resonates in the applied magnetic field, which is the basis of the MR signal [9-10]. Even though a nucleus may posses an intrinsic magnetic moment, and would therefore be suitable to use for MRI, its feasibility is dependent on the natural abundance and biological availability of the isotope **(Table 1.1)** [11-12]. Currently, only ^{1}H MRI is used in the clinic. The other isotopes listed in **Table 1.1** have been applied in research and might advance to clinical applications in the future as well.

Nuclei	Natural Abundance (%)	Biological Abundance (%)
^{1}H	99.985	63
^{13}C	1.11	0.10
^{19}F	100	0
^{23}Na	100	0.041
^{31}P	100	0.24

Table 1.1
Nuclei that posses an intrinsic magnetic moment with their natural and biological abundance listed.

An MR detectable signal change can be measured when a radiofrequency (RF) pulse is applied. At equilibrium, the net magnetization vector of a group of protons aligns along the applied magnetic field in the longitudinal plane, which is referred to as the equilibrium magnetization. By applying an RF pulse, the net magnetization vector can be flipped from the longitudinal plane to the transverse plane, after which it relaxes back to its original longitudinal, equilibrium magnetization. This relaxation process is described by two parameters, being spin-lattice relaxation time (T_1) and spin-spin relaxation time ($T_2^{(*)}$). Spin-lattice relaxation time, T_1, is the time in which the longitudinal relaxation recovers, which is determined by the interaction of water protons with their surrounding. Spin-spin relaxation time, $T_2^{(*)}$, describes the decay of the transverse magnetization towards equilibrium. This decay in transverse magnetization is caused by dephasing of the signal as every spin experiences a slightly different magnetic field. This dephasing is caused by intramolecular spin-spin interactions (pure T_2) and variations in the applied magnetic field (inhomogeneous T_2 effect). The combined effect of T_2 and inhomogeneous T_2 effects are described by T_2*. T_1, T_2 and T_2* are time constants (expressed in s), and follow the rule $T_1 >> T_2 >> T_2$*. Local differences in these parameters can be exploited to generate tissue contrast as displayed in **Figure 1.2**, which shows typical MR images of a unilaterally ischemic mouse brain based on T_1-weighting **(Figure 1.2A)**, T_2-weighting **(Figure 1.2B)** and T_2*-weighting **(Figure 1.2C)**.

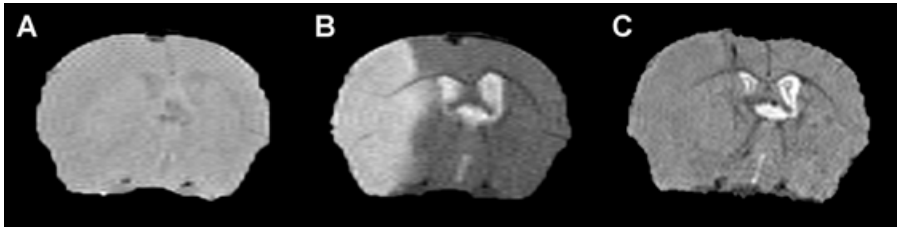

Figure 1.2 *

*** Figure 1.2**
Differences in tissue contrast from MR relaxation times T_1, T_2 and T_2*, as demonstrated on MR images of a unilaterally ischemic mouse brain based on **(A)** T_1-weighting, **(B)** T_2-weighting and **(C)** T_2*-weighting.

In the last two decades, MRI has proven to be a valuable tool to investigate the spatio-temporal profile of pathology-induced changes, mainly attributable to its capability to longitudinally evaluate a wide spectrum of structural and functional tissue characteristics. This versatility originates from the fact that contrast in MR images is dependent on intrinsic, biophysical tissue properties such as proton density, inter- and intramolecular magnetic interactions, oxygenation state, magnetic susceptibility, diffusion, perfusion and flow. These endogenous tissue characteristics influence the MRI signal by their effect on MR relaxation times (T_1, T_2 and T_2*) and water proton mobility, which can be exploited to generate image contrast. Additionally, exogenous contrast agents can be applied to enhance endogenous contrast-generating mechanisms. This can improve anatomical and/or physiological distinction, and may allow detection of otherwise indiscernible factors.

1.3 MR CONTRAST AGENTS

MR contrast agents reduce the intrinsic longitudinal (T_1) and transverse ($T_2^{(*)}$) relaxation times of its surrounding tissue, thereby generating localized hyperintense or hypointense areas on T_1- or $T_2^{(*)}$-weighted MR images, respectively. The potency of a contrast agent to change the signal intensity on MR images is represented by its relaxivities r_1, r_2 and r_2*, expressed in mM^{-1} s^{-1}. In general, the ratio between these relaxivity values determines whether a contrast agent is most suitable for T_1- or $T_2^{(*)}$-weighted imaging, i.e., agents with an r_2/r_1 ratio between 1-2 typically induce strong contrast effects on T_1-weighted images, while agents with higher r_2/r_1 ratios induce most tissue contrast on $T_2^{(*)}$-weighted images [13]. The most commonly applied clinical MR contrast agents are the FDA- and EMEA-approved low molecular weight paramagnetic gadolinium (Gd) polyaminocarboxylate chelates, e.g., Gd-DTPA and Gd-DOTA [14-15]. These agents have a r_2/r_1 ratio between 1-2 and are therefore commonly applied to induce hyperintense signals on T_1-weighted MR images **(Figure 1.3A)**. Another important class of contrast agents are formed by superparamagnetic iron oxide particles, which come in a wide range of sizes and a variety of coatings [16].

The popularity of these agents, typically with high r_2/r_1 ratios, is predominantly based on their biocompatibility [17] and their capacity to efficiently disturb local magnetic fields, thereby generating localized hypointense areas on T_2- and T_2*-weighted MR images **(Figure 1.3B)** to an extent that generally increases with particle concentration, particle size and external magnetic field strength [18].

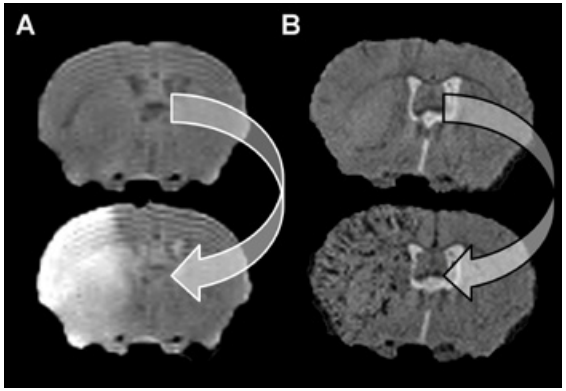

Figure 1.3
Contrast agents allow detection of otherwise indiscernable factors, such as **(A)** blood-brain barrier permeability from leakage of an intravenously injected T_1-type contrast agent (i.e., Gd-complex), and **(B)** neurovascular inflammation from binding of an intravenously injected $T_2^{(*)}$-type contrast agent (i.e., iron oxide).

To increase the efficiency of MR contrast agents, nano- or microformulations can be manufactured with a high payload of contrast agent per unit. An important example of such particles are micron-sized particles of iron oxide (MPIO), with sizes in the micrometer range, containing very high amounts of iron oxide. Commercially available polystyrene/divinylbenzene MPIO, such as employed by Hoyte et al [19], are adequate for investigations in animal models. But these particles are inert which excludes their application in humans. Recent developments in the synthesis of biodegradable MPIO may potentially provide a clinically applicable alternative [20].

Another established platform for increased contrast payload is available in the form of lipid-based nanoparticles [21]. Lipid-based nanoparticles, such as micelles, emulsions or liposomes, are comprised of a biocompatible lipid mono- or bilayer coating that encapsulates either an aqueous or hydrophilic core **(Figure 1.4)**. The composition of this lipid coating, as well as the relative amount of additionally incorporated hydrophobic compounds (e.g., oil), define the morphology, size and blood half-life of the particle [22-23]. This offers an extremely versatile and tunable compound for a wide variety of applications, ranging from preclinical cellular and molecular imaging studies to drug delivery in patients [24]. For MRI purposes, large quantaties of Gd-containing lipids can be incorporated in the nanoparticle's lipid (bi)layer [25], or alternatively, hydrophobic iron oxide nanocrystals can be encapsulated in the nanoparticle's core [26-27]. Moreover, additional inclusion of fluorescent moieties [28] or PET/SPECT tracers [29] in the lipid (bi)layer, or hydrophobic particles, such as gold particles [30] and quantum dots [31], in the nanoparticle core, extends the utility of this platform to multimodal imaging set-ups [32].

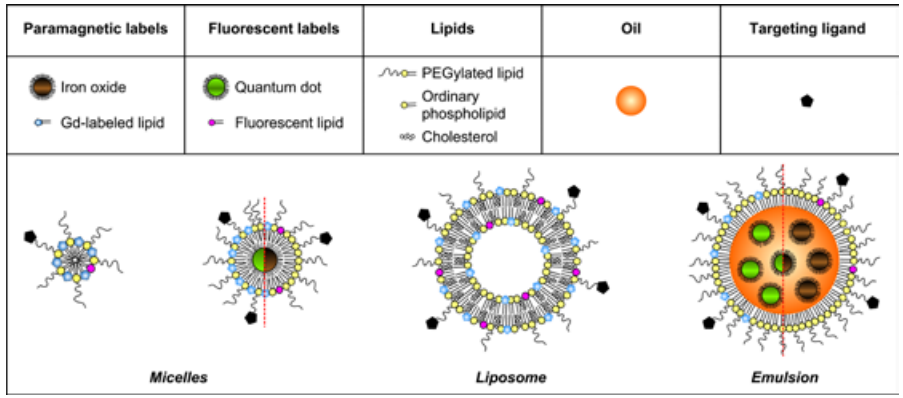

Figure 1.4
Schematic representation of different types of lipid-coated nanoparticles with a variety of possible imaging entities, including MRI labels (Gd-labeled lipids or iron oxide) and fluorescent labels (fluorescent lipids or quantum dots), and a targeting ligand. PEGylated lipids typically increase the blood half-life of nanoparticles.

1.4 MOLECULAR MRI

Besides being employed for contrast enhancement of specific tissue characteristics, the abovementioned MR contrast agents can also be used for molecular MRI purposes, in which they enable detection of cellular or molecular entities. A distinction is made between cellular MR imaging, which involves labeling of cells with MR contrast agents to enable tracking of their migration and distribution in tissues, and molecular MR imaging, for which contrast agents are functionalized with ligands (e.g., antibodies) that specifically target molecular markers **(Figure 1.5)**. Both molecular and cellular MRI are limited to targets which are accessable for the contrast agent. Different administration routes can be chosen, but clinically, only minimally invasive administration routes like intravenous or intraarterial

injection are accepted, enabling a good distribution throughout the system, but limiting molecular MRI to vascular targets. Nevertheless, vascular targets are often part of fundamental signaling cascades of various pathology-associated processes, e.g., atherosclerosis, tumor growth and ischemia. This thesis deals with molecular MRI of two types of vascular events that are critically involved in many pathologies; i.e., angiogenesis and neurovascular inflammation.

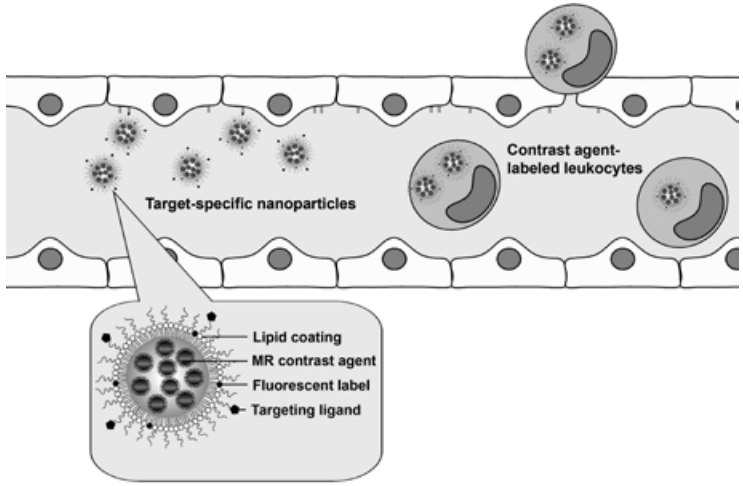

Figure 1.5
Schematic overview of the concept of cellular and molecular MR imaging. Target-specific contrast agents allow detection of e.g., upregulated endothelial markers, such as cell adhesion molecules, while infiltrating cells, e.g., leukocytes, can be detected after specific cell labeling with contrast agents.

1.5 MOLECULAR MRI OF ANGIOGENESIS

Angiogenesis is the formation of new blood vessels from existing vessels, which is a normal and vital process in tissue growth and development that may also occur under pathophysiological conditions, such as after tissue hypoxia (e.g., in tumors) or ischemia (e.g., after stroke) [33]. The stages of onset, formation and maturation of new blood vessels are highly complex, but well-characterized in a couple of stages **(Figure 1.6)**. Angiogenesis is triggered by a lack of oxygen and nutrition in cells. These cells subsequently start transcribing a variety of genes that are involved in the process of angiogenesis, such as vascular endothelial growth factor (VEGF) and proinflammatory cytokines. These factors then activate receptors on endothelial cells, e.g., $\alpha_v\beta_3$ integrin [34] and platelet endothelial cell adhesion molecule (PECAM-1), and thereby create a permissive environment for sprouting of proliferating endothelial cells towards the deprived cells. The activated endothelial cells excrete proteases that degrade the basal membrane, increasing the permittivity of the blood vessel, but also creating room for the proliferating endothelial cells to form vascular buds in the direction of the inclining gradient of angiogenic factors. These vascular buds eventually grow into fully-fledged vessels, connecting with each other and pre-existing vessels, hereby creating a network of vessels supplying the deprived cells of oxygen and nutrition. These newly formed angiogenic microvessels do not always become functional vasculature. This is depended on the pathology that is being investigated [35].

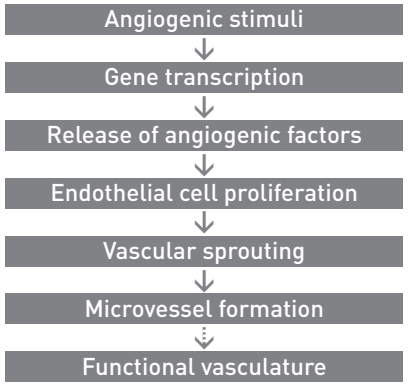

Figure 1.6
Schematic overview of the different stages of angiogenesis.

Molecular MRI of angiogenesis can provide unique information on the process of vascular remodeling after pathophysiological conditions, which may improve disease diagnosis as well as monitoring of anti- or pro-angiogenic therapies. Oncology has been the major focus of angiogenesis-related molecular MRI [36-37]. When malignant tumor growth is detected, it may concern an angiogenic phenotype of the tumor which may respond to anti-angiogenic therapy. MR-based molecular imaging with $\alpha_v\beta_3$ integrin-targeted nanoparticles has demonstrated its potential to monitor tumor angiogenesis [28, 38-39], enabling the differentiation between angiogenic blood vessels from normal blood vessels. In **Chapter 2** of this thesis, we show the application of $\alpha_v\beta_3$ integrin-targeted superparamagnetic nanoemulsions that are able to differentiate between tumors that are low and highly angiogenic [40].

Molecular MRI might also be a promising approach to shed more light on angiogenesis after stroke, which may contribute to elucidation of endogenous repair mechanisms and help to identify specific targets for restorative cell-based and pharmacological therapies, as we report in **Chapter 3**. However, brain vasculature is different from vasculature in other tissues and organs since it contains a blood-brain barrier, which restricts the permeability of vessels to active transport for most molecules. Newly formed cerebral vessels, such as during neuroangiogenesis, lack a blood-brain barrier, which may be identified with vascular permeability imaging. However, blood-brain barrier leakage is also a direct pathological consequence of cerebral ischemia [41]. A clear example of the potential of *in vivo* molecular imaging of angiogenesis after stroke has recently been presented by Cai et al, who used PET to measure upregulation of VEGF receptors with radioactively-labeled VEGF in ischemic rat brain [42]. For non-invasive monitoring of kinetics of expression of molecular markers, nuclear imaging techniques are valuable, however, their relatively low resolution, requirement of a radioactive tracer and lack of anatomical reference, are significant drawbacks that may be overcome by development of MR-based molecular imaging.

1.6 MOLECULAR MRI OF NEUROVASCULAR INFLAMMATION

Inflammation is another major pathology-related event that takes place at the level of the vasculature. Inflammation is part of a complex biological reaction to harmful stimuli **(Figure 1.7)**, which may be seen as a protective attempt to prevent further injury and to initiate recovery, but which may also be detrimental under certain conditions. Inflammation starts with the release of pro-inflammatory cytokines by resident immune cells. These cytokines trigger endothelial cells to release proteases to increase vascular permeability and to express cell adhesion molecules that facilitate the transmigration of blood-born leukocytes towards the injured site [43].

Inflammation plays a significant role – which can be beneficial as well as detrimental – in a wide variety of pathologies, and is therefore of interest to assess with molecular MRI. Atherosclerosis-induced inflammation has been the target for molecular MRI in a variety of studies, exploiting different molecular MRI strategies with gadolinium and iron oxide-based contrast agents targeted to a myriad of vascular targets [44-46].

Also inflammation after myocardial infarction has been the topic of interest in many reports [47-48]. Recently, also neurovascular inflammation has been focus of molecular MRI studies. MR imaging of molecular neurovascular inflammatory markers in rat and mouse brain has been successfully demonstrated in experimental neuroinflammation models, where cytokines were injected intracerebrally [49-51]. These models guarantee a high expression of cell adhesion molecules, and may therefore serve in proof-of-principle studies for *in vivo* detection of target-specific MR contrast agents.

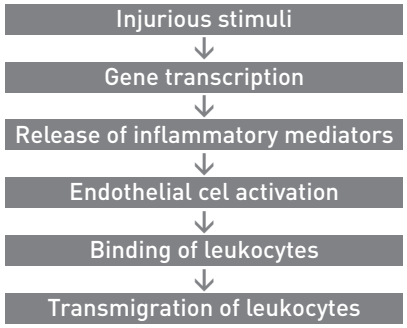

Figure 1.7
Schematic overview of the inflammatory cascade upon an injurious stimuli.

The first studies that reported on *in vivo* molecular MR imaging of pathology-induced neuroinflammation aimed to visualize the upregulation of the endothelial leukocyte adhesion molecules P- and E-selectin in a stroke model [52]. For this purpose, the paramagnetic contrast agent Gd-DTPA was functionalized with a mimetic of sialyl Lewis^{X} (sLe^{X}), a glycan that binds to cell adhesion molecule P- or E-selectin. Even though changes in longitudinal MR relaxation time T_1 were relatively modest, MR images revealed specific binding of Gd-DTPA-(sLe^{X})A to activated endothelium in the lesion territory at 24 h after transient MCAO in mice. Alternatively, functionalized iron oxide nanoparticles may be applied to enhance contrast effects. This approach has been used in detecting stroke-induced neurovascular inflammation by Van Kasteren et al, who designed sLe^{X}-decorated iron oxide nanoparticles [51], and by Jin et al, who conjugated a P-selectin binding peptide to a magnetic iron oxide nanoparticle [53]. Following injection of these targeted nanoparticles, significant hypointensities on T_2*-weighted MR images were observed at sites of primary and secondary injury, a few hours after endothelin-induced stroke in rats [51], and at 24 h after transient MCAO in mice [53]. Functionalized iron oxide particles have also been used for the detection of other brain pathologies. McAteer et al has shown the effective binding of VCAM-1-targeted MPIO (αVCAM-1-MPIO) in experimental autoimmune

encephalomyelitis (EAE), a mouse model of multiple sclerosis (MS) [54]. This platform was further exploited to detect EAE and brain tumor metastases at early stage when this could not be detected by conventional MRI methods [55-56], and has also been applied in a murine stroke model [19]. Importantly, isotype control immunoglobulin G (IgG)-functionalized MPIO, with similar size, blood half-life and surface properties as the αVCAM-1-MPIO, were administered in a control group in these studies. This allowed assessment of possible non-specific contrast accumulation, for instance as a result of MPIO extravasation through an impaired blood-brain barrier. T_2*-weighted MR brain images of mice injected with αVCAM-1-MPIO revealed significantly more signal voids in affected brain areas as compared to IgG-MPIO injected mice, thereby demonstrating target specificity of the contrast agent. Zhu and co-workers showed a similar set-up to image radiation-induced brain inflammation, however, they chose intercellular adhesion molecule-1 (ICAM-1) as a target [57], which was already shown to be a suitable target for *post mortem* MRI analysis after *in vivo* injection of ICAM-1-targeted Gd-liposomes [58]. **Chapters 4, 5 and 6** of this thesis also report on the use of ICAM-1-targeted MR contrast agent to target neurovascular inflammation.

1.7 OUTLINE OF THIS THESIS

This thesis describes the use of different MR contrast agent platforms for the direct detection of pathology-induced upregulation of intraluminally-expressed vascular entities by molecular MRI. We particularly focused on the *in vivo* target specificity and MR sensitivity of the agents. The biological targets of our molecular MRI approaches were associated with two types of vascular events that are critically involved in many pathologies; i.e., angiogenesis and neurovascular inflammation. **Chapters 2 and 3** touch upon the topic of molecular MRI of angiogenesis, whereas **Chapters 4, 5 and 6** explore the applicability of molecular MRI of neurovascular inflammation.

In **Chapter 2**, iron oxide-containing nanoemulsions targeted to angiogenesis-upregulated $\alpha_v\beta_3$ integrin were tested on their ability to adequately monitor the angiogenic activity of a tumor malignancy to serve as an *in vivo* biomarker for anti-angiogenesis treatment and angiogenesis phenotyping. **Chapter 3** reports on the efficacy of PECAM-1-targeted MPIO for MRI of vascular remodeling after experimental stroke.

Assessment of the suitability of two ICAM-1-targeted MR contrast agents, i.e., based on Gd-liposomes or MPIO, for molecular MRI of upregulation of the neuroinflammatory biomarker ICAM-1 after stroke, is described in **Chapter 4**. In **Chapter 5**, ICAM-1-targeted MPIO were administrated at different time points post-stroke in mice to determine to what extent different stages of endothelial activation and leukocyte infiltration can be visualized with this agent. **Chapter 6** explores if ICAM-1-targeted MPIO are able to detect EAE-induced ICAM-1 upregulation at a stage when conventional MRI does not reveal any lesions. **Chapter 7** concludes this thesis with a general discussion.

1.8 REFERENCES

1. Thakur M, Lentle BC (2005) Report of a summion molecular imaging. Radiology 236:753-755.
2. Weissleder R, Mahmood U (2001) Molecular imaging. Radiology 219:316-333.
3. Shilo M, Reuveni T, Motiei M, Popovtzer R (2012) Nanoparticles as computed tomography contrast agents: current status and future perspectives. Nanomedicine (Lond) 7:257-269.
4. Kiessling F, Fokong S, Koczera P, Lederle W, Lammers T (2012) Ultrasound microbubbles for molecular diagnosis, therapy, and theranostics. J Nucl Med 53:345-348.
5. Pimlott SL, Sutherland A (2011) Molecular tracers for the PET and SPECT imaging of disease. Chem Soc Rev 40:149-162.
6. Hilderbrand SA, Weissleder R (2010) Near-infrared fluorescence: application to *in vivo* molecular imaging. Curr Opin Chem Biol 14:71-79.
7. Brogan J, Li F, Li W, He Z, Huang Q, Li CY (2012) Imaging molecular pathways: reporter genes. Radiat Res 177:508-513.
8. Dijkhuizen RM, Nicolay K (2003) Magnetic resonance imaging in experimental models of brain disorders. J Cereb Blood Flow Metab 23:1383-1402.
9. Carrington A, McLachlan AD (1967) Introduction to magnetic resonance. Chapman and Hall, London.
10. Haacke EM, Brown RW, Thompson MR, Venkatesan R (1999) Magnetic resonance imaging: physical principles and sequence design. Wiley, New York.
11. Weast RC (1972) Handbook of chemistry and physics. Chemical Rubber Company, Cleveland, Ohio.
12. Foster MA (1984) Magnetic resonance in medicine and biology Pergamon Press, New York.

13. Muller RN, Roch A, Colet J-M, Ouakssim A, Gillis P (2001) Particulate magnetic contrast agents. In The chemistry of contrast agents in medical magnetic resonance imaging, Eds. Merbach AE, Tóth E. John Wiley & Sons, Ltd, pp 417-435.

14. Aime S, Fasano M, Terreno E (1998) Lanthanide(III) chelates for NMR biomedical applications. Chem Soc Rev 27:19-29.

15. Laurent S, Elst LV, Muller RN (2006) Comparative study of the physico chemical properties of six clinical low molecular weight gadolinium contrast agents. Contrast Media Mol Imaging 1:128-137.

16. Gossuin Y, Gillis P, Hocq A, Vuong QL, Roch A (2009) Magnetic resonance relaxation properties of superparamagnetic particles. Wiley Interdiscip Rev Nanomed Nanobiotechnol 1:299-310.

17. Weissleder R, Stark DD, Engelstad BL, Bacon BR, Compton CC, White DL, Jacobs P, Lewis J (1989) Super paramagnetic iron oxide: pharmacokinetics and toxicity. AJR Am J Roentgenol 152:167-173.

18. Bulte JW, Vymazal J, Brooks RA, Pierpaoli C, Frank JA (1993) Frequency dependence of MR relaxation times. II. Iron oxides. J Magn Reson Imaging 3:641-648.

19. Hoyte LC, Brooks KJ, Nagel S, Akhtar A, Chen R, Mardiguian S, McAteer MA, Anthony DC, Choudhury RP, Buchan AM, Sibson NR (2010) Molecular magnetic resonance imaging of acute vascular cell adhesion molecule-1 expression in a mouse model of cerebral ischemia. J Cereb Blood Flow Metab 30:1178-1187.

20. Nkansah MK, Thakral D, Shapiro EM (2011) Magnetic poly(lactide-co-glycolide) and cellulose particles for MRI-based cell tracking. Magn Reson Med 65:1776-1785.

21. Mulder WJ, Strijkers GJ, Van Tilborg GA, Cormode DP, Fayad ZA, Nicolay K (2009) Nanoparticulate assemblies of amphiphiles and diagnostically active materials for multimodality imaging. Acc Chem Res 42:904-914.

22. Klibanov AL, Maruyama K, Torchilin VP, Huang L (1990) Amphipathic polyethyleneglycols effectively prolong the circulation time of liposomes. FEBS Lett 268:235-237.

23. Van Tilborg GA, Strijkers GJ, Pouget EM, Reutelingsperger CP, Sommerdijk NA, Nicolay K, Mulder WJ (2008) Kinetics of avidin-induced clearance of biotinylated bimodal liposomes for improved MR molecular imaging. Magn Reson Med 60:1444-1456.

24. Torchilin VP (2005) Recent advances with liposomes as pharmaceutical carriers. Nat Rev Drug Discov 4:145-160.

25. Mulder WJ, Strijkers GJ, Griffioen AW, Van Bloois L, Molema G, Storm G, Koning GA, Nicolay K (2004) A liposomal system for contrast-enhanced magnetic resonance imaging of molecular targets. Bioconjug Chem 15:799-806.

26. Jarzyna PA, Skajaa T, Gianella A, Cormode DP, Samber DD, Dickson SD, Chen W, Griffioen AW, Fayad ZA, Mulder WJ (2009) Iron oxide core oil-in-water emulsions as a multifunctional nanoparticle platform for tumor targeting and imaging. Biomaterials 30:6947-6954.

27. Van Tilborg GA, Mulder WJ, Deckers N, Storm G, Reutelingsperger CP, Strijkers GJ, Nicolay K (2006) Annexin A5-functionalized bimodal lipid-based contrast agents for the detection of apoptosis. Bioconjug Chem 17:741-749.

28. Mulder WJ, Strijkers GJ, Habets JW, Bleeker EJ, Van der Schaft DW, Storm G, Koning GA, Griffioen AW, Nicolay K (2005) MR molecular imaging and fluorescence microscopy for identification of activated tumor endothelium using a bimodal lipidic nanoparticle. FASEB J 19:2008-2010.

29. Phillips WT, Goins BA, Bao A (2009) Radioactive liposomes. Wiley Interdiscip Rev Nanomed Nanobiotechnol 1:69-83.

30. Van Schooneveld MM, Cormode DP, Koole R, Van Wijngaarden JT, Calcagno C, Skajaa T, Hilhorst J, t Hart DC, Fayad ZA, Mulder WJ, Meijerink A (2010) A fluorescent, paramagnetic and PEGylated gold/silica nanoparticle for MRI, CT and fluorescence imaging. Contrast Media Mol Imaging 5:231-236.

31. Mulder WJ, Koole R, Brandwijk RJ, Storm G, Chin PT, Strijkers GJ, De Mello Donega C, Nicolay K, Griffioen AW (2006) Quantum dots with a paramagnetic coating as a bimodal molecular imaging probe. Nano Lett 6:1-6.

32. Jarzyna PA, Gianella A, Skajaa T, Knudsen G, Deddens LH, Cormode DP, Fayad ZA, Mulder WJ (2010) Multifunctional imaging nanoprobes. Wiley Interdiscip Rev Nanomed Nanobiotechnol 2:138-150.

33. Folkman J (1971) Tumor angiogenesis: therapeutic implications. N Engl J Med 285:1182-1186.

34. Robinson SD, Hodivala-Dilke KM (2011) The role of beta3-integrins in tumor angiogenesis: context is everything. Curr Opin Cell Biol 23:630-637.

35. Rubanyi GM (2000) Angiogenesis in health and disease. M. Dekker, Inc., New York - Basel.

36. Pathak AP, Penet MF, Bhujwalla ZM (2010) MR molecular imaging of tumor vasculature and vascular targets. Adv Genet 69:1-30.

37. Strijkers GJ, Kluza E, Van Tilborg GA, van der Schaft DW, Griffioen AW, Mulder WJ, Nicolay K (2010) Paramagnetic and fluorescent liposomes for target-specific imaging and therapy of tumor angiogenesis. Angiogenesis 13:161-173.

38. Sipkins DA, Cheresh DA, Kazemi MR, Nevin LM, Bednarski MD, Li KC (1998) Detection of tumor angiogenesis *in vivo* by alphaVbeta3-targeted magnetic resonance imaging. Nat Med 4:623-626.

39. Winter PM, Schmieder AH, Caruthers SD, Keene JL, Zhang H, Wickline SA, Lanza GM (2008) Minute dosages of alpha(nu)beta3-targeted fumagillin nanoparticles impair Vx-2 tumor angiogenesis and development in rabbits. FASEB J 22:2758-2767.

40. Jarzyna PA, Deddens LH, Kann BH, Ramachandran S, Calcagno C, Chen W, Gianella A, Dijkhuizen RM, Griffioen AW, Fayad ZA, Mulder WJ (2012) Tumor angiogenesis phenotyping by nanoparticle-facilitated magnetic resonance and near-infrared fluorescence molecular imaging Neoplasia 14:964-973.

41. Yanev P, Dijkhuizen RM (2012) *In vivo* imaging of neurovascular remodeling after stroke. Stroke 43:3436-3441.

42. Cai W, Guzman R, Hsu AR, Wang H, Chen K, Sun G, Gera A, Choi R, Bliss T, He L, Li ZB, Maag AL, Hori N, Zhao H, Moseley M, Steinberg GK, Chen X (2009) Positron emission tomography imaging of poststroke angiogenesis. Stroke 40:270-277.

43. Iadecola C, Anrather J (2011) The immunology of stroke: from mechanisms to translation. Nat Med 17:796-808.

44. Kanwar RK, Chaudhary R, Tsuzuki T, Kanwar JR (2012) Emerging engineered magnetic nanoparticulate probes for molecular MRI of atherosclerosis: how far have we come? Nanomedicine (Lond) 7:899-916.

45. Kanwar RK, Chaudhary R, Tsuzuki T, Kanwar JR (2012) Emerging engineered magnetic nanoparticulate probes for targeted MRI of atherosclerotic plaque macrophages. Nanomedicine (Lond) 7:735-749.

46. Te Boekhorst BC, van Tilborg GA, Strijkers GJ, Nicolay K (2012) Molecular MRI of inflammation in atherosclerosis. Curr Cardiovasc Imaging Rep 5:60-68.

47. Geelen T, Paulis LE, Coolen BF, Nicolay K, Strijkers GJ (2012) Contrast-enhanced MRI of murine myocardial infarction - part I. NMR Biomed 25:953-968.

48. Sosnovik DE, Nahrendorf M, Caravan P (2012) Science to practice: how will myocardial inflammation be imaged with MR imaging? Radiology 264:309-311.

49. McAteer MA, Choudhury RP (2009) Chapter 4 - Applications of nanotechnology in molecular imaging of the brain. Prog Brain Res 180:72-96.

50. Sibson NR, Anthony DC, Van Kasteren S, Dickens A, Perez-Balderas F, McAteer MA, Choudhury RP, Davis BG (2011) Molecular MRI approaches to the detection of CNS inflammation. Methods Mol Biol 711:379-396.

51. Van Kasteren SI, Campbell SJ, Serres S, Anthony DC, Sibson NR, Davis BG (2009) Glyconanoparticles allow pre-symptomatic *in vivo* imaging of brain disease. Proc Natl Acad Sci U S A 106:18-23.

52. Barber PA, Foniok T, Kirk D, Buchan AM, Laurent S, Boutry S, Muller RN, Hoyte L, Tomanek B, Tuor UI (2004) MR molecular imaging of early endothelial activation in focal ischemia. Ann Neurol 56:116-120.

53. Jin AY, Tuor UI, Rushforth D, Filfil R, Kaur J, Ni F, Tomanek B, Barber PA (2009) Magnetic resonance molecular imaging of post-stroke neuroinflammation with a P-selectin targeted iron oxide nanoparticle. Contrast Media Mol Imaging 4:305-311.

54. McAteer MA, Sibson NR, von Zur Muhlen C, Schneider JE, Lowe AS, Warrick N, Channon KM, Anthony DC, Choudhury RP (2007) *In vivo* magnetic resonance imaging of acu te brain inflammation using microparticles of iron oxide. Nat Med 13:1253-1258.

55. Serres S, Mardiguian S, Campbell SJ, McAteer MA, Akhtar A, Krapitchev A, Choudhury RP, Anthony DC, Sibson NR (2011) VCAM-1-targeted magnetic resonance imaging reveals subclinical disease in a mouse model of multiple sclerosis. FASEB J 25:4415-4422.

56. Serres S, Soto MS, Hamilton A, McAteer MA, Carbonell WS, Robson MD, Ansorge O, Khrapitchev A, Bristow C, Balathasan L, Weissensteiner T, Anthony DC, Choudhury RP, Muschel RJ, Sibson NR (2012) Molecular MRI enables early and sensitive detection of brain metastases. Proc Natl Acad Sci U S A 109:6674-6679.

57. Zhu Y, Ling Y, Zhong J, Liu X, Wei K, Huang S (2012) Magnetic resonance imaging of radiation-induced brain injury using targeted microparticles of iron oxide. Acta Radiol 53:812-819.

58. Sipkins DA, Gijbels K, Tropper FD, Bednarski M, Li KC, Steinman L (2000) ICAM-1 expression in autoimmune encephalitis visualized using magnetic resonance imaging. J Neuroimmunol 104:1-9.

TUMOR ANGIOGENESIS PHENOTYPING BY NANOPARTICLE-FACILITATED MR AND NIRF MOLECULAR IMAGING

Based on:
Peter A. Jarzyna, Lisette H. Deddens, Benjamin H. Kann, Sarayu Ramachandran, Claudia Calcagno, Wei Chen, Anita Gianella, Rick M. Dijkhuizen, Arjan W. Griffioen, Zahi A. Fayad and Willem J. M. Mulder.
Tumor angiogenesis phenotyping by nanoparticle-facilitated magnetic resonance and near-infrared fluorescence molecular imaging.
Neoplasia **2012** 14: 964-973

02

2.1 ABSTRACT

One of the challenges of tailored anti-angiogenic therapy is the ability to adequately monitor the angiogenic activity of a malignancy in response to treatment. The $\alpha_v\beta_3$ integrin, highly overexpressed on newly formed tumor vessels, has been successfully used as a target for Arg-Gly-Asp (RGD)-functionalized nanoparticle contrast agents. In the present study, an RGD-functionalized nanocarrier was used to image ongoing angiogenesis in two different xenograft tumor models with varying intensities of angiogenesis (LS174T > EW7). To that end, iron oxide nanocrystals were included in the core of the nanoparticles to provide contrast for T_2*-weighted magnetic resonance imaging (MRI), while the fluorophore Cy7 was attached to the surface to enable near-infrared fluorescence (NIRF) imaging. The mouse tumor models were used to test the potential of the nanoparticle probe in combination with dual modality imaging for *in vivo* detection of tumor angiogenesis. Pre- and post-contrast images (4 h) were acquired at a 9.4 T MRI system, and revealed significant differences in the nanoparticle accumulation patterns between the two tumor models. In the case of the highly vascularized LS174T tumors, the accumulation was more confined to the periphery of the tumors, where angiogenesis is predominantly occurring. NIRF imaging revealed significant differences in accumulation kinetics between the models. In conclusion, this technology can serve as an *in vivo* biomarker for anti-angiogenesis treatment and angiogenesis phenotyping.

2.2 INTRODUCTION

Angiogenesis is one of the crucial processes in tumor growth and development, and is considered to predict short term survival. Compared to the highly organized morphology of blood vessels in healthy tissues, the tumor vasculature is characterized by a chaotic architecture, tortuous vessel structure and a leaky endothelium [1]. While many angiogenesis inhibitors are already known for decades [2], it wasn't until 2004 that the Food and Drug Administration (FDA) approved the first anti-angiogenic drug (bevacizumab) for clinical use [3-4]. Agents targeting different angiogenic pathways were subsequently approved [5] or are currently in different stages of clinical trails [6-8]. The major drawbacks associated with angiostatic drugs are inherent or acquired tumor resistance, increased tumor invasiveness, limited effects on overall survival and, notably, a lack of reliable and thoroughly validated predictive biomarkers to monitor response to treatment [6-7]. For the latter imaging is being considered as an approach to non-invasively track response to anti-angiogenic therapy [9]. The most common standardized *post mortem* measure of angiogenesis of tissue specimens is the determination of the microvessel density (MVD). Quantification of the MVD is performed by counting the (maximal) number of stained blood vessels per defined area on a histological section [10]. *In vivo* imaging read-outs of MVD include dynamic contrast-enhanced magnetic resonance imaging (DCE-MRI) [11], dynamic contrast-enhanced computed tomography (DCE-CT) [12], ultrasound [13], positron emission tomography (PET) [14] and optical methods [15-16]. Among those, DCE-MRI is the most widely explored method for monitoring response to anti-angiogenic tumor therapy in both animal models [17] and clinical studies [18-19]. It relies on the fast acquisition of T_1-weighted MR images after rapid intravenous injection of gadolinium based contrast agents [20]. DCE-MRI was used in a recent study to investigate its potential as a biomarker for the treatment of metastatic renal cancer with the receptor tyrosine kinase inhibitor sorafenib, which blocks the vascular endothelial growth factor (VEGF) receptor [21]. While DCE-MRI-derived parameters could be shown as pharmacodynamic biomarkers for this agent, variability was high, and therefore further refinements of the data acquisition and analysis are needed.

Within the field of molecular imaging, nanotechnology and in particular the development of nanoparticle contrast agents, has seen unprecedented growth in the last years [22]. Because of their ability to incorporate high payloads of contrast agents/drugs as well as the possibility to covalently attach targeting molecules to the surface [23], their use to also investigate angiogenic processes has emerged as a very promising tool in cancer research [24-25]. The $\alpha_v\beta_3$ integrin is known to be significantly upregulated on activated endothelial cells during neoangiogenesis. By binding to the sequence arginine-glycine-aspartate (RGD), it mediates its biological activity and therefore this peptide sequence has been used to functionalize contrast agents/nanoparticles for targeting the tumor neovasculature [26-28].

In the current study the RGD-peptide was attached to the surface of a nanoparticle platform that we described previously [29]. It is based on oil-in-water nanoemulsions with a tunable particle size in a range of 30-100 nm, and the possibility to include lipophilic contrast agents/drugs in the core as well as amphiphilic ones in the corona.

Here, we focused on iron oxide-enhanced T_2*-weighted MRI and near-infrared fluorescence (NIRF) imaging (Cy7 fluorophore), two very complementary imaging modalities of RGD-functionalized nanoparticles. The first modality was used to acquire spatial distribution of angiogenic activity at a given time point, while NIRF imaging provided time resolved information about the nanoparticle binding kinetics in the tumors over a period of 24 h. Two xenograft tumor models - the highly angiogenic

human colorectal LS174T [30] model and the slow growing and low vascular density human EW7 Ewing sarcoma model [31] - were chosen to evaluate our approach with regard to its capability to adequately distinguish different intensity levels of angiogenesis. Moreover, the latter model is known to show abundant vascular mimicry in the outer rim of the tumors, a phenomenon in which tumor cells form tubular structures that contribute to circulation [32], explaining the lower MVD. These fundamental differences between the EW7 and LS174T tumors made us decide that the EW7 group injected with targeted contrast agent served as a control for the LS174T groups examined in this study. Confocal laser scanning microscopy (CLSM) and histological staining for iron oxide were used to examine the location of the nanoparticles in the tumor tissues and corroborate the *in vivo* findings.

2.3 MATERIALS AND METHODS

2.3.1 Materials Distearoyl-sn-glycero-3-phosphocholine (DSPC), distearoyl-phosphoethanolamine-N-[methoxy (polyethylene glycol)-2000] ammonium salt (DSPE-PEG), 1,2-distearoyl-sn-glycero-3-phosphoethanolamine-N-[maleimide(polyethylene glycol)-2000] ammonium salt (DSPE-PEG (maleimide)), 1,2-dimyristoyl-sn-glycero-3-phospho-ethanolamine-N-(lissamine rhodamine B sulfonyl) and distearoyl-phosphoethanolamine-N-[amino(polyethylene glycol)-2000] (DSPE-PEG (amino)) were all purchased from Avanti Polar Lipids. Oleic acid coated magnetite (Fe_3O_4) particles with an average diameter of 10 nm were obtained as a powder from NN labs (Fayetteville, AR, USA). The cyclic 5-mer RGD (c(RGDf(S-acetylthioacetyl)K)) was obtained from Peptides International (Louisville, KY, USA). The Cy7 NHS ester was purchased from Amersham Biosciences (Piscataway, NJ, USA). Cell culture supplies were purchased from Invitrogen (Carlsbad, CA, USA).

2.3.2 Synthesis of the nanoemulsions For the synthesis of the nanoemulsions, separate stock solutions of all the lipophilic components were prepared in chloroform. The Cy7-DSPE-PEG lipid was synthesized using the DSPE-PEG (amino) lipid and Cy7-NHS ester as described earlier [29]. The composition of the formulation was: 2.7 mg of DSPC, 9.1 mg of DSPE-PEG, 38 mg of soybean oil, 19.8 mg of iron oxide particles, 1.06 mg of DSPE-PEG (maleimide), 746 µg of Cy7-DSPE-PEG lipids (= 0.22 µmol Cy7) and 40 µg 1,2-dimyristoyl-sn-glycero-3-phospho-ethanolamine-N-(lissamine rhodamine B sulfonyl). The components were mixed together and the solvent evaporated in a rotary evaporator under maximum vacuum in a 70 °C water bath. The formed lipid layer was hydrated with 10 ml of HEPES-buffered saline (HBS; 2.38 g/l HEPES, 8 g/l NaCl, pH 6.7) and the crude emulsion homogenized by sonication using a sonicator tip (3.9 mm). The formulation was sonicated for 20 min (level 20 %, pulse 70 %, device: BioLogics, Inc. (Manassas, VA, USA) ultrasonic homogenizer model 150 V/T) while being cooled with room temperature water. Finally, the nanoparticle suspension was concentrated to a final volume of 2 ml by using a Vivaspin 6 centrifugal filter device (membrane cut off: 100 kD; Sartorius Corporation, Edgewood, NY, USA) and divided into two batches of 1 ml each. Cyclic RGD was activated by adding 5 µl of deacetylation solution (348 mg Hydroxylamine*HCl, 1.19 g Hepes, 98 mg EDTA in 10 ml Millipore water; pH 7.0) to 50 µl RGD stock solution (2.5 mg/ml), and placed on a shaker at RT for 45 min. 20 µl of activated cyclic RGD solution was added to one of the two batches of nanoemulsions for the coupling reaction to take place overnight at 4 °C, while the other served as a control. Both formulations were washed the next day by using Vivaspin 6 columns. To ensure that the formulations of different batches had the same iron oxide content, T_1 values of every batch of nanoemulsion were measured (diluted 1:10 with water, 60 MHz Bruker Minispec device operating at 40 °C, Bruker Medical GmbH, Ettlingen, Germany).

2.3.3 Dynamic light scattering Hydrodynamic sizes of the nanoparticles were measured by using dynamic light scattering (Brookhaven Instruments, Holtsville, NY, USA) after washing of the particles. 10 µl of the nanoemulsion formulation was diluted in 1 ml Millipore water for the measurement.

2.3.4 Cell culture and tumor model Human EW7 (Ewing's sarcoma, a kind gift of dr. O. Delattre, Paris, France) cancer cells were cultured in RPMI 1640 medium, human LS174T (colon carcinoma) in DMEM medium, both supplemented with 10 % FCS. The cells were grown in a 5 % CO^2, water saturated atmosphere at 37 °C and subculturing was performed once a week by 1:10 dilution after trypsinization. All animal handling protocols and procedures were approved by the Mount Sinai School of Medicine Institutional Animal Care and Use Committee. Six-week-old male Swiss nude mice were purchased from Taconic (Albany, NY, USA). Subcutaneous tumors were established by injecting 2 million cells of the same cancer type in the lower left and right flank of the mouse, respectively.

2.3.5 Study outline Two complementary imaging methods [22], NIRF imaging and MRI, were used to examine the potential of the targeted nanoparticles to serve as a contrast agent for the phenotyping of tumors with different levels of angiogenesis **(Figure 2.1)**. To that end, three different mice groups (6 mice per group) were established

to determine the time resolved accumulation by NIRF imaging: (1) LS174T mice injected with RGD-conjugated nanoparticles: LS174T RGD; (2) mice with LS174T tumors injected with unconjugated nanoparticles: LS174T control and (3) EW7 bearing mice injected with RGD nanoparticles: EW7 RGD. All the groups used for the NIRF imaging experiments were injected with nanoparticles lacking iron oxide nanocrystals. MRI was used to investigate the spatial distribution of the contrast agent within the tumors in dependence of the presence or absence of the targeting molecule RGD on the surface of the particles. The following five groups were used to acquire the MRI data: (4) LS174T RGD, (5) LS174T control, (6) EW7 RGD, (7) LS174T(C) RGD and (8) LS174T comp. Groups (7) and (8) were chosen for the competition experiment. Group (7) was similar to group (4), but injected with a different batch of RGD-conjugated (iron oxide) nanoparticles, and used as control for group (8). In the latter group, mice received two injections: The first injection consisted of RGD nanoparticles lacking iron iron oxide, the second one was given 1.5 h afterwards and contained RGD nanoparticles carrying iron oxide (same batch as used in group (7)). For the first injection twice as many particles were administered than for the second.

The purpose of the MRI competition experiment was to demonstrate that the previously acquired specific accumulation (signal loss) pattern of the RGD-targeted particles in LS174T tumors (group 4) was caused by binding to the $\alpha_v\beta_3$ integrins rather than non-specific accumulation. This was performed by monitoring changes in the signal attenuation pattern after saturating $\alpha_v\beta_3$ integrins by non-labeled nanoparticles in the tumors prior to injection of the targeted nanoparticles carrying the iron oxide label. To achieve saturation, we chose the injection of the first dose of unlabeled nanoparticles to be twice that of the labeled nanoparticles.

Two different tumor models with distinct microvessel density (MVD):

EW7 → MVD → LS174T

Group	Purpose	Designation	Tumor type	Targeting	Mouse count	Imaging modality	Contrast agents	Injection (i.v.)	Scan range
1	Time-resolved accumulation	LS174T RGD	LS174T	RGD	6	NIRF	Cy7/Rhodamine	1	0-24 h
2		LS174T control	LS174T	-	6	NIRF	Cy7/Rhodamine	1	0-24 h
3		EW7 RGD	EW7	RGD	5	NIRF	Cy7/Rhodamine	1	0-24 h
4	Anatomical detail	LS174T RGD	LS174T	RGD	6	MRI	Fe_3O_4/Cy7/Rhodamine	1	0-4 h
5		LS174T control	LS174T	-	6	MRI	Fe_3O_4/Cy7/Rhodamine	1	0-4 h
6		EW7 RGD	EW7	RGD	6	MRI	Fe_3O_4/Cy7/Rhodamine	1	0-4 h
7	Competition experiment	LS174T (C) RGD	LS174T	RGD	6	MRI	Fe_3O_4/Cy7/Rhodamine	1	0-4 h
8		LS174T comp	LS174T	RGD	6	MRI	(1) Cy7/Rhodamine (2) Fe_3O_4/Cy7/Rhodamine	2	0-4 h

Figure 2.1 *

*** Figure 2.1**

Conceptual scheme of the study characterizing the different mice groups selected for the *in vivo* NIRF imaging and the MRI experiments (6 mice per group, 2 tumors per mouse). Nanoparticles used for the MRI imaging contained iron oxide, while those for the NIRF imaging were lacking it. LS174T RGD: Mice bearing LS174T tumors injected i.v. with RGD nanoparticles; LS174T control: Mice with LS174T tumors injected with unconjugated nanoparticles; EW7 RGD: Mice bearing EW7 tumors injected with RGD nanoparticles; LS174T comp: Mice with LS174T tumors that were injected twice for the competition experiment. The first injection was performed with RGD nanoparticles lacking iron oxide, the second with RGD nanoparticles carrying iron oxide 1.5 h afterwards; LS174T (C) RGD: Mice bearing LS174T tumors injected with RGD nanoparticles (iron oxide, same batch as used for LS174T comp) to serve as a control for the competition experiment.

2.3.6 Near-infrared fluorescence imaging and data analysis NIRF imaging was performed with a custom-made imaging system [33-34] using a 760 nm excitation filter, an 800 nm emission filter, and an exposure time of 700 ms. The camera of the device was operated with the LabView software (National Instruments, Austin, TX, USA, [35]). Swiss nude mice were anesthetized with a 4 % isoflurane/oxygen gas mixture (400 ml/min initial dose) and maintained by using 1.5 % isoflurane/oxygen gas (100 ml/min) delivered through a nose cone. The mice were injected intravenously (i.v.) with the nanoparticles through the tail vein. For the time resolved accumulation, images were acquired 5 min, 15 min, 30 min, 1 h, 2 h, 4 h, 6 h, and 24 h after i.v. injection. The mice were perfused with PBS containing 20 U Heparin/ml directly afterwards, while being under isoflurane anesthesia. In three mice of each group, Alexa Fluor 488-labeled isolectin GS-IB4 (a general stain for vascular endothelium; Invitrogen) was administered i.v. 15 min before perfusion. Tumors as well as organs were excised and imaged simultaneously with an exposure time of 500 ms. Subsequently, the tumors were embedded in TissueTek (Sakura, Torrance, CA, USA) and stored at -80 ˚C.

For the data analysis of the fluorescence images (24 h kinetic), ROIs outlining the tumors as well as parts of the skin, respectively, were drawn using ImageJ software. By using the following equation, the signal intensity of the tumor was normalized to the signal intensity of the skin: NER = (Itumor - Iskin)/Iskin x 100 % (NER: Normalized enhancement ratio; Itumor: Signal intensity of tumor ROI at certain time point; Iskin: Signal intensity of skin ROI at equal time point). All calculated values were subtracted by the value determined at the 5 min time point to correct for the blood pool signal. To evaluate statistical significance, a two-way ANOVA analysis was used and $P < 0.05$ was considered as significant.

The biodistribution of the nanoparticles was evaluated by drawing ROIs along the outlines of the excised tumors and organs. Subsequently, all relative fluorescence intensities I (I = (ROI area) x (mean signal intensity of ROI)) corresponding to the different ROIs per mouse were added up to create a 100 % value (Io) to which all the individuals values (I) of the organs or tumors were normalized. The determined values (I/Io) were averaged within the mouse groups **(Figure 2.4D)**. To assess the accumulation of the nanoparticles in the tumors compared to the liver, the averaged tumor-fluorescence intensities were normalized to the liver intensity per mouse (Itumor/Iliver x 100 %) and averaged again within the three different mouse groups.

2.3.7 Immunohistochemistry, confocal and Perls' staining To determine the MVD of the tumors, 5 µm cryosections were cut, followed by fixation in acetone for 5 minutes at -20 °C. After blocking unspecific sites by using 4 % rabbit serum in PBS for 10 minutes, sections were incubated with rat anti-mouse CD31 primary antibody (BD Pharmingen) in a dilution of 1:100 with 4 % rabbit serum. A rabbit anti-rat secondary antibody and the alkaline phosphatase method served for the staining (Vector ABC kit, Vector Laboratories, Burlingame CA, USA). Four tumors of the EW7 RGD group and five tumors of the LS174T RGD group were analyzed with 1-2 sections per tumor. Several digital images of the tumor sections were photographed in bright field by using the Axioplan 2IE microscope with a 20x objective and stitched together by using the Axiovision 4.6.3 SP1 software to one image displaying the entire tumor section. The CD31+ color (red) selection was performed by using the gimp 2 software and converted to greyscale images. These images showing only positive CD31 areas were inverted to white (signal) on black (background) images. ROIs were drawn along the outlines of the tumors and the area fraction in percent was determined by using ImageJ software **(Figure 2.8)**.

2.3.8 MR imaging and data analysis Nude mice bearing EW7 or LS174T subcutaneous tumors were scanned under isoflurane anesthesia using a 9.4 T MRI system (400.106 MHz; Bruker Instruments), operated by the ParaVision software 4.0. MR imaging was performed by using a gradient echo sequence (T_2*) with a repetition time (TR) of 120 ms, echo time (TE) of 3 ms, flip angle of 30°, field of view of 2.6 x 2.6 cm^2, matrix size of 128 x 128, 10 slices with a slice thickness of 1 mm, and 16 averages, which amounted to a total scan time of 2.5 min. After the pre-scans, mice were injected i.v. with the nanoemulsion (equivalent of 36.7 mg/kg iron oxide), and scanned up to 4 h post injection in 30 min steps while the position of the mouse remained unchanged.

The data analysis of the T_2* images was performed by using a custom-made program written in MATLAB (MathWorks, Natick MA, USA). An ROI was manually drawn along the outline of the selected tumor slice. The program used this outer outline to automatically subdivide the tumor section into five concentric sub-ROIs of equal area from the periphery to the core (ROIs 1-5; **Figure 2.3C**). For the pixel-by-pixel analysis per ROI, a threshold of 4x the standard deviation of the noise was set to define a pixel of the 4 h post image to be "reduced" (hypointense due to contrast agent accumulation) compared to the one of the pre-scanned image. Two slices were analyzed per tumor and the percentage of reduced pixels per total number of pixels in the equal area ROI of two slices was averaged in each mouse group and plotted against the corresponding ROI. For the statistical analysis, a paired t-test of the values for the reduced pixels (%) of ROI 1 (periphery) versus ROI 5 (core) was performed for each mouse group. P values < 0.05 were considered as statistically significant.

2.4 RESULTS

2.4.1 *In vivo* MRI The distribution pattern of iron oxide nanoemulsions (mean particle size range: 75-85 nm) with and without the conjugation of RGD in tumors was investigated by T_2*-weighted MRI, which is sensitive to the presence of iron. Five groups of mice were chosen to compare the two different tumor models (LS174T vs EW7) with distinct MVD and to perform a competition experiment (**Figure 2.1**, details see Methods section). To minimize the error for the pre-post quantification due to movement or reposition of the mouse after application of the contrast agent, the mice were fixed and kept in the same position in the coil during the entire scan series. In the pre-contrast images, the tumors appear isointense with their surrounding muscle tissue **(Figure 2.2 A-D)**. The mice were scanned immediately after the administration of the nanoemulsion (equivalent of 36.7 mg/kg iron oxide) and an intense homogeneous darkening of the tumor area served as proof for a proper i.v. injection. Based on the half-lives previously determined for the untargeted version of the nanoemulsions [29], four hours post administration was considered to be sufficient for the necessary clearance of the particles from the blood pool. Hypointense (dark) regions could be discerned within the tumor area of the post-contrast images (4 h) due to the accumulation of iron oxide. Importantly, the spatial distribution of signal loss in the group LS174T RGD **(Figure 2.2E)** differed from all the other investigated groups **(Figure 2.2F-H)**. While in the latter groups the nanoparticles seemed to be distributed rather homogenously, in the case of the LS174T tumors injected with the RGD-functionalized nanoemulsions, the contrast agent was prevailingly confined to the periphery of the tumors.

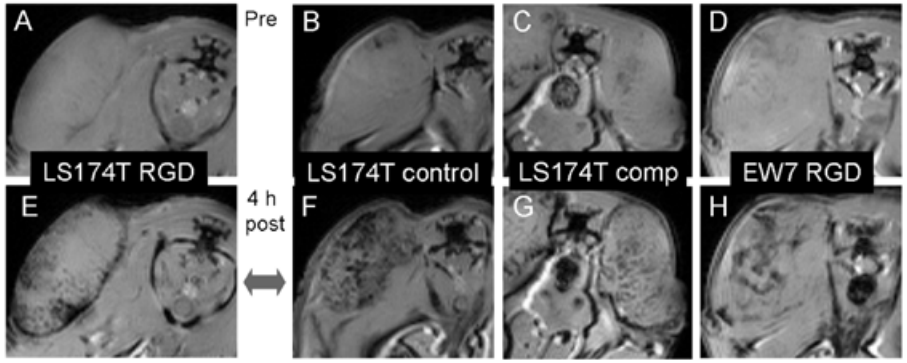

Figure 2.2

T_2*-weighted gradient echo pre- **(A-D)** and post-injection **(E-H)** (4 h, 36.7 mg/kg Fe) MR images of subcutaneous LS174T and EW7 tumors in Swiss nude mice (position unchanged in coil). The tumors of the LS174T RGD group, i.v. injected with RGD-conjugated nanoparticles, show as the only group a hypointense signal distribution (due to iron oxide accumulation) confined to the periphery of the tumor **(E)**. The other groups, injected either with the unconjugated particles **(F)**, after a competition experiment **(G)**, or in the case of the other tumor model (EW7) characterized by a lower angiogenesis level **(H)**, are rather marked by a homogeneous pattern spread throughout the entire tumor section (TR = 120 ms; TE = 3 ms; flip angel 30°; Bruker 9.4 T).

The statistical analysis of the acquired T_2*-weighted tumor images (details see Methods section) revealed a very high reproducibility of the performed experiments **(Figure 2.3A)**. As seen in the chart showing the percentage of reduced pixels per ROI plotted against the corresponding ROI, two different groups of mice injected with different batches of the RGD-conjugated contrast agent yielded an almost identical signal loss pattern across the tumor (* P < 0.01 between ROI 1 and ROI 5). In comparison to the high statistically significant difference of pixels with reduced intensity between the tumor-periphery and the core (P = 0.008) in the targeted LS174T RGD model, the analysis of the EW7 RGD as well as the LS174T control group revealed no difference (EW7 RGD: P = 0.88; LS174T control: P = 0.204; **Figure 2.3B**). The evaluation of the competition group that was injected first with twice the amount of targeted nanoparticles lacking iron oxide, followed by a second injection with targeted nanoparticles carrying iron oxide, resulted in a distribution with a trend towards the control **(Figure 2.3D)**.

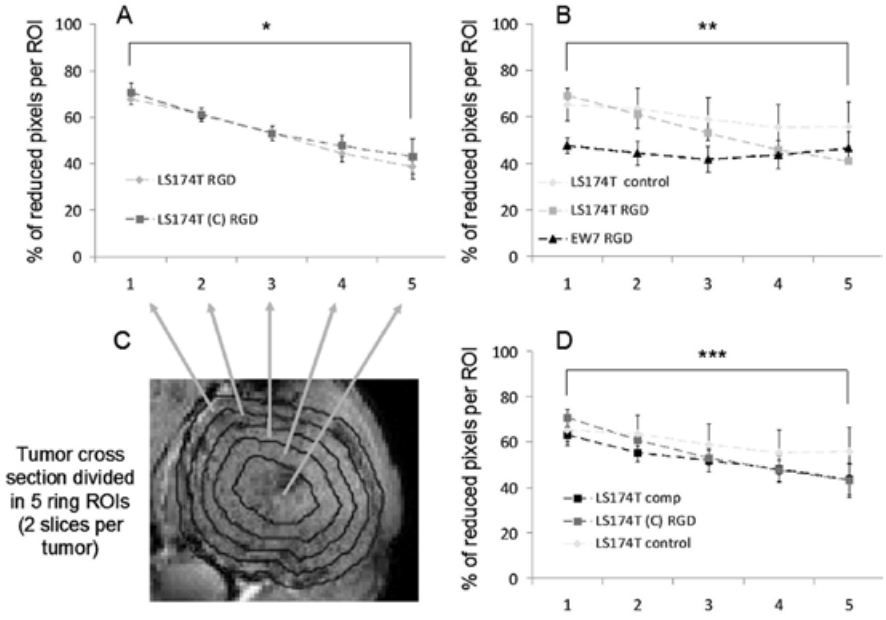

Figure 2.3

For the evaluation of the MR images, the tumor area was divided into five ROIs **(C)** and the percentage of reduced pixels (pre vs post) per ROI (RP/ROI) plotted against the corresponding ROI **(A, B, D)**. A very high grade of reproducibility could be achieved when comparing two different mice groups injected just with different batches of the same RGD-conjugated nanoparticles **(A)** (* P < 0.01 between ROI 1 and ROI 5). The two different tumor models injected with RGD-nanoemulsions show a very distinct rate of decrease in RP/ROI from ROI 1 to ROI 5 **(B)** (** LS174T RGD: P = 0.008; EW7 RGD: P = 0.88; LS174T control: P = 0.204), indicating a considerably different angiogenesis level. While the competition group LS174 (C) RGD was still significantly different between ROI 1 and 5, a shift of the entire pattern towards the one of the control can be observed **(D)** (*** LS174T (C) RGD: P < 0.05; LS174T comp: P < 0.05; LS174T control: P > 0.05). Mean values ± SE.

2.4.2 *In vivo* NIRF imaging Representative examples of mice for the different groups display the results of the time resolved accumulation of the nanoemulsions in the tumors by using *in vivo* fluorescence imaging within a period of 24 hours **(Figure 2.4)**. The normalized enhancement ratio of the Cy7 fluorescence in percent was plotted against the time and revealed a statistically difference (P < 0.05) between all three investigated groups for the time points 1, 2, 4 and 6 h **(Figure 2.5)**. The LS174T RGD group was the one with the fastest accumulation kinetic. The analysis demonstrated that the difference in tumor fluorescence intensity between the two different cancer models was higher than the LS174T RGD compared to the LS174T control for those time points. The mice were sacrificed 24 h post injection, perfused and the organs as well as tumors imaged **(Figure 2.6)**. The analysis of the fluorescence intensities revealed a high dose-percentage of the contrast agent in the tumors normalized to the liver for the LS174T RGD mice (35 %) compared to the EW7 RGD (17 %) and the LS174T control (19 %) (details see Methods section). The result of the analysis of the organ fluorescence (I) normalized to the sum total of the fluorescence of the organs and the tumors (Io) is depicted in **Figure 2.6D**.

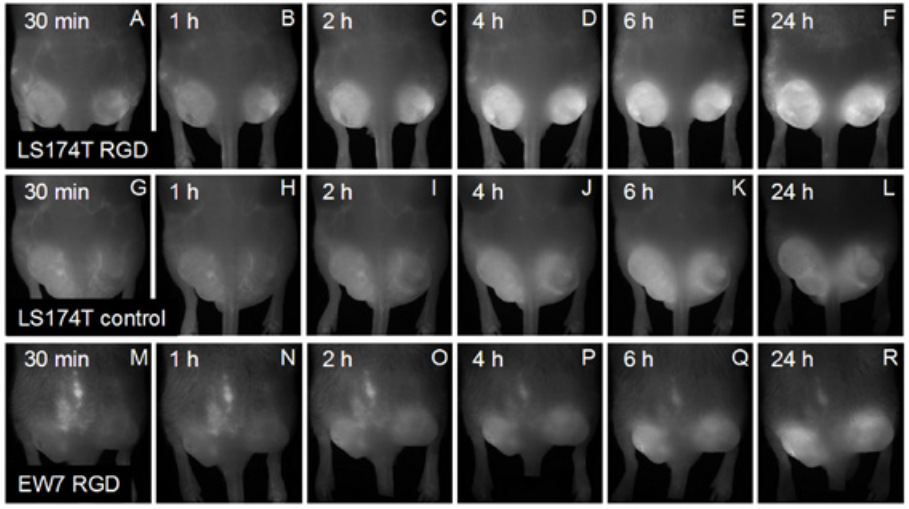

Figure 2.4

Fluorescence images (Cy7) of representatives of the two mice groups injected with RGD-targeted nanoemulsions (LS174T RGD: **A-F**; EW7 RGD: **M-R**) as well as of the group injected with untargeted nanoemulsions (LS174T control: **G-L**) showing the accumulation of the contrast agent in subcutaneous tumor-bearing nude mice over a time period of 24 h.

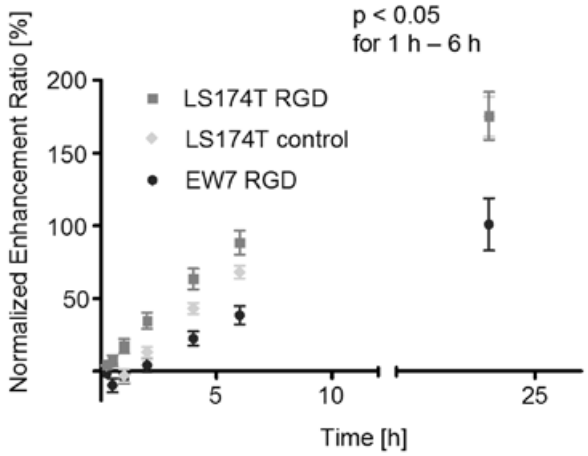

Figure 2.5

Time dependent tumor fluorescence signal of the three mice groups normalized to the skin and corrected for the blood pool effect after injection. The analysis of the kinetic revealed a statistically significant difference (P < 0.05) between the three groups at the time points 1 h, 2 h, 4 h and 6 h post-injection (LS174T RGD, LS174T control: n = 12 tumors; EW7 RGD: n = 10 tumors, mean values ± SE).

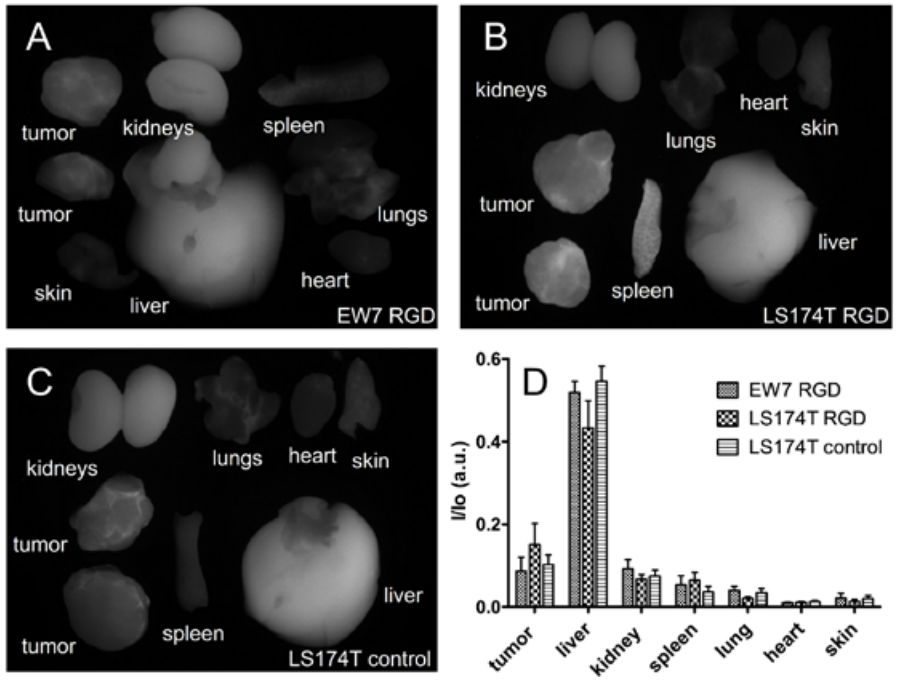

Figure 2.6

Fluorescence images (Cy7) of excised tumors and organs **(A-C)** of one representative mouse from each group, 24 h after injection of the nanoparticles. **(D)** The relative fluorescence counts of each organ or tumor were normalized to the sum total of all organs including the two tumors per mouse and averaged for all the mice within a group (LS174T RGD: n = 6 mice, LS174T control: n = 3 mice, EW7 RGD: n = 5 mice, mean value + SD).

2.4.3 Histological analysis Perls' staining was performed on fixed tumor sections to confirm the presence of iron oxide delivered by the nanocarrier 24 h after i.v. administration. The results depicted in **Figure 2.7A-C** demonstrate the association of the particles with tumor vessels in the example of LS174T RGD, while for the LS174T control tumors, the distribution was rather within the tissue **(Figure 2.7D)**.

CLSM imaging corroborated the co-localization of the targeted nanoparticles (RhodamineB-fluorescence)withmicrovessels(isolectin-AlexaFluor488stained;**Figure2.7E-H**), while control particles were again spread within the tumor tissue **(Figure 2.7I-L)**.

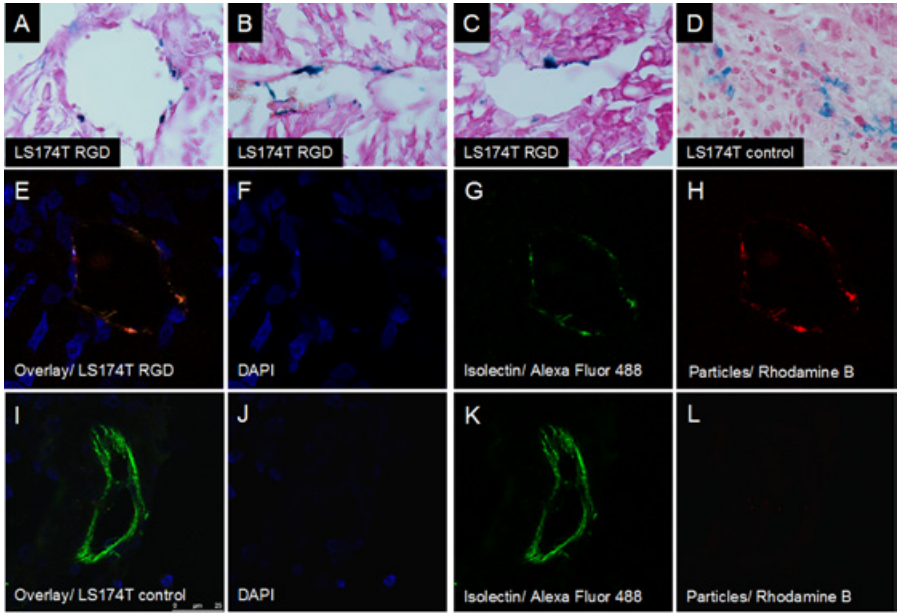

Figure 2.7

Post mortem Perls' staining for iron oxide showed accumulation of the nanoparticles in the tumor vessel endothelium **(A-C)** as compared to the rather homogenous distribution within the tumor tissue in the control **(D)**. Confocal laser scanning microscopy corroborated these results, where the red fluorescence (Rhodamine B) of RGD conjugated nanoparticles could be co-localized with the fluorescently labeled vessel marker isolectin GS-IB4 **(E-H)**, contrary to the unconjugated control particles **(I-L)**.

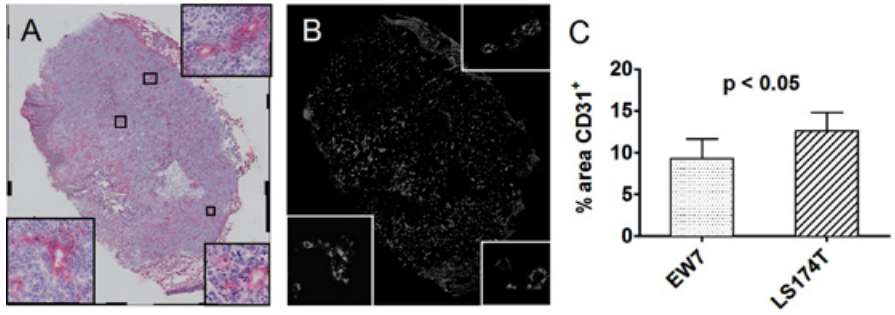

Figure 2.8

Histological CD31 staining was performed for EW7 and LS174T tumors to determine the microvessel density. One entire tumor section was captured with an automated brightfield microscope (20x objective) generating multiple images which were stitched together to one. **(A)** shows an example of a high-resolution image of a stitched CD31-stained EW7 tumor section. The red brightfield CD31 stain was color-selected to generate a black and white image with just the visible CD31 signal **(B)** and the area fraction in percent was determined. The three insets show the vessel staining in the original magnification **(A)** with the corresponding black and white equivalents **(B)**. There was a statistically significant difference ($P < 0.05$) in CD31 signal between the two chosen tumor models **(C)** (EW7: n = 4 tumors; LS174T: n = 5 tumors; mean values + SD).

The MVD of the two different tumor models was determined by using CD31 staining. Tumor areas of one slide were photographed sequentially with a system using a 20x objective and then auto-stitched to display an entire section (CD31+: red color, **Figure 2.8A**). These high-resolution images were transformed by using appropriate software into a corresponding black and white image with white representing positive CD31 signal **(Figure 2.8B)**. The result of the percentage area analysis confirmed the statistically significant higher MVD of the LS174T tumors compared to the EW7 **(Figure 2.8C)**.

2.5 DISCUSSION

In the present study we demonstrated that our previously developed nanoparticle platform can be functionalized with RGD to serve as a contrast agent that allows the detection of ongoing angiogenesis and the distinction between angiogenesis intensities of different tumor models by two complementary and non-invasive imaging modalities, i.e., MRI and NIRF. The combination of both modalities provided spatiotemporal information about the accumulation and fate of the probe. Analysis of the MR images revealed a significant difference in distribution of the RGD-targeted nanoemulsions in the fast growing and highly vascularized human colorectal LS174T model compared to the EW7 mo-

del, characterized by slow growth (50 % of LS174T), highly elevated vascular mimicry in the tumor rim [32] and lower MVD [31]. In the case of the EW7 model with a lower angiogenesis level and vascular mimicry, the majority of the RGD nanoparticle uptake occurred non-specifically and might explain the relatively homogeneous nanoparticle distribution pattern, which was similar to the LS174T control group injected with the untargeted nanoparticles. In this way the EW7 RGD group served as a control for both, i.e., the targeted as well as untargeted LS174T groups. On the contrary, in the LS174T RGD nanoparticle tumors the high expression of the $\alpha_v\beta_3$ integrin, predominantly observed at the periphery of the tumor, caused a shift away from the homogenous accumulation pattern towards a pattern corresponding prevalently to documented expression of the integrin [36]. Since $\alpha_v\beta_3$ integrin expressed at endothelial cells is directly accessible from the circulation, targeting of RGD-functionalized nanoparticles is faster than the passive accumulation due to the EPR effect. Therefore the first one of these two competing processes dominates the second in the case of a high receptor expression at the tumor vasculature [37-38].

While MRI served to show the accumulation pattern within the tumors 4 h after injection, NIRF imaging provided time resolved information about the fate of the particles on the whole tumor level for a period of 24 h. The statistically significant difference in accumulation kinetics between the three investigated groups for the time points up to 6 h was as follows: LS174T RGD > LS174T control > EW7 RGD.

Histological examination served to corroborate the accumulation of nanoparticles in the tumor tissue. Perls' staining, used to visualize iron oxide deposits in tissue, demonstrated the co-localization of the targeted particles with the vessel walls, while untargeted nanoemulsions were found extravasated and diffusely spread throughout the tissue. CLSM of Rhodamine B-labeled nanoparticles corroborated the Perls' staining results. The biodistribution, assessed by measuring the Cy7 fluorescence counts of the whole organs and the tumors after excision, revealed a high dose-percentage of the targeted contrast agent in the LS174T tumors (normalized to the liver: 35 %), a highly desirable property of a contrast agent.

The MVD of the two used tumor models was assessed using CD31 staining and revealed LS174T tumors to have a much higher angiogenesis level than the EW7 counterpart. It is important to stress that such an assessment of MVD alone does not provide information about the proliferating fraction of endothelial cells within a tumor at a given time point. However, in most mouse models - unlike human tumors - high MVD is associated to intense ongoing angiogenesis [39]. Usually, the degree of MVD increases with tumor types that have higher rates of nutrient or oxygen consumption compared to others with a lower-level metabolic requirement. While MVD has often been shown to be a prognostic indicator in many tumor studies, its measurement for monitoring of anti-angiogenic therapy has not been demonstrated to be reliable. A decrease in MVD following anti-angiogenic therapy is certainly a confirmation of its efficacy, but an unchanged MVD not necessarily proof for its inefficacy [10]. In cases of equal tumor cell and endothelial cell drop-out, no changes in MVD are detectable, as e.g., shown in a case of multiple myeloma treatment with thalidomide, where not all tumor regressions were associated with a MVD decrease [40].

In light of this, since our nanoparticles were shown to be able to distinguish between different levels of angiogenesis in two distinct tumor models by directly targeting to the $\alpha_v\beta_3$ receptor as visualized by NIRF and MRI, it is imaginable that they could be not only used as a non-invasive contrast agent for angiogenic phenotyping, but also to reliably monitor response to anti-angiogenic therapy, like we have shown with paramagnetic liposomes [41]. The efficacy of the latter then would be expressed as a change in nanoparticle kinetics monitored by NIRF imaging and/or differences in T_2* signal loss pattern using MRI after injection over time. Moreover, we found in a very recent parallel study that our nanoparticle platform could be modified by implementation of cholesterol to form a stable nanocarrier with a PEG content that could be judiciously varied in a range of 5-50 mol %. Lower PEG contents proved to even highly increase its targeting capabilities to the $\alpha_v\beta_3$ receptors of newly forming vessels [42]. An improved modification of our nanoemulsion of this sort might result in a much higher sensitivity for detecting changes in neoangiogenesis during the course of treatment. Furthermore, by using this modified version of our nanoemulsion formulation, it could be convincingly shown that RGD-targeted nanoparticles began to accumulate as early as 10-30 min after i.v. injection and gave a clear binding pattern 2 h post administration. In contrast, untargeted control particles showed almost no accumulation within the first 30 min, and a very heterogeneous pattern after 2-4 h. Only 8 h after injection all the particles extravasated into the tumor tissue. These data corroborate our finding that RGD-targeted nanoparticles show a higher accumulation compared to the untargeted control within the first hours after i.v. administration, as presented in the 24 h kinetic herein. Another recent study using RGD-targeted, superparamagnetic polymeric micelle nanoprobes, combined with T_2*-weighted time-resolved-MRI, demonstrated an increased accumulation of the probe over the control in subcutaneous tumor animal models during the first 30 min after i.v. injection, showing an onset already within the first 5 min [38].

In a recently published study with a smaller, 50 nm version of the RGD nanoemulsion presented here, which also had hydrophobic glucocorticoids incorporated, we achieved significant tumor growth inhibition, demonstrating the versatility of this nanocarrier and its use for theranostics [42].

2.6 CONCLUSIONS

In conclusion, the RGD-conjugated nanoparticle contrast agent presented in this study can be used to noninvasively investigate differences in angiogenic activity in tumors and for angiogenesis phenotyping of tumors. Its biodegradability, flexibility and the capability of encapsulating hydrophobic materials/drugs make this platform suitable for theranostics and the tailored anti-angiogenesis combination therapy with highly potent, but water insoluble cytotoxic agents.

2.7 REFERENCES

1. Jain RK, Stylianopoulos T (2010) Delivering nanomedicine to solid tumors. Nat Rev Clin Oncol 7:653-664.
2. Folkman J (2007) Angiogenesis: an organizing principle for drug dis covery? Nat Rev Drug Discov 6:273-286.
3. Presta LG, Chen H, O'Connor SJ, Chisholm V, Meng YG, Krummen L, Winkler M, Ferrara N (1997) Humanization of an anti-vascular endothelial growth factor monoclonal antibody for the therapy of solid tumors and other disorders. Cancer Res 57:4593-4599.
4. Hurwitz H, Fehrenbacher L, Novotny W, Cartwright T, Hainsworth J, Heim W, Berlin J, Baron A, Griffing S, Holmgren E, Ferrara N, Fyfe G, Rogers B, Ross R, Kabbinavar F (2004) Bevacizumab plus irinotecan, fluorouracil, and leucovorin for metastatic colorectal cancer. N Engl J Med 350:2335-2342.
5. Chung AS, Lee J, Ferrara N (2010) Targeting the tumour vasculature: insights from physiological angiogenesis. Nat Rev Cancer 10:505-514.
6. Shojaei F (2012) Anti-angiogenesis therapy in cancer: current challenges and future perspectives. Cancer Lett 320:130-137.
7. Ebos JM, Kerbel RS (2011) Anti-angiogenic therapy: impact on invasion, disease progression, and metastasis. Nat Rev Clin Oncol 8:210-221.
8. Moreno Garcia V, Basu B, Molife LR, Kaye SB (2012) Combining anti-angiogenics to overcome resistance: rationale and clinical experience. Clin Cancer Res 18:3750-3761.
9. Lederle W, Palmowski M, Kiessling F (2012) Imaging in the age of molecular medicine: monitoring of anti-angiogenic treatments. Curr Pharm Biotechnol 13:595-608.
10. Nico B, Benagiano V, Mangieri D, Maruotti N, Vacca A, Ribatti D (2008) Evaluation of microvascular density in tumors: pro and contra. Histol Histopathol 23:601-607.
11. Calcagno C, Mani V, Ramachandran S, Fayad ZA (2010) Dynamic contrast enhanced (DCE) magnetic resonance imaging (MRI) of atherosclerotic pla que angiogenesis. Angiogenesis 13:87-99.
12. Cao Y (2011) The promise of dynamic contrast-enhanced imaging in radiation therapy. Semin Radiat Oncol 21:147-156.
13. Deshpande N, Pysz MA, Willmann JK (2010) Molecular ultrasound assessment of tumor angiogenesis. Angiogenesis 13:175-188.
14. Nagengast WB, Lub-de Hooge MN, Oosting SF, den Dunnen WF, Warnders FJ, Brouwers AH, de Jong JR, Price PM, Hollema H, Hospers GA, Elsinga PH, Hesselink JW, Gietema JA, de Vries EG (2011) VEGF-PET imaging is a noninvasive biomarker showing differential changes in the tumor during sunitinib treatment. Cancer Res 71:143-153.
15. Hak S, Reitan NK, Haraldseth O, de Lange Davies C (2010) Intravital microscopy in window chambers: a unique tool to study tumor angiogenesis and delivery of nanoparticles. Angiogenesis 13:113-130.
16. Snoeks TJ, Lowik CW, Kaijzel EL (2010) *'In vivo'* optical approaches to angiogenesis imaging. Angiogenesis 13:135-147.
17. De Lussanet QG, Beets-Tan RG, Backes WH, Van der Schaft DW, Van Engelshoven JM, Mayo KH, Griffioen AW (2004) Dynamic contrast-enhanced magnetic resonance imaging at 1.5 Tesla with gadopentetate dimeglumine to assess the angiostatic effects of anginex in mice. Eur J Cancer 40:1262-1268.

18. De Lussanet QG, Backes WH, Griffioen AW, Padhani AR, Baeten CI, Van Baardwijk A, Lambin P, Beets GL, Van Engelshoven JM, Beets-Tan RG (2005) Dynamic contrast-enhanced magnetic resonance imaging of radiation therapy-induced microcirculation changes in rectal cancer. Int J Radiat Oncol Biol Phys 63:1309-1315.

19. Leach MO, Morgan B, Tofts PS, Buckley DL, Huang W, Horsfield MA, Chenevert TL, Collins DJ, Jackson A, Lomas D, Whitcher B, Clarke L, Plummer R, Judson I, Jones R, Alonzi R, Brunner T, Koh DM, Murphy P, Waterton JC, Parker G, Graves MJ, Scheenen TW, Redpath TW, Orton M, Karczmar G, Huisman H, Barentsz J, Padhani A (2012) Imaging vascular function for early stage clinical trials using dynamic contrast-enhanced magnetic resonance imaging. Eur Radiol 22:1451-1464.

20. Barrett T, Brechbiel M, Bernardo M, Choyke PL (2007) MRI of tumor angiogenesis. J Magn Reson Imaging 26:235-249.

21. Hahn OM, Yang C, Medved M, Karczmar G, Kistner E, Karrison T, Manchen E, Mitchell M, Ratain MJ, Stadler WM (2008) Dynamic contrast-enhanced magnetic resonance imaging pharmacodynamic biomarker study of sorafenib in metastatic renal carcinoma. J Clin Oncol 26:4572-4578.

22. Jarzyna PA, Gianella A, Skajaa T, Knudsen G, Deddens LH, Cormode DP, Fayad ZA, Mulder WJ (2010) Multifunctional imaging nanoprobes. Wiley Interdiscip Rev Nanomed Nanobiotechnol 2:138-150.

23. Medarova Z, Rashkovetsky L, Pantazopoulos P, Moore A (2009) Multiparametric monitoring of tumor response to chemotherapy by noninvasive imaging. Cancer Res 69:1182-1189.

24. Mulder WJ, Griffioen AW (2010) Imaging of angiogenesis. Angiogenesis 13:71-74.

25. Akers WJ, Zhang Z, Berezin M, Ye Y, Agee A, Guo K, Fuhrhop RW, Wickline SA, Lanza GM, Achilefu S (2010) Targeting of alpha(nu)beta(3)-integrins expressed on tumor tissue and neovasculature using fluorescent small molecules and nanoparticles. Nanomedicine (Lond) 5:715-726.

26. Chen W, Jarzyna PA, van Tilborg GA, Nguyen VA, Cormode DP, Klink A, Griffioen AW, Randolph GJ, Fisher EA, Mulder WJ, Fayad ZA (2010) RGD peptide functionalized and reconstituted high-density lipoprotein nanoparticles as a versatile and multimodal tumor targeting molecular imaging probe. FASEB J 24:1689-1699.

27. Van Tilborg GA, Mulder WJ, Van der Schaft DW, Reutelingsperger CP, Griffioen AW, Strijkers GJ, Nicolay K (2008) Improved magnetic resonance molecular imaging of tumor angiogenesis by avidin-induced clearance of nonbound bimodal liposomes. Neoplasia 10:1459-1469.

28. Lanza GM, Caruthers SD, Winter PM, Hughes MS, Schmieder AH, Hu G, Wickline SA (2010) Angiogenesis imaging with vascular-constrained particles: the why and how. Eur J N ucl Med Mol Imaging 37 Suppl 1:S114-126.

29. Jarzyna PA, Skajaa T, Gianella A, Cormode DP, Samber DD, Dickson SD, Chen W, Griffioen AW, Fayad ZA, Mulder WJ (2009) Iron oxide core oil-in-water emulsions as a mul tifunctional nanoparticle platform for tumor targeting and imaging. Biomaterials 30:6947-6954.

30. Fukumura D, Yuan F, Monsky WL, Chen Y, Jain RK (1997) Effect of host microenvironment on the micro-circulation of human colon adenocarcinoma. Am J Pathol 151:679-688.

31. Van der Schaft DW, Hillen F, Pauwels P, Kirschmann DA, Castermans K, Egbrink MG, Tran MG, Sciot R, Hauben E, Hogendoorn PC, Delattre O, Maxwell PH, Hendrix MJ, Griffioen AW (2005) Tumor cell plasticity in Ewing sarcoma, an alternative circulatory system stimulated by hypoxia. Cancer Res 65:11520-11528.

32. Hillen F, Kaijzel EL, Castermans K, oude Egbrink MG, Lowik CW, Griffioen AW (2008) A transgenic Tie2-GFP athymic mouse model; a tool for vascular biology in xenograft tumors. Biochem Biophys Res Commun 368:364-367.

33. Kim S, Lim YT, Soltesz EG, De Grand AM, Lee J, Nakayama A, Parker JA, Mihaljevic T, Laurence RG, Dor DM, Cohn LH, Bawendi MG, Frangioni JV (2004) Near-infrared fluorescent type II quantum dots for sentinel lymph node mapping. Nat Biotechnol 22:93-97.

34. Nakayama A, del Monte F, Hajjar RJ, Frangioni JV (2002) Functional near-infrared fluorescence imaging for cardiac surgery and targeted gene therapy. Mol Imaging 1:365-377.

35. De Grand AM, Frangioni JV (2003) An operational near-infrared fluorescence imaging system prototype for large animal surgery. Technology in cancer research & treatment 2:553-562.

36. Mulder WJ, Strijkers GJ, Habets JW, Bleeker EJ, Van der Schaft DW, Storm G, Koning GA, Griffioen AW, Nicolay K (2005) MR molecular imaging and fluorescence microscopy for identification of activated tumor endothelium using a bimodal lipidic nanoparticle. FASEB J 19:2008-2010.

37. Hak S, Helgesen E, Hektoen HH, Huuse EM, Jarzyna PA, Mulder WJ, Haraldseth O, Davies Cde L (2012) The effect of nanoparticle polyethylene glycol surface density on ligand-directed tumor targeting studied *in vivo* by dual modality imaging. ACS Nano 6:5648-5658.

38. Kessinger CW, Togao O, Khemtong C, Huang G, Takahashi M, Gao J (2011) Investigation of *in vivo* targeting kinetics of alpha(v)beta(3)-specific superparamagnetic nanoprobes by time-resolved MRI. Theranostics 1:263-273.

39. Vermeulen PB, Gasparini G, Fox SB, Colpaert C, Marson LP, Gion M, Belien JA, de Waal RM, Van Marck E, Magnani E, Weidner N, Harris AL, Dirix LY (2002) Second international consensus on the methodology and criteria of evaluation of angiogenesis quantification in solid human tumours. Eur J Cancer 38:1564-1579.

40. Singhal S, Mehta J, Desikan R, Ayers D, Roberson P, Eddlemon P, Munshi N, Anaissie E, Wilson C, Dhodapkar M, Zeddis J, Barlogie B (1999) Anti tumor activity of thalidomide in re fractory multiple myeloma. N Engl J Med 341:1565-1571.

41. Mulder WJ, van der Schaft DW, Hautvast PA, Strijkers GJ, Koning GA, Storm G, Mayo KH, Griffioen AW, Nicolay K (2007) Early *in vivo* assessment of angiostatic therapy efficacy by molecular MRI. FASEB J 21:378-383.

42. Gianella A, Jarzyna PA, Mani V, Ramachandran S, Calcagno C, Tang J, Kann B, Dijk WJ, Thijssen VL, Griffioen AW, Storm G, Fayad ZA, Mulder WJ (2011) Multifunctional nanoemulsion platform for imaging guided therapy evaluated in experimental cancer. ACS Nano 5:4422-4433.

αPECAM-1-MPIO AS MR CONTRAST AGENT FOR DETECTION OF VASCULAR REMODELING AFTER STROKE

Based on:
Lisette H. Deddens, Geralda A.F. van Tilborg, Annette van der Toorn, Helga E. de Vries and Rick M. Dijkhuizen.
αPECAM-1-targeted micron-sized particles of iron oxide as MRI contrast agent for detection of vascular remodeling after cerebral ischemia.
Contrast Media Mol Imaging **2013** (in press)

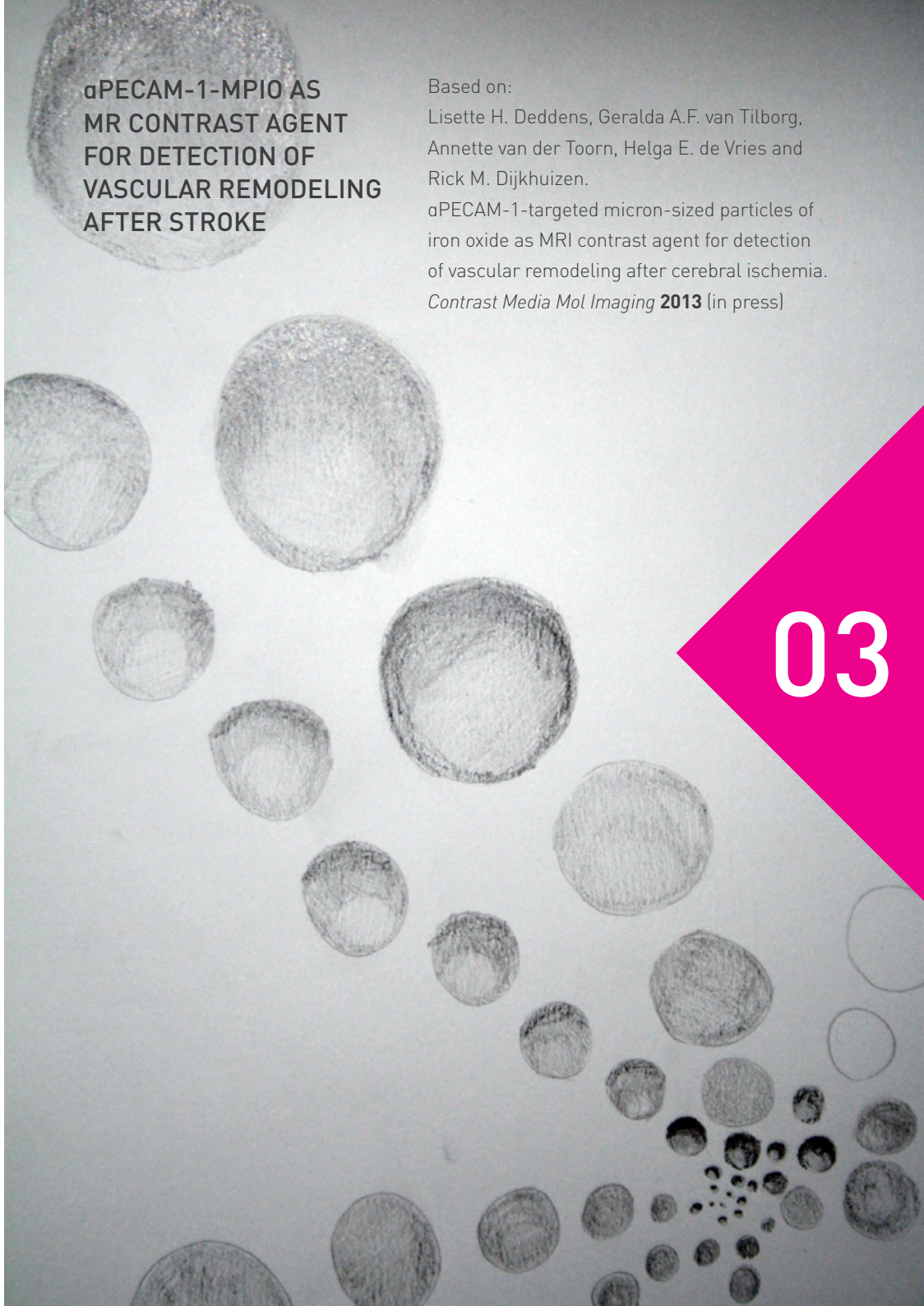

03

3.1 ABSTRACT

An increasing amount of studies have provided evidence for vascular remodeling, e.g., angiogenesis, after cerebral ischemia, which may play a significant role in post-stroke brain plasticity and recovery. Molecular imaging can provide unique *in vivo* whole-brain information on alterations in the expression of specific endothelial markers. A possible target for molecular magnetic resonance imaging (MRI) of post-stroke (neo)vascularization is platelet endothelial cell adhesion molecule-1 (PECAM-1). Here we describe significantly increased PECAM-1 mRNA levels in ipsilesional brain tissue at 6 h, 24 h and 3 days after transient middle cerebral artery occlusion in mice, and elevated PECAM-1 staining throughout the lesion at 3, 7 and 21 days post-stroke. The potential of micron-sized particles of iron oxide (MPIO) conjugated with PECAM-1-targeted antibodies, i.e., αPECAM-1-MPIO, to expose stroke-induced PECAM-1 upregulation with molecular MRI was assessed. *In vitro* studies demonstrated that PECAM-1-expressing brain endothelial cells could be effectively labeled with αPECAM-1-MPIO, giving rise to a fourfold increase in MRI relaxation rate R_2. Injection of near-infrared fluorescent dye-labeled αPECAM-1 showed target specificity and dose efficiency of the antibody for detection of brain endothelial cells at 3 days post-stroke. However, *in vivo* molecular MRI at 3 and 7 days after stroke revealed no αPECAM-1-MPIO-based contrast enhancement, which was corroborated by absence of αPECAM-1-MPIO in *post mortem* brain tissue. This indicates that this molecular MRI approach, which has been proven successful for *in vivo* detection of other types of cell adhesion molecules, is not invariably effective for MRI-based assessment of stroke-induced alterations in expression of cerebrovascular markers.

3.2 INTRODUCTION

Stroke is one of the leading causes of death and disability in the Western world. It is the result of occlusion or rupture of a brain artery, leading to focal loss of blood flow and brain function. Ischemic stroke accounts for the majority of the cases. The time window of the only FDA-approved treatment for ischemic stroke, thrombolysis with recombinant tissue plasminogen activator (rtPA), is limited to 4.5 h after stroke onset, leaving 95 % of the patients untreated [1]. Interestingly, experimental studies suggest that restorative cell-based and pharmacological therapies have potential to improve functional outcome when initiated days to weeks after stroke [2-3]. These therapies may stimulate endogenous processes that contribute to neuronal survival and regeneration [4-5]. Formation of new blood vessels, i.e., arteriogenesis and angiogenesis, are critical components in normal tissue growth and development, and has also been observed in post-stroke brain tissue, promoting recovery [6-12]. However, the process of vascular remodeling in relation to preservation or restoration of brain functioning after cerebral ischemia remains unknown.

Magnetic resonance imaging (MRI) provides a powerful tool to non-invasively assess the evolution of various indices that can characterize cerebral tissue status after stroke [13-15]. Contrast in MR images can be manipulated by exploiting differences in intrinsic, biophysical tissue properties such as proton density, signal decay time-constants (T_1, T_2, T_2*), oxygenation state, magnetic susceptibility, diffusion, perfusion and flow. Additionally, exogenous contrast agents (e.g., gadolinium chelates and iron oxide particles) can be applied to alter some of these endogenous contrast-generating mechanisms, which improve contrast and allow revealing of otherwise indiscernible features. MRI, with and without contrast enhancement, has been effectively applied to measure (changes in) vascular parameters such as cerebral blood flow (CBF), cerebral blood volume (CBV), microvessel density (MVD) and vessel size index (VSI) [8, 16-19]. Furthermore, recent advancements in contrast agent design and synthesis have created promising opportunities for MRI of molecular vascular markers [20], offering the potential for *in vivo* assessment of additional and unmapped features of vascular status in normal and diseased brain.

We speculate that molecular MR imaging can provide unique information on the process of vascular remodeling after cerebral ischemia that may contribute to elucidation of endogenous repair mechanisms and identification of specific targets for restorative cell-based and pharmacological therapies. Therefore, we developed a novel MRI approach to detect a molecular vascular marker with use of a specifically targeted contrast agent. As potential target for molecular MRI of vascular remodeling after stroke, we chose platelet endothelial cell adhesion molecule-1 (PECAM-1) - also known as cluster of differentiation 31 (CD31) - which is an established endothelial marker that has been successfully applied for measurement of (neo)vascularization after experimental stroke [21]. PECAM-1 is found on the surface of platelets, neutrophils, monocytes and constitutively expressed on endothelial cells. A marked increase after cerebral ischemia has been observed in post-stroke brain tissue in experimental setting [21-22], suggestive of increased vascular density, e.g., through angiogenesis. In this study we explored the potential of MRI of PECAM-1-targeted micron-sized particles of iron oxide (MPIO) to detect vascular remodeling at 3 and 7 days after experimental stroke in mice.

3.3 MATERIALS AND METHODS

3.3.1 Materials ProMag™ 1 Series, Bind-IT™ MPIO (25 mg MPIO/ml, 26.5 % iron-content) were obtained from Bangs Laboratories, Inc. (Fishers, IN, USA). Diaminobenzidine solution (DAB+) was obtained from Sigma-Aldrich (St. Louis, MO, USA). A monoclonal antibody against mouse PECAM-1 (αPECAM-1) was produced in house from ER-MP12 hybridoma. Near-infrared fluorescent dye-labeled αPECAM-1 (αPECAM-1-NIRF) was obtained by labeling αPECAM-1 with Alexa647 using an Alexa647 protein labeling kit of Invitrogen (Carlsbad, CA, USA) according to the manufacturer's description; biotinylation was accomplished by labeling αPECAM-1 with biotin (αPECAM-1-biotin). Irrelevant isotype control immunoglobulin G antibody (IgG, RTK4530) was obtained from BioLegend (San Diego, CA, USA), near-infrared fluorescent dye-labeled IgG (IgG-NIRF; IgG-eFluor660) was obtained from eBioscience (Vienna, Austria). Horseradish peroxidase-labeled streptavidin (HRP strep) was obtained from DAKO (Glostrup, Denmark). Primers were obtained from Ocimum Biosolutions (IJsselstein, The Netherlands).

3.3.2 Preparation of antibody-functionalized MPIO MPIO were extracted from their original buffer by magnetic separation and resuspended in coupling buffer (50 mM 2-(N-morpholino)ethanesulfonic acid (MES); pH 5.2) to a concentration of 25 mg MPIO/ml (6.6 mg iron/ml). Prior to the coupling procedure, αPECAM-1 or IgG were buffer-exchanged to coupling buffer by centrifugation using Vivaspin concentrators (molecular weight cut-off 50 kD; GE Healthcare, Diegem, Belgium) at 4000g, resulting in a final antibody concentration of 1.0 mg/ml. Next, MPIO and αPECAM-1 or IgG were added in a 1:1 (v/v) ratio, vortexed and left to incubate for 60 min at room temperature on a roller-bench. Following incubation, antibody-MPIO were buffer-exchanged to storage solution (150 mM NaCl, 0.002 % azide) by magnetic separation and stored at 4 °C at a concentration of 3.3 mg iron/ml.

3.3.3 *In vitro* cell preparations The mouse brain endothelioma cell line bEnd.5 [23] was maintained in Dulbecco's Modified Eagle Medium (DMEM; Invitrogen, Grand Island, NY, USA) supplemented with 10 % heat-inactivated fetal calf serum (FCS; PAA Laboratories GmbH, Pasching, Austria), 100 U/ml penicillin, 100 µg/ml streptomycin (all obtained from Gibco, Carlsbad, CA, USA) and 5 µM of b-mercaptoethanol. Cells were cultured in non-coated T75 flasks under normal cell culture conditions. bEnd.5 cell cultures at 70-80 % confluence were incubated with αPECAM-1-MPIO or IgG-MPIO (10 µg iron/ml medium; 1 h at 37 °C) (n = 2 per condition). Alternatively, control cell cultures were left untreated (n = 2 per condition). Following incubation, cells were thoroughly washed and subsequently harvested by incubation in EDTA and a mild trypsinization procedure. The resulting cell suspension was washed twice with phosphate-buffered saline (PBS) during centrifugation (1500 rpm, 5 min). Cells were subsequently fixed in 4 % paraformaldehyde in PBS (10 min), washed with PBS twice, and stored in PBS containing 0.002 % azide. The fixed cells were subsequently embedded in a 2 % agarose for measurement of longitudinal and transverse MR relaxation rates, R_1 and R_2, respectively.

3.3.4 MR relaxation rate measurements R_1 and R_2 values of samples embedded in 2 % agarose were measured at room temperature in a 9.4 T 20 cm horizontal bore MR system (Agilent, Palo Alto, CA, USA). R_1 ($1/T_1$) was calculated from T_1 measurements acquired with a Look-Locker inversion recovery sequence (after each inversion pulse 40 acquisitions were done with intervals of 250 ms; repetition time (TR) 20 s; echo time (TE) 3.18 ms; flip angle (FA) 5°; number of averages (NA) 4; matrix size 256 x 256, field-of-view (FOV) 3 x 3 cm^2, slice thickness 400 µm). R_2 ($1/T_2$) was calculated from T_2 measurements with a multi-spin echo sequence (TR 5 s; TE 9-900 ms; number of echoes (NE) 100; NA 4; matrix size 256 x 256, FOV 3 x 3 cm^2, slice thickness 400 µm).

3.3.5 Modified Perls' staining Before embedding in agarose, a small amount of fixed bEnd.5 cells, incubated with antibody-functionalized contrast agent, was used to prepare cytospins for optical visualization of contrast agent binding. A modified Perls' staining [24-25] was performed on cytospins of cells in order to detect iron with light microscopy. Shortly, cytospins were fixed in acetone for 10 min at -20 °C, dried and rehydrated in PBS for 5 min. Endogenous peroxidase was blocked with 1 % H_2O_2 for 15 min, followed by washing the slides under tap water for another 15 min. Slides were washed 3 times for 5 min with Milli-Q, and incubated with freshly prepared Perls' solution (2 N HCl and 2 % ferrocyanide in Milli-Q in 1:1 (v/v) ratio) for 45 min. Slides were again washed under running tap water for 15 min, and washed 3 times for 5 min with Milli-Q, after which they were dipped in a nuclear fast red solution, dehydrated and mounted in Entallan.

3.3.6 *In vivo* mouse stroke model All animal procedures were approved by the Utrecht University Ethical Committee on Animal Experiments, and experiments were performed in accordance with the guidelines of the European Communities Council Directive.
Eight-week-old C57Bl/6 mice, weighing 20 to 25 g (Harlan, Horst, The Netherlands), were anesthetized with isoflurane (3.5 % induction; 1.5-2.0 % maintenance) in air/O_2 (2:1). Body temperature was maintained at 37.0 ± 0.5 °C. Transient focal cerebral

ischemia was induced by 30 min right middle cerebral artery occlusion (MCAo) with an intraluminal filament [26]. In brief, a 7.0 polypropylene suture with a silicon-coated tip (tip diameter of 0.21 mm; Doccol Corporation, Redlands, CA, USA) was introduced into the right external carotid artery and advanced through the internal carotid artery until a slight resistance was felt, indicating that the MCA was occluded. During occlusion, the common carotid artery was clipped. After 30 min, the filament was withdrawn from the internal carotid artery and the clip was removed from the common carotid artery to allow full reperfusion. Before surgery, mice received a 1 ml subcutaneous injection of saline to compensate for loss of water and minerals, and a subcutaneous injection of 0.1 mg/kg buprenorphine (Temgesic; Schering-Plough, Houten, The Netherlands) for (post-)surgical analgesia.

3.3.7 *Post mortem* PECAM-1 immunohistochemistry and qPCR Mice were sacrificed at 6 h, 24 h, 3 days, 7 days or 21 days after MCAo (n = 4 per time-point) with an overdose of pentobarbital (Euthanimal; Alfasan International BV, Woerden, The Netherlands) followed by transcardial perfusion with PBS. Two healthy animals were used as controls (0 h). Brains were excised and snap-frozen in liquid nitrogen and used for immunohistochemistry and quantitative polymerase chain reaction (qPCR).

For immunohistochemistry, cryosections of 10 µm (6 per mouse, ranging from approximately -1 to +1.5 mm from Bregma) were air-dried overnight, and acetone-fixated for 10 min. Dry, fixed sections were hydrated for 15 min in PBS containing 0.1 % bovine serum albumin (BSA). Next, sections were incubated with αPECAM-1-biotin (15 µg antibody/ml) in PBS/0.1 % BSA for 1 h. Subsequently, sections were incubated for 45 min with horseradish peroxidase-labeled streptavidin (HRPstrep; prepared according to the manufacturer's description). Diaminobenzidine solution (DAB) was used as chromogen (according to the manufacturer's description). Between incubation steps, sections were thoroughly washed with PBS. Preparations were incubated with hematoxylin for 1 min after which sections were dehydrated and mounted in Entallan. All steps were performed at room temperature.

For qPCR, messenger ribonucleic acid (mRNA) was isolated from brain tissue from adjacent sets of the tissue sections used for immunohistochemistry, using an mRNA capture kit (Roche Applied Science, Indianapolis, IN, USA) according to the manufacturer's instructions. Two samples per mouse were obtained, being ipsilesional and contralesional hemispheric tissue. For this, 6 brain slices of 10 µm (in the range of -1 to +1.5 mm from Bregma) were hemispherically divided and pooled in an ipsilesional and contralesional tissue fraction. Complimentary deoxyribonucleic acid (cDNA) was synthesized with the Reverse Transcription System kit (Promega Corporation, Madison, WI, USA) following manufacturer's guidelines. qPCR reactions were performed in an ABI7900HT sequence detection system with the SYBR Green method (Applied Biosystems, Foster City, CA, USA). Obtained expression levels of transcripts of PECAM-1 (primer sequences used were PECAM-1-F 5'-TGGTTGTCATTGGAGTGGTC-3' and PECAM-1-R 5'-TTCTCGCTGTTGGAGTTCAG-3') were normalized to glyceraldehyde 3-phosphate dehydrogenase (GAPDH) expression levels (GAPDH-F 5'-CCATGTTCGTCATGGGTGTG-3' and GAPDH-R 5'-GGTGCTAAGCAGTTGGTGGTG-3').

3.3.8 *In vivo* antibody binding Mice underwent MCAo (n = 8) and received a single i.v. dosage of αPECAM-1-NIRF (n = 3) or IgG-NIRF (n = 3), or were untreated (control; n = 2) at 3 days after stroke onset. The amount of injected antibody was equivalent to the dosage of the antibody-MPIO for molecular MRI (see below), i.e., 750 µg/kg body weight. Mice were sacrificed 70 min after antibody injection by an overdose of isoflurane anesthesia followed by transcardial perfusion with PBS. Fresh brains were quickly excised, snap-frozen in liquid nitrogen and stored at -80 °C for *post mortem* immunohistochemical validation.

For immunohistochemistry, cryosections were prepared as described above. Subsequently, tissue was dried and acetone-fixated for 10 min at -20 °C. After the acetone was evaporated, tissue was mounted in 4',6-diamidino-2-phenylindole (DAPI)-containing mounting medium for fluorescence microscopy.

3.3.9 *In vivo* molecular MRI Mice were subjected to MCAo (n = 20) and underwent *in vivo* MRI under general isoflurane anesthesia at 3 days (n = 12) or at 7 days (n = 8) post-stroke. T_2 maps were obtained by multi-spin echo MRI (TR/TE 2300/12-96 ms; NE 8; NA 4; matrix size 192 x 96, FOV 2 x 2 cm^2, 21 slices of 400 µm) in order to determine lesion outline. T_2*-weighted images (3D gradient echo; TR/TE 35/15 ms; NA 8; FA 10°; matrix size 96 x 80 x 160, FOV 1 x 1.2 x 2 cm^3) were acquired before and up to 1 h after i.v. injection of αPECAM-1- or IgG-MPIO (100 µg iron/mouse) at 3 days (n = 6 per group) or 7 days post-stroke (n = 4 per group). One animal (αPECAM-1-MPIO-injected at 3 days post-stroke) was excluded from further analyses due to movement artifacts observed on the T_2*-weighted images. Mice were sacrificed immediately after the last MRI scan by an overdose of isoflurane anesthesia followed by transcardial perfusion with PBS. Fresh brains were quickly excised, snap-frozen in liquid nitrogen and stored at -80 °C for *post mortem* immunohistochemical validation.

For immunohistochemistry validation, cryosections were prepared and stained for PECAM-1 as described above. Tissue was subsequently incubated with freshly prepared Perls' solution (2 N HCl and 2 % ferrocyanide in Milli-Q in 1:1 (v/v) ratio) for 20 min, thoroughly washed with Milli-Q, dipped in a nuclear fast red solution, dehydrated and mounted in Entallan.

3.3.10 MRI analysis Lesions and homologous contralesional tissue were manually outlined on T_2 maps for each animal, as well as the ventricles and corpus callosum. At 3 days post-stroke, tissue was considered to be lesioned when it showed a considerable increase in T_2. At 7 days post-stroke, the lesion core was characterized by heterogeneous signal irregularity. Lesion borderzone tissue was defined by computationally expanding the lesion segmentation two times with a 3 x 3 2D kernel medially, after which the ventricle and corpus callosum segmentations were subtracted. The lesion core, lesion borderzone and contralesional segmentations were used as regions-of-interest (ROIs). To determine the amount of contrast agent accumulation within these ROIs, mean signal intensity (SI) of T_2*-weighted images (corrected for surface coil inhomogeneities) at 1 h after MPIO injection was measured, and expressed as a percentage of corresponding pre-contrast values for each animal according to **(a)**.

(a) $[SI_{(post\text{-}CA)} / SI_{(pre\text{-}CA)}] \cdot 100\ \%$

To calculate within the ROIs the volume percentage of contrast-enhanced (CE) voxels, i.e., voxels that showed contrast-induced hypointensities, hypointense (HI) voxels with more than 2 standard deviations signal difference from pre-contrast T_2*-weighted signal intensity, according to **(b)**, were counted, and the volume of CE voxels was expressed as a percentage of total ROI volume, according to **(c)**.

(b) $SI_{(HI\ voxel)} < SI_{(ROI\ pre\text{-}CA)} - 2 \cdot SD_{(ROI\ pre\text{-}CA)}$

(c) $[(\text{volume of HI voxels}_{(post\text{-}CA)} - \text{volume of HI voxels}_{(pre\text{-}CA)}) / \text{volume of ROI}] \cdot 100\ \%$

3.3.11 Statistical analysis SPSS 19.0 was used for statistical analyses. Comparisons were performed with a univariate ANOVA with Bonferroni correction. Values are presented as mean ± SD. $P < 0.05$ was considered statistically significant.

3.4 RESULTS

3.4.1 Brain tissue exposes increased levels of PECAM-1 mRNA and protein expression after stroke PECAM-1 mRNA and protein expression levels in mouse brain were measured at different time points after experimental unilateral stroke. mRNA levels of *post mortem* contralesional and ipsilesional brain tissue samples were obtained, while protein expression was visualized in the contralesional cortex, the lesion borderzone and lesion core as depicted in **Figure 3.1A**. Ipsilesional PECAM-1 mRNA levels were significantly increased compared to contralesional values at 6 h (6.0 ± 2.1 % vs. 2.4 ± 0.9 %; $P < 0.05$), 24 h (8.3 ± 2.5 % vs. 2.1 ± 0.8 %; $P < 0.05$) and 3 days post-stroke (4.4 ± 1.6 % vs. 1.6 ± 0.8 %; $P < 0.05$), but not at 7 (2.8 ± 1.1 % vs. 1.8 ± 0.6 %) and 21 days post-stroke (3.0 ± 0.9 % vs. 2.1 ± 0.5 %) **(Figure 3.1B)**. Brain sections revealed that the increase in PECAM-1 mRNA in the ipsilesional hemisphere was associated with a marked upregulation of PECAM-1 protein expression in vascular structures in the lesioned tissue, which was already detectable after 6 and 24 h after stroke onset, but intensified at later time points, i.e., 3, 7 and 21 days post-stroke **(Figure 3.1C)**.

3.4.2 PECAM-1-targeted MPIO bind specifically to brain endothelial cells *in vitro* and increase MR transverse relaxation rate The specificity of PECAM-1-targeted contrast agent was tested on mouse brain endothelial cells *in vitro*. Cells were therefore incubated with IgG-MPIO or αPECAM-1-MPIO (10 µg iron/ml medium; 1 h). Light microscopy images of Perls' stained cells showed that cells treated with IgG-MPIO displayed minimal amounts of cell-associated contrast agent, whereas cells treated with αPECAM-1-MPIO showed abundant association **(Figure 3.2A)**, indicating specific binding of PECAM-1-targeted contrast agent *in vitro*. In order to assess whether cell-associated contrast agent was sufficient to generate contrast on MR images, agarose solutions were prepared with no cells, untreated control cells or cells incubated with IgG-MPIO or αPECAM-1-MPIO. No differences were observed in R_1 **(Figure 3.2B)**, but a fourfold significant increase in R_2 was measured for cells incubated with αPECAM-1-MPIO (35.4 ± 2.4 s^{-1}) compared to IgG-MPIO-incubated (8.9 ± 0.5 s^{-1}) or untreated control cells (9.1 ± 0.2 s^{-1}) **(Figure 3.2C)**.

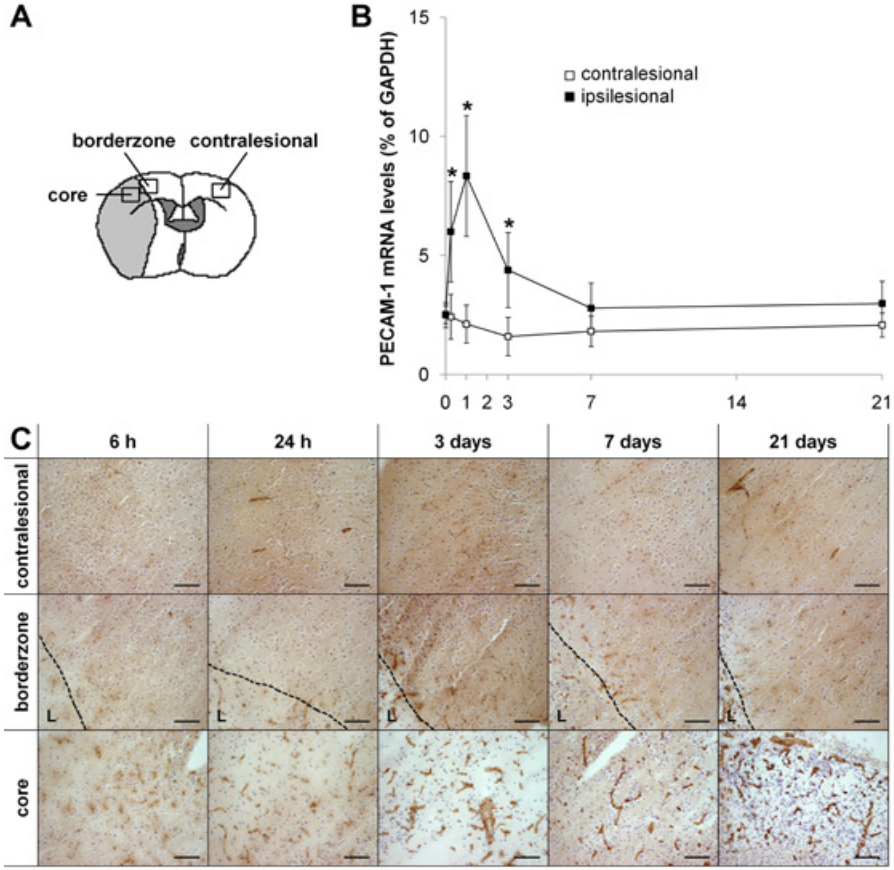

Figure 3.1

Post-stroke brain tissue reveals a significant increase in PECAM-1 mRNA levels and protein expression. **(A)** Schematic representation of the location of specified region of interest, i.e., contralesional and ipsilesional, which contains the lesion core and lesion borderzone. Squares indicate the regions were the light microscopy images were acquired. **(B)** mRNA levels of PECAM-1 (% of GAPDH) at 0 h, 6 h, 24 h, 3 days, 7 days and 21 days post-stroke for ipsilesional and contralesional mouse brain tissue (n = 4 per time-point). * P < 0.05 compared to contralesional brain tissue. **(C)** Light microscopy images (20x; scale bars represent 100 µm) of PECAM-1 protein expression (brown) in contralesional, lesion borderzone and lesion core cortical tissue at 6 h, 24 h, 3 days, 7 days and 21 days after stroke (nuclei: blue; L: lesion).

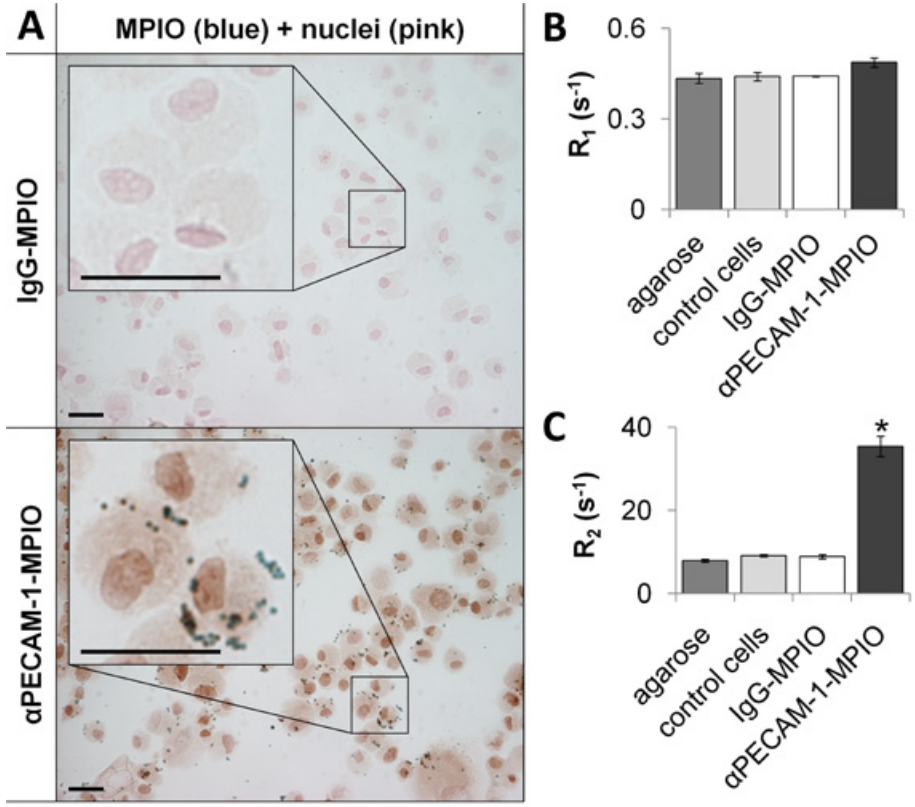

Figure 3.2

MPIO targeted to PECAM-1 bind specifically to brain endothelial cells (bEnd.5), giving rise to a fourfold increase in MR transverse relaxation rate R_2. **(A)** Light microscopy images (20x; scale bars represent 50 µm) of cells incubated with IgG-MPIO (top panel) or αPECAM-1-MPIO (bottom panel). Inserts present 4x magnification (nuclei: pink; MPIO: blue). **(B)** R_1 ($1/T_1$) values of agarose samples, containing agarose (i.e., no cells), untreated control cells or cells incubated with IgG-MPIO or αPECAM-1-MPIO (all samples: n = 2; bars represent mean ± SD). **(C)** R_2 ($1/T_2$) values of agarose samples, containing agarose (i.e., no cells), untreated control cells or cells incubated with IgG-MPIO or αPECAM-1-MPIO (all samples: n = 2; * P < 0.05 compared to agarose, control cells and IgG-MPIO; bars represent mean ± SD).

3.4.3 αPECAM-1-NIRF specifically targets post-stroke vasculature *in vivo* The *in vivo* suitability of αPECAM-1 to detect vascular remodelling was explored by intravenous (i.v.) injection of near-infrared fluorescent (NIRF) dye-labeled αPECAM-1 or IgG at 3 days post-stroke (αPECAM-1-NIRF: n = 3; IgG-NIRF: n = 3; control: n = 2). Mice received 750 µg antibody/kg body weight, and were euthanized at 70 min post-injection. Analysis of brain tissue sections indicated high binding of αPECAM-1-NIRF to brain vasculature, in contrast to IgG-NIRF, which was not detected in the tissue **(Figure 3.3)**. This indicates that the αPECAM-1 used in this study was able to reach and effectively bind to PECAM-1 on brain endothelium.

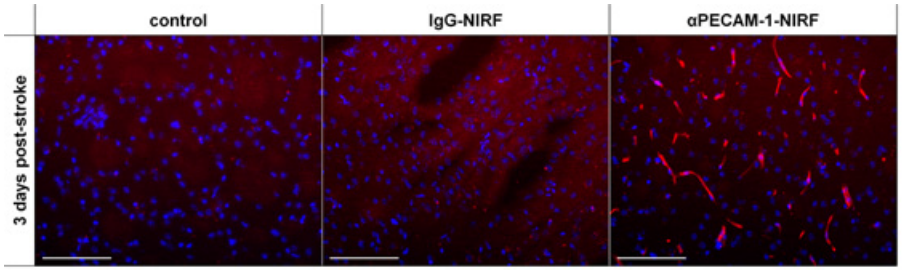

Figure 3.3
αPECAM-1-NIRF specifically targets post-stroke vasculature *in vivo*. Fluorescence microscopy images (20x; scale bars represent 100 µm) of *post mortem* ipsilesional cortical brain tissue of control mice, or mice after *in vivo* injection of IgG-NIRF or αPECAM-1-NIRF at 3 days post-stroke (IgG-NIRF/αPECAM-1-NIRF: red; nuclear staining (DAPI): blue).

3.4.4 Ineffective *in vivo* molecular MRI of post-stroke PECAM-1 expression with αPECAM-1-MPIO αPECAM-1-MPIO were subsequently explored for their applicability as a target-specific contrast agent for *in vivo* molecular MRI of PECAM-1 upregulation at 3 and 7 days after stroke onset. **Figure 3.4A** shows typical examples of post-stroke T_2 maps of mouse brain with an overlay of the contralesional (blue), lesion borderzone (green) and lesion core (red) ROIs, and pre- and post-contrast agent injection T_2*-weighted MR images with overlay of contrast-enhanced voxels. At 3 days post-stroke the lesion core on T_2 maps was identified as a hyperintense area in the right hemisphere, at 7 days post-stroke, lesioned tissue was characterized by heterogeneous signal irregularity in the right hemisphere. Administration of either IgG-MPIO (day 3: n = 6; day 7: n = 4) or αPECAM-1-MPIO (day 3: n = 5; day 7: n = 4) did not result in significant contrast enhancement on the post-contrast agent MR images at day 3 or 7 post-stroke **(Figure 3.4A, last column)**.

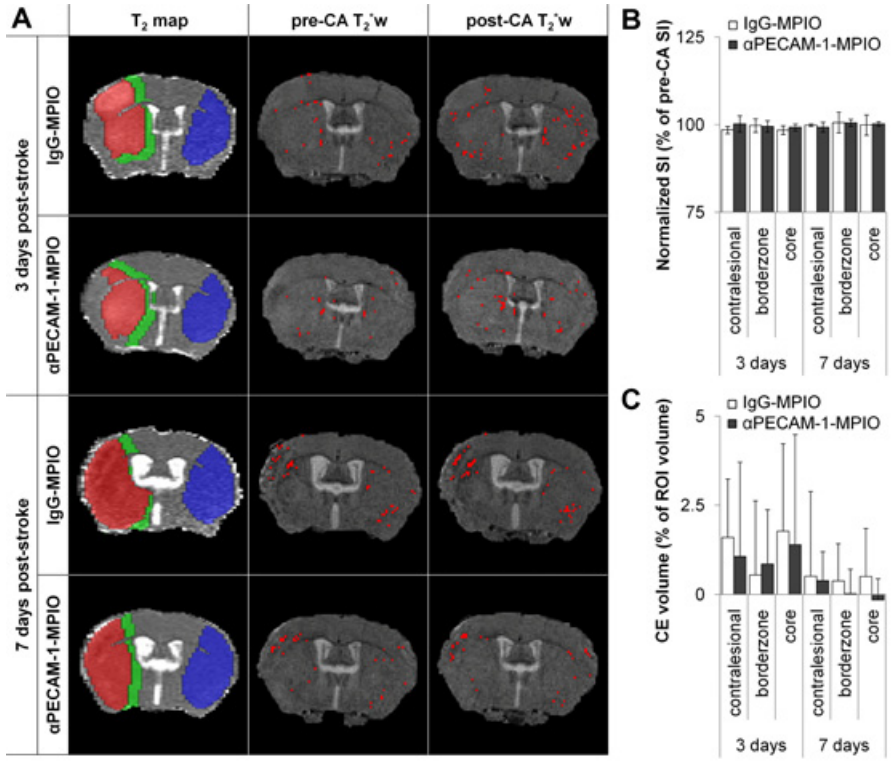

Figure 3.4
In vivo molecular MRI of PECAM-1 expression is not achieved with αPECAM-1-MPIO at 3 or 7 days after transient MCAo in mice. **(A)** Representative pre-contrast agent (CA) T_2 map overlaid with contralesional (blue), lesion borderzone (green) and lesion core (red) ROIs; pre-CA T_2*-weighted image; and post-CA T_2*-weighted image of a coronal brain slice of animals that received IgG-MPIO or αPECAM-1-MPIO at 3 days (top two rows) or 7 days (bottom two rows) post-stroke. Overlaid are contrast-enhanced (CE) voxels, which are depicted in red. **(B)** and **(C)** Bar graphs showing normalized T_2*-weighted signal intensity (SI) **(B)** and difference in contrast-enhanced (CE) volume **(C)** in contralesional, lesion borderzone and lesion core ROIs after injection of CA (IgG-MPIO (day 3: n = 6; day 7: n = 4) or αPECAM-1-MPIO (day 3: n = 5; day 7: n = 4) at 3 and 7 days post-stroke. Bars represent mean ± SD.

This was confirmed by ROI-based image analysis, which revealed that relative mean T_2*-weighted signal intensities in the lesion core (day 3: 100.9 ± 3.5 %; day 7: 102.6 ± 2.6 %) or lesion borderzone (day 3: 100.8 ± 3.9 %; day 7: 102.6 ± 3.4 %) of αPECAM-1-MPIO injected mice were not significantly different from mean signal intensities in the contralesional ROI (day 3: 100.8 ± 4.0 %; day 7: 101.7 ± 2.5 %) or mean signal intensities in the lesion core (day 3: 100.8 ± 4.1 %; day 7: 102.1 ± 1.4 %) or lesion borderzone (day 3: 99.3 ± 3.1 %; day 7: 101.8 ± 1.8 %) of IgG-MPIO injected mice **(Figure 3.4B)**.

The volume percentage of contrast-enhanced voxels in the lesion core and lesion border-zone ROIs also did not change significantly after injection of αPECAM-1-MPIO (lesion core, day 3: 1.4 ± 3.1 %; lesion core, day 7: -0.2 ± 0.6 %; lesion borderzone, day 3: 0.7 ± 1.7 %; lesion borderzone, day 7: -0.1 ± 0.5 %) compared to IgG-MPIO (lesion core, day 3: 1.8 ± 2.4 %; lesion core, day 7: 0.5 ± 1.3 %; lesion borderzone, day 3: 0.5 ± 1.9 %; lesion borderzone, day 7: 0.4 ± 1.1 %), or compared to the αPECAM-1-MPIO-enhanced volume percentage change in the contralesional ROI (day 3: 1.1 ± 2.6 %; day 7: 0.4 ± 0.8 %) (**Figure 3.4C**).

3.4.5 αPECAM-1-MPIO does not specifically target post-stroke vasculature *in vivo*

To determine whether the lack of *in vivo* MRI contrast-enhancement with αPECAM-1-MPIO was due to insufficient contrast agent accumulation in post-stroke brain tissue, mice were terminated after the MRI scan (day 3: n = 5 per group; day 7: n = 4 per group) and brain sections were analyzed by immunohistochemistry. Light microscopy images of PECAM-1-stained and Perls'-stained cortical brain tissue of mice that had received IgG-MPIO or αPECAM-1-MPIO did not reveal any MPIO in the affected hemisphere at days 3 and 7 post-stroke (**Figure 3.5**).

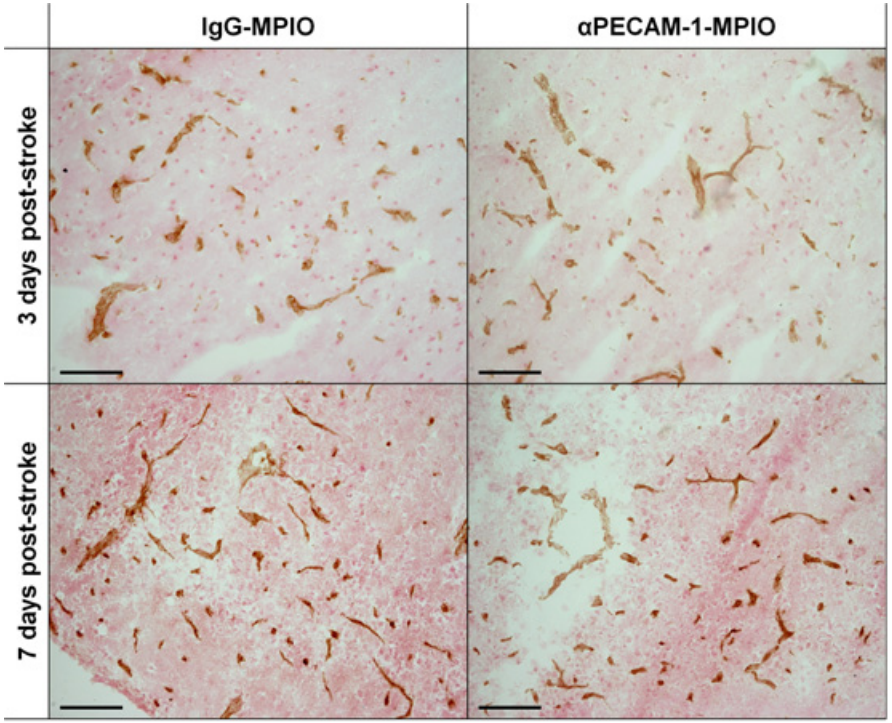

Figure 3.5 *

*** Figure 3.5**

αPECAM-1-MPIO does not specifically target post-stroke vasculature in vivo. Light microscopy images (20x; scale bars represent 100 µm) of *post mortem* cortical brain tissue of the lesion core of mice that received IgG-MPIO (left panel) or αPECAM-1-MPIO (right panel) at 3 (top panel) or 7 days (bottom panel) after MCAo (MPIO: blue; PECAM-1-postitive vessels: brown; nuclei: pink).

3.5 DISCUSSION

PECAM-1 has been frequently applied as an endothelial marker in tissues, including assessments of changes in vascularization after experimental stroke [22, 27-29]. Augmented PECAM-1 immunoreactivity in and around ischemic lesions, reflective of higher blood vessel density, has been found particularly between 2 and 14 days after stroke in different rodent models [21-22, 28]. Furthermore, PECAM-1 expression in post-stroke brain tissue has been shown to increase in response to angiogenesis-stimulating exercise [22], and to decrease after administration of an angiogenesis inhibitor [27]. Our findings of significantly increased ipsilesional PECAM-1 expression between 3 and 21 days, preceded by acutely elevated mRNA levels, after transient unilateral MCA occlusion in mice, are in line with previous studies and provide additional evidence of dynamic vascular modifications in post-stroke tissue. Furthermore, our data corroborate the potential of PECAM-1 as a target for molecular MRI of angiogenesis after stroke.

Molecular MRI of angiogenesis has been successfully performed in animal models of different pathologies, including cancer [30-31], atherosclerosis [32] and myocardial infarction [33-34]. These studies have applied different types of MRI contrast agents, for example based on gadolinium [30, 32-33], iron oxides [31], or perfluorocarbons [35], with conjugated targeting ligands ranging from small peptides to big antibodies. To our knowledge, there have been no reports of molecular MRI of angiogenesis after stroke. Nevertheless, the feasibility of molecular imaging of post-stroke angiogenesis has been demonstrated in a rat model using positron emission tomography (PET) with a radio-labeled vascular endothelial growth factor (VEGF) construct [36]. In the current study, we performed molecular MRI of PECAM-1 expression at 3 and 7 days after experimental stroke, when upregulation of this endothelial marker is markedly increased. Although αPECAM-1-MPIO showed to be an effective target-specific contrast agent in brain endothelial cell culture, we did not detect significant contrast enhancement in post-stroke brain when applied *in vivo*. Lack of *in vivo* contrast agent binding was confirmed by *post mortem* analysis of brain tissue, which revealed absence of contrast agent in PECAM-1-positive vessels. Our findings are in contrast with si-

milar molecular MRI studies in which MPIO was labeled with antibodies against other types of cell adhesion molecules, such as vascular cell adhesion molecule-1 (VCAM-1) [37] and intercellular adhesion molecule-1 (ICAM-1) [38]. Those studies showed specific binding to endothelium after experimental stroke in mice, which generated significant contrast enhancement on *in vivo* MR images with the same MPIO dosage, i.e., ~ 5 mg/kg bodyweight, and ~ 40 µg antibody per $1{\cdot}10^9$ MPIO [37-38], as used in our present study.

The absence of PECAM-1-targeted contrast agent in our present study cannot be explained by inefficiency of the targeting antibody, since a similar amount of the same antibody attached to a NIRF label, i.e., αPECAM-1-NIRF, effectively labeled brain endothelial cells *in vivo* at 3 days post-stroke. This indicates that the binding of single αPECAM-1 IgG molecules with a small NIRF label (less than a nm) is sufficient to recognize its endothelial target PECAM-1 after injection in the blood circulation, and maintains attachment under flow conditions. However, effective binding might not be accomplished when αPECAM-1 is conjugated to larger particles like MPIO (1.05 µm in size), which may reduce target accessibility and increase susceptibility to shear force from circulating blood. Large MPIO may sterically hinder the binding of αPECAM-1 to its epitope PECAM-1, which is mainly expressed in the endothelial cell intercellular junctions [39]. Furthermore, the relatively short blood half-life of the targeted MPIO (in the order of minutes [40-41]) - which is important for wash-out of free circulating contrast agent - may have been too short for efficient binding. Even though binding strength was maximized by multivalent presentation of αPECAM-1 on a single MPIO (~ 100.000 αPECAM-1 per MPIO), this may have decreased the amount of particles available for direct endothelial binding, also when considering possible occupation by PECAM-1-expressing platelets and leukocytes. The number of iron oxide particles available for binding may be increased by reducing the amount of multivalent presentation, e.g., by using smaller particles of iron oxide, such as ultrasmall superparamagnetic particles of iron oxide (USPIO; < 50 nm) or superparamagnetic iron oxide particles (SPIO; 50-200 nm), even though these induce a weaker contrast-generating effect per particle. In addition, further improvement of binding efficiency may be accomplished by co-labeling with a different type of αPECAM-1 targeted to another epitope on PECAM-1, a strategy that has recently been proven to successfully optimize endothelial targeting [42].

3.6 CONCLUSIONS

To summarize, our data demonstrate that PECAM-1, an endothelial marker that can be used for assessment of post-stroke vascular remodeling, can be effectively targeted with αPECAM-1-MPIO *in vitro*, giving rise to significant MRI contrast enhancement. Nevertheless, application of this targeted contrast agent was ineffective for *in vivo* molecular MRI of angiogenesis at 3 or 7 days after experimental stroke in mice, which may be explained by inefficient binding of the large multivalent ligand-presenting construct under *in vivo* conditions.

3.7 REFERENCES

1. Hacke W, Kaste M, Bluhmki E, Brozman M, Davalos A, Guidetti D, Larrue V, Lees KR, Medeghri Z, Machnig T, Schneider D, von Kummer R, Wahlgren N, Toni D (2008) Thrombolysis with alteplase 3 to 4.5 hours after acute ischemic stroke. N Engl J Med 359:1317-1329.
2. Cramer SC (2008) Repairing the human brain after stroke. II. Restorative therapies. Ann Neurol 63:549-560.
3. Zhang ZG, Chopp M (2009) Neurorestorative therapies for stroke: underlying mechanisms and translation to the clinic. Lancet Neurol 8:491-500.
4. Cramer SC (2008) Repairing the human brain after stroke: I. Mechanisms of spontaneous recovery. Ann Neurol 63:272-287.
5. Xiong Y, Mahmood A, Chopp M (2010) Angiogenesis, neurogenesis and brain recovery of function following injury. Curr Opin Investig Drugs 11:298-308.
6. Arai K, Jin G, Navaratna D, Lo EH (2009) Brain angiogenesis in developmental and pathological processes: neurovascular injury and angiogenic recovery after stroke. FEBS J 276:4644-4652.
7. Beck H, Plate KH (2009) Angiogenesis after cerebral ischemia. Acta Neuropathol 117:481-496.
8. Yanev P, Dijkhuizen RM (2012) *In vivo* imaging of neurovascular remodeling after stroke. Stroke 43:3436-3441.
9. Hayashi T, Deguchi K, Nagotani S, Zhang H, Sehara Y, Tsuchiya A, Abe K (2006) Cerebral ischemia and angio genesis. Curr Neurovasc Res 3:119-129.

10. Krupinski J, Kaluza J, Kumar P, Kumar S, Wang JM (1994) Role of angiogenesis in patients with cerebral ischemic stroke. Stroke 25:1794-1798.
11. Slevin M, Kumar P, Gaffney J, Kumar S, Krupinski J (2006) Can angiogenesis be exploited to improve stroke outcome? Mechanisms and therapeutic potential. Clin Sci (Lond) 111:171-183.
12. Liman TG, Endres M (2012) New vessels after stroke: postischemic neovascularization and regeneration. Cerebrovasc Dis 33:492-499.
13. Baird AE, Warach S (1998) Magnetic resonance imaging of acute stroke. J Cereb Blood Flow Metab 18:583-609.
14. Dijkhuizen RM, Nicolay K (2003) Magnetic resonance imaging in experimental models of brain disorders. J Cereb Blood Flow Metab 23:1383-1402.
15. Farr TD, Wegener S (2010) Use of magnetic resonance imaging to predict outcome after stroke: a review of experimental and clinical evidence. J Cereb Blood Flow Metab 30:703-717.
16. Barbier EL, Lamalle L, Decorps M (2001) Methodology of brain perfusion imaging. J Magn Reson Imaging 13:496-520.
17. Seevinck PR, Deddens LH, Dijkhuizen RM (2010) Magnetic resonance imaging of brain angiogenesis after stroke. Angiogenesis 13:101-111.
18. Calamante F, Thomas DL, Pell GS, Wiersma J, Turner R (1999) Measuring cerebral blood flow using magnetic resonance imaging techniques. J Cereb Blood Flow Metab 19:701-735.
19. Wu EX, Tang H, Jensen JH (2004) Applications of ultrasmall superparamagnetic iron oxide contrast agents in the MR study of animal models. NMR Biomed 17:478-483.
20. Deddens LH, Van Tilborg GA, Mulder WJ, De Vries HE, Dijkhuizen RM (2012) Imaging neuroinflammation after stroke: current status of cellular and molecular MRI strategies. Cerebrovasc Dis 33:392-402.
21. Marti HJ, Bernaudin M, Bellail A, Schoch H, Euler M, Petit E, Risau W (2000) Hypoxia-induced vascular endothelial growth factor expression precedes neovascularization after cerebral ischemia. Am J Pathol 156:965-976.
22. Matsuda F, Sakakima H, Yoshida Y (2011) The effects of early exercise on brain damage and recovery after focal cerebral infarction in rats. Acta Physiol (Oxf) 201:275-287.
23. Wagner EF, Risau W (1994) Oncogenes in the study of endothelial cell growth and differentiation. Semin Cancer Biol 5:137-145.
24. Perls M (1867) Nachweis von Eisenoxyd in gewissen Pigmenten. Virchows Archiv 39:42-48.
25. Schroeter M, Saleh A, Wiedermann D, Hoehn M, Jander S (2004) Histochemical detection of ultrasmall superparamagnetic iron oxide (USPIO) contrast medium uptake in experimental brain ischemia. Magn Reson Med 52:403-406.
26. Hata R, Mies G, Wiessner C, Fritze K, Hesselbarth D, Brinker G, Hossmann KA (1998) A reproducible model of middle cerebral artery occlusion in mice: hemodynamic, biochemical, and magnetic resonance imaging. J Cereb Blood Flow Metab 18:367-375.
27. Ohab JJ, Fleming S, Blesch A, Carmichael ST (2006) A neurovascular niche for neurogenesis after stroke. J Neurosci 26:13007-13016.
28. Mora-Lee S, Sirerol-Piquer MS, Gutierrez-Perez M, Lopez T, Casado-Nieto M, Jauquicoam C, Abizanda G, Romaguera-Ros M, Gomez-Pinedo U, Prosper F, Garcia-Verdugo JM (2011) Histological and ultra structural comparison of cauterization and thrombosis stroke models in immune-deficient mice. J Inflamm (Lond) 8:28.
29. Gertz K, Kronenberg G, Kalin RE, Baldinger T, Werner C, Balkaya M, Eom GD, Hellmann-Regen J, Krober J, Miller KR, Lindauer U, Laufs U, Dirnagl U, Heppner FL, Endres M (2012) Essential role of interleukin-6 in post-stroke angiogenesis. Brain 135:1964-1980.
30. Mulder WJ, Strijkers GJ, Habets JW, Bleeker EJ, Van der Schaft DW, Storm G, Koning GA, Griffioen AW, Nicolay K (2005) MR molecular imaging and fluorescence microscopy for identification of activated tumor endothelium using a bimodal lipidic nanoparticle. FASEB J 19:2008-2010.
31. Jarzyna PA, Deddens LH, Kann BH, Ramachandran S, Calcagno C, Chen W, Gianella A, Dijkhuizen RM, Griffioen AW, Fayad ZA, Mulder WJ (2012) Tumor angiogenesis phenotyping by nanoparticle-facilitated magnetic resonance and near-infrared fluorescence molecular imaging Neoplasia 14:964-973.
32. Cai K, Caruthers SD, Huang W, Williams TA, Zhang H, Wickline SA, Lanza GM, Winter PM (2010) MR molecular imaging of aortic angiogenesis. JACC Cardiovasc Imaging 3:824-832.

33. Oostendorp M, Douma K, Wagenaar A, Slenter JM, Hackeng TM, van Zandvoort MA, Post MJ, Backes WH (2010) Molecular magnetic resonance imaging of myocardial angiogenesis after acute myocardial infarction. Circulation 121:775-783.

34. Xiao L, Zhang Y, Yang Z, Xu Y, Kundu B, Chordia MD, Pan D (2012) Syn thesis of PECAM-1-specific 64Cu PET imaging agent: evaluation of myocardial infarction caused by ischemia-reperfusion injury in mouse. Bioorg Med Chem Lett 22:4144-4147.

35. Caruthers SD, Winter PM, Wickline SA, Lanza GM, Keupp J (2010) MR molecular imaging of angiogenesis using targeted perfluorocarbon nanoparticles. Medicamundi 54:5-13.

36. Cai W, Guzman R, Hsu AR, Wang H, Chen K, Sun G, Gera A, Choi R, Bliss T, He L, Li ZB, Maag AL, Hori N, Zhao H, Moseley M, Steinberg GK, Chen X (2009) Positron emission tomography imaging of poststroke angiogenesis. Stroke 40:270-277.

37. Hoyte LC, Brooks KJ, Nagel S, Akhtar A, Chen R, Mardiguian S, McAteer MA, Anthony DC, Choudhury RP, Buchan AM, Sibson NR (2010) Molecular magnetic resonance imaging of acute vascular cell adhesion molecule-1 expression in a mouse model of cerebral ischemia. J Cereb Blood Flow Metab 30:1178-1187.

38. Deddens LH, Van Tilborg GA, Van der Toorn A, Paulis LE, Strijkers GJ, Storm G, Mulder WJ, De Vries HE, Dijkhuizen RM (2012) Micron-sized particles of iron oxide and gadolinium-containing liposomes as targeted contrast agent for mole cular MRI of neuroinflammation after stroke: A comparative study. Proceedings International Society for Magnetic Resonance in Medicine 20: 1627P.

39. Newman PJ (1997) The biology of PECAM-1. J Clin Invest 100:S25-29.

40. Yang Y, Yanasak N, Schumacher A, Hu TC (2010) Temporal and noninvasive monitoring of inflammatory-cell infiltration to myocardial infarction sites using micrometer-sized iron oxide particles. Magn Reson Med 63:33-40.

41. Ye Q, Wu YL, Foley LM, Hitchens TK, Eytan DF, Shirwan H, Ho C (2008) Longitudinal tracking of recipient macrophages in a rat chronic cardiac allograft rejection model with noninvasive magnetic resonance imaging using micrometer-sized paramagnetic iron oxide particles. Circulation 118:149-156.

42. Chacko AM, Nayak M, Greineder CF, Delisser HM, Muzykantov VR (2012) Collaborative enhancement of antibody binding to distinct PECAM-1 epitopes modulates endothelial targeting. PLoS One 7:e34958.

MOLECULAR MRI OF ICAM-1 UPREGULATION AFTER STROKE: CHOOSING THE APPROPRIATE CONTRAST AGENT

Based on:
Lisette H. Deddens, Geralda A.F. van Tilborg, Annette van der Toorn, Kajo van der Marel, Leonie E.M. Paulis, Louis van Bloois, Gert Storm, Gustav J. Strijkers, Willem J.M. Mulder, Helga E. de Vries and Rick M. Dijkhuizen.
MRI of ICAM-1 upregulation after stroke: The importance of choosing the appropriate target-specific particulate contrast agent
Mol Imaging Biol **2013** (in press)

04

4.1 ABSTRACT

MRI with targeted contrast agents provides a promising means for diagnosis and treatment monitoring after cerebrovascular injury. Our goal was to demonstrate the feasibility of this approach to detect the neuroinflammatory biomarker intercellular adhesion molecule-1 (ICAM-1) after stroke, and to establish a most efficient imaging procedure. We compared two types of ICAM-1-functionalized contrast agent: T_1-shortening gadoliniumchelate-containing liposomes, and $T_2^{(*)}$-shortening micron-sized iron oxide particles (MPIO). Binding efficacy and MRI contrast effects were tested in cell cultures and a mouse stroke model. Both ICAM-1-targeted agents bound effectively to activated cerebrovascular cells *in vitro*, generating significant MRI contrast-enhancing effects. Direct *in vivo* MRI-based detection after stroke was only achieved with ICAM-1-targeted MPIO, although both contrast agents showed similar target-specific vascular accumulation. Our study demonstrates the potential of *in vivo* MRI of post-stroke ICAM-1 upregulation, and signifies target-specific MPIO as most suitable contrast agent for molecular MRI of cerebrovascular inflammation.

4.2 INTRODUCTION

Cerebrovascular disorders, such as stroke, are leading causes of death and disability in modern society. One of the key players in cerebrovascular injury is the neuroinflammatory cascade, which among others involves endothelial cell activation and leukocyte infiltration [1]. Despite increasing number of studies on neuroinflammatory processes, underlying mechanisms have been incompletely elucidated. Imaging strategies that enable *in vivo* detection of inflammatory markers can significantly contribute to improved characterization of neuroinflammatory events in cerebrovascular disorders, and may serve as valuable means for early disease diagnosis and direct monitoring of the efficacy of anti-inflammatory treatments [2-3].

Magnetic resonance imaging (MRI) is an established versatile method for non-invasive imaging of brain pathologies in clinical and experimental settings [4-5]. Using MR contrast agents, such as gadolinium (Gd)-chelates, complementary information can be obtained on, for instance, perfusion disturbances and blood-brain barrier disruption. MR contrast agents may also be functionalized with target-specific ligands, e.g., peptides, proteins and antibodies, for imaging of molecular biomarkers, such as inflammatory constituents [6]. Two main types of contrast agents for (molecular) MRI can be distinguished: paramagnetic Gd-chelates, which shorten longitudinal relaxation time T_1 and thereby induce local hyperintensity on T_1-weighted images, and superparamagnetic iron oxide particles that shorten the transverse relaxation time, $T_2^{(*)}$, resulting in local hypointensities on $T_2^{(*)}$-weighted images [7]. These contrast agents can be presented in a variety of platforms, ranging from nanometer-sized single Gd-chelates (Gd-diethylenetriaminepentaacetic acid; Gd-DTPA) and tens-of-nanometer-sized ultrasmall particles of iron oxide (USPIO), to larger structures containing high numbers of Gd-chelates or iron oxides per particle, such as Gd-dendrimers [8] and Gd-liposomes [9] and micron-sized particles of iron oxide (MPIO) [10].

Molecular MRI of inflammation in brain disorders, using tailored contrast agents targeted to neuroinflammatory markers, is an emerging field of research [6]. Previous studies in animal stroke models have targeted the cell adhesion molecules P- or E-selectin [11-13], vascular cell adhesion molecule-1 (VCAM-1) [14], or the heme protein myeloperoxidase (MPO), which is secreted by activated neutrophils and macrophages/microglia [15]. However, to date, no study has imaged stroke-induced upregulation of intercellular adhesion molecule-1 (ICAM-1) expression *in vivo*. ICAM-1 is highly upregulated on inflamed cerebral endothelium during the first days post-stroke in rodents [16] and humans [17], and provides an interesting alternative target for molecular MR imaging of neuroinflammation, being maximally expressed at later time points than other cell adhesion molecules, such as selectins [18] and VCAM-1 [19]. Importantly, an efficient strategy to target cerebrovascular ICAM-1 may expand the potential of molecular imaging in (pre)clinical settings, by extending the time window for *in vivo* detection of neuroinflammation up to sub-acute phases, thereby improving the possibilities for monitoring of anti-inflammatory treatments, implicating clinical potential for long-term monitoring of treatment efficacy.

In previous studies, both target-specific Gd-chelates [11] and iron oxides [12-15] have been successfully applied for *in vivo* molecular MRI of stroke-induced neuroinflammation, but it remains unknown to what extent these agents provide adequate sensitivity and specificity, considering dynamic endogenous tissue contrast changes during disease progression, such as T_1 and $T_2^{(*)}$ prolongation. To this end, we directly compared the application of ICAM-1-targeted Gd-based versus iron oxide-based contrast agents, using Gd-liposomes and MPIO as most potent representatives for the different contrast agent types. These particles can target intraluminally expressed ICAM-1 after intravascular injection, and enable amplified image contrast by their high payload of contrast agent per particle, while preventing possible leakage over a disrupted blood-brain barrier by their substantial size (~ 200 nm and ~ 1 µm,

respectively). With this comparison, we aimed to establish a most efficient method for straightforward, sensitive and specific *in vivo* detection of the neuroinflammatory marker ICAM-1 after cerebrovascular injury with molecular MRI.

4.3 MATERIALS AND METHODS

4.3.1 Materials Gd-DTPA-di(stearylamide) (Gd-DTPA-DSA) was obtained from Gateway Chemical Technology (St. Louis, MO, USA). 1,2-distearoyl-sn-glycero-3-phosphocholine (DSPC), 1,2-distearoyl-sn-glycero-3-phosphoethanolamine-N-[methoxy(polyethylene glycol)2000] (PEG2000-DSPE), 1,2-distearoyl-sn-glycero-3-phosphoethanolamine-N-[maleimide(polyethylene glycol)2000] (Mal-PEG2000-DSPE) and 1,2-dipalmitoyl-sn-glycero-3-phosphoethanolamine-N-(lissamine rhodamine B sulfonyl) (rhodamine-PE) were obtained from Avanti Polar Lipids (Albaster, AL, USA). ProMag™ 1 Series, Bind-IT™ MPIO (25 mg MPIO/ml, 26.5 % iron-content) were obtained from Bangs Laboratories, Inc. (Fishers, IN, USA). Cholesterol and diaminobenzidine solution (DAB+) were obtained from Sigma-Aldrich (St. Louis, MO, USA). A monoclonal antibody against mouse ICAM-1 (αICAM-1, YN1/1.7.4) and irrelevant immunoglobulin G antibody (IgG, RTK4530) were obtained from BioLegend (San Diego, CA, USA). Horseradish peroxidase-labeled streptavidin (HRPstrep) was obtained from DAKO (Glostrup, Denmark). A monoclonal antibody against mouse CD31 (αCD31) was produced from hybridoma ER-MP12. Primers were obtained from Ocimum Biosolutions, IJsselstein, The Netherlands.

4.3.2 Preparation of antibody-functionalized Gd-liposomes Gd-liposomes were prepared by lipid film hydration. Gd-DTPA-DSA, DSPC, cholesterol, PEG2000-DSPE, Mal-PEG2000-DSPE and rhodamine-PE were mixed at a molar ratio of 0.75/1.10/1/0.075/0.075/0.003, dissolved in chloroform/methanol 10:1 (v/v) and evaporated to dryness at 40 ˚C. The lipid film was hydrated in HEPES-buffered saline (10 mM 4-(2-hydroxyethyl)-1-piperazineethanesulfonic acid (HEPES), 135 mM NaCl; pH 6.5). The resulting lipid dispersion was extruded at 60 ˚C, once through a single polycarbonate membrane filter with a pore diameter of 200 nm, and sequentially 10 times through a double filter of 200 nm using a Lipofast Extruder (Avestin Inc., Ottawa, Ontario, Canada).

αICAM-1or isotype control IgG was coupled to Gd-liposomes by a sulfhydryl-maleimide linking method as described previously [20-21]. In short, αICAM-1 and IgG (1 mg/ml) were modified with N-succinimidyl S-acetylthioacetate (SATA, 80:1 SATA:antibody in molar ratio) and incubated for 1 h on a roller-bench at room temperature. Free SATA was removed from SATA-derivatized antibody by washing 3 times with HEPES-buffered saline using a Vivaspin concentrator with a cut-off size of 50 kD (GE Healthcare Europe GmbH, Diegem, Belgium) and centrifugation at 4000g. SATA-derivatized antibody was deacetylated by incubation with a hydroxylamine solution (pH 6.7) for 1 h at room temperature. Activated antibody was added to the maleimide-containing Gd-liposomes in a 50 µg protein/µmol lipid ratio. This preparation was stored at 4 ˚C under gaseous N_2 overnight. Uncoupled antibodies were separated from immunoliposomes by centrifugation at 65000 rpm for 2 times 45 min at 4 ˚C. The phospholipid content of the obtained liposome preparations was determined by phosphate analysis according to Rouser et al [22] after destruction with perchloric acid. Subsequently, the sample was further diluted to obtain a lipid suspension of 20 mM total lipid. The final liposomal suspension was stored at 4 ˚C under gaseous N_2 and used within 7 days.

The size distribution of the αICAM-1 or IgG-Gd-liposomes was displayed as z-average ± polydispersity index (PDI), determined by dynamic light scattering (DLS) at 25 ˚C with a Malvern 4700 system using an argon-ion laser (488 nm) operating at 10.4 mW (Uniphase) and using PCS (photon correlation spectrometry) software for Windows version 1.34 (Malvern Instruments Ltd, Worcestershire, UK). For data analysis, the viscosity and refractive index of water was used. The system was calibrated with a polystyrene dispersion containing particles of 100 nm.

4.3.3 Preparation of antibody-functionalized MPIO MPIO were extracted from their original buffer by magnetic separation and resuspended in coupling buffer (50 mM 2-(N-morpholino)ethanesulfonic acid (MES); pH 5.2). Prior to the coupling procedure, αICAM-1 or IgG were buffer exchanged to coupling buffer by centrifugation, resulting in a final antibody concentration of 1.0 mg/ml. Next, MPIO and αICAM-1 or IgG were added in a 1:1 (v/v) ratio, vortexed and left to incubate for 60 min at room temperature on a roller-bench. Following incubation, antibody-MPIO were buffer-exchanged to storage solution (150 mM NaCl, 0.002 % azide) by magnetic separation and stored at 4 ˚C.

4.3.4 MR relaxivity measurements Relaxivities were acquired on a 9.4 T horizontal 20 cm bore MR system (Varian Inc., Palo Alto, CA, USA) at room temperature using a dilution series of Gd-liposomes (ranging from 0 to 2.5 mM Gd-DTPA-DSA, calculated from the lipid ratio and total lipid concentration) or MPIO (ranging from 0 to 0.05 mg iron/ml, calculated from the iron-content provided by the manufacturer). T_1 values were acquired using a Look-Locker inversion recovery sequence (after each inversion pulse

40 acquisitions were done with intervals of 250 ms, repetition time (TR) 20 s, echo time (TE) 3.18 ms, flip angle (FA) 5°, number of averages (NA) 4, matrix size 256 x 256, field-of-view (FOV) 3 x 3 cm^2, slice thickness 400 µm). T_2 values were acquired with a multi-spin echo sequence (TR 5 s, TE 9-900 ms, number of echoes (NE) 100, NA 4, matrix size 256 x 256, FOV 3 x 3 cm^2, slice thickness 400 µm). Relaxivities, r_1 and r_2, expressed in $mM^{-1} \cdot s^{-1}$, were measured from the slope from a linear fit of $1/T_1$ (R_1) and $1/T_2$ (R_2) values versus the concentration of Gd or iron.

4.3.5 *In vitro* cell experiments The mouse brain endothelioma cell line bEnd.5 [23] was maintained in Dulbecco's Modified Eagle Medium (DMEM; Invitrogen, Grand Island, NY, USA) supplemented with 10 % heat-inactivated fetal calf serum (FCS; PAA Laboratories GmbH, Pasching, Austria), 100 U/ml penicillin, 100 µg/ml streptomycin (all obtained from Gibco, Carlsbad, CA, USA) and 5 µM of b-mercaptoethanol. Cells were cultured in non-coated flasks at normal cell culture conditions.

For endothelial activation, bEnd.5 cells at 70-80 % confluence were stimulated with 10 ng/ml tumor necrosis factor alpha (TNFα; PeptroTech EC Ltd., London, UK). After 24 h, cells were either incubated with αICAM-1-Gd-liposomes or IgG-Gd-liposomes (1 µmol total lipid/ml medium; 4 h at 37 °C) or αICAM-1-MPIO and IgG-MPIO (10 µg iron/ml medium; 1 h at 37 °C) (n = 2 per condition). Alternatively, control cells were left untreated (n = 2 per condition). Following incubation, cells were thoroughly washed and subsequently harvested. The resulting cell suspension was washed twice with phosphate-buffered saline (PBS) by centrifugation (1500 rpm, 5 min). Cells were subsequently fixed in 4 % paraformaldehyde in PBS (10 min), washed with PBS twice, and stored in PBS containing 0.002 % azide. The fixed cells were allowed to settle overnight by gravitational force. The resulting cell pellet was subsequently subjected to T_1 and T_2 measurements using the same MRI protocols as for relaxivity measurements. Additionally, a small amount of fixed bEnd.5 cells incubated with antibody-functionalized contrast agent was used to prepare cytospins for optical visualization of contrast agent binding. Cytospins of cells incubated with Gd-liposomes were mounted in 4',6-diamidino-2-phenylindole (DAPI)-containing mounting medium for detection by fluorescence microscopy. Perls' staining [24-25] was performed on cytospins of cells incubated with MPIO to be detected with light microscopy. Shortly, cytospins were fixed in acetone for 10 min at room temperature, dried and incubated with Perls' solution (2 N HCl and 2 % ferrocyanide in Milli-Q in 1:1 (v/v) ratio) for 20 min. Subsequently, cytospins were thoroughly washed with Milli-Q, dipped in a nuclear fast red solution, dehydrated and mounted in Entallan.

4.3.6 *In vivo* stroke model All animal procedures were approved by the Utrecht University Ethical Committee on Animal Experiments, and experiments were performed in accordance with the guidelines of the European Communities Council Directive.

Eight-week-old C57Bl/6 mice, weighing 20 to 25 g (Harlan, Horst, The Netherlands) were anesthetized with isoflurane (3.5 % induction, 1.5-2.0 % maintenance) in air/O_2 (2:1). Body temperature was maintained at 37.0 ± 0.5 °C. Transient focal cerebral ischemia was induced by 30 min right middle cerebral artery occlusion (MCAo) with an intraluminal filament [26]. In brief, a 7.0 polypropylene suture with a silicon-coated tip (tip diameter of 0.21 mm, Doccol Corporation, Redlands, CA, USA) was introduced into the right external carotid artery and advanced through the internal carotid artery until a slight resistance was felt, indicating that the MCA was occluded. During occlusion, the common carotid artery was clipped. After 30 min, the filament was withdrawn from the internal carotid artery and the clip was removed from the common carotid artery to allow full reperfusion. Before surgery, mice received a 1 ml subcutaneous injection of saline to compensate for loss of water and minerals, and a subcutaneous injection of 0.1 mg/kg buprenorphine (Temgesic; Schering-Plough, Houten, The Netherlands) for post-surgical analgesia.

4.3.7 *Post mortem* ICAM-1 immunohistochemistry and qPCR Mice were sacrificed at 6 h, 24 h, 3 days or 7 days after MCAo (n = 4 per time point) with an overdose of pentobarbital (Euthanimal; Alfasan International BV, Woerden, Holland) followed by transcardial perfusion with PBS. Two healthy animals were used as controls (0 h). Brains were excised and snap-frozen in liquid N_2 and used for *post mortem* immunohistochemistry and quantitative polymerase chain reaction (qPCR).

For immunohistochemistry, cryosections of 10 µm (6 per mouse, ranging from approximately -1 to +1.5 mm from Bregma) were air-dried overnight, and acetone-fixated for 10 min. Dry, fixed sections were hydrated for 15 min in PBS containing 0.1 % bovine serum albumin (BSA). Next, sections were incubated with biotinylated αICAM-1 (10 µg antibody/ml) in PBS/0.1 % BSA for 1 h. Subsequently, sections were incubated for 45 min with horseradish peroxidase-labeled streptavidin (HRPstrep, prepared according to the manufacturer's description). Diaminobenzidine solution (DAB) was used as chromogen (used according to the manufacturer's description). Between incubation steps, sections were thoroughly washed with PBS. Preparations were incubated with hematoxylin for 1 min after which sections were dehydrated and mounted in Entallan. All steps were performed at room temperature.

For qPCR, messenger ribonucleic acid (mRNA) was isolated from brain tissue from subsequent sets as used for immunohistochemistry, using an mRNA capture kit (Roche Applied Science, Indianapolis, IN, USA) according to the manufacturer's instructions. Two samples per mouse were obtained, being ipsilesional and contralesional hemispheric tissue. For this, 6 brain slices of 10 µm (in the range of -1 to +1.5 mm from Bregma) were hemispherically divided and pooled in an ipsilesional and contralesional tissue fraction. Complimentary deoxyribonucleic acid (DNA) was synthesized with the Reverse Transcription System kit (Promega Corporation, Madison, WI, USA) following manufacturer's guidelines. qPCR reactions were performed in an ABI7900HT sequence detection system with the SYBR Green method (Applied Biosystems, Foster City, CA, USA). Obtained expression levels of transcripts of ICAM-1 (primer sequences used were ICAM-1-F 5'-TAGCAGCCGCAGTCATAATGGG-3' and ICAM-1-R 5'-AGGCGTGGCTTGTGTGTTCG-3') were normalized to glyceraldehyde 3-phosphate dehydrogenase (GAPDH) expression levels (GAPDH-F 5'-CCATGTTCGTCATGGGTGTG-3' and GAPDH-R 5'-GGTGCTAAGCAGTTGGTGGTG-3').

4.3.8 *In vivo* molecular MRI Mice were subjected to MCAo (n = 36) and underwent *in vivo* MRI at 24 h after reperfusion under general isoflurane anesthesia (n = 26; 10 animals died the first 24 h after surgery). Multi-spin echo MRI was applied for T_2 mapping (TR/TE = 2300/12-96 ms, NE 8, NA 4, matrix size 192 x 96, FOV 2 x 2 cm^2, 21 slices of 400 µm) to determine lesion size. T_1 maps (Look-Locker inversion recovery; 40 slice-interleaved acquisitions with 10 ms intervals after each inversion pulse, interval time of 210 ms per slice, TR/TE = 9000/4.5 ms, FA 10°, NA 2, matrix size 96 x 64, FOV 2 x 2 cm^2, 21 slices of 400 µm) were acquired before and up to 3 h after intravenous (i.v.) injection of αICAM-1- or IgG-Gd-liposomes (5 µmol total lipid/mouse, n = 7 per contrast agent type). T_2*-weighted images (3D gradient echo; TR/TE = 35/15 ms, NA 8, FA 10°, matrix size 96 x 80 x 160, FOV 1 x 1.2 x 2 cm^3) were acquired before and up to 1 h after i.v. injection of αICAM-1- or IgG-MPIO (100 µg iron/mouse, n = 5 for αICAM-1-MPIO (one animal was excluded due to incomplete injection) and n = 6 for IgG-MPIO). A subgroup of mice were subjected to a follow-up scan at 48 h after stroke, i.e., 24 h after contrast agent injection (n = 6 for both Gd-liposomes group, n = 2 for both MPIO groups). Mice were sacrificed immediately after the last MRI scan by an intraperitoneal (i.p.) injection with pentoparbital followed by transcardial perfusion with PBS. Fresh brains were quickly excised, snap-frozen with liquid N_2 and stored at -80 °C for *post mortem* immunohistochemical validation.

For *post mortem* immunohistochemical validation, cryosections of 10 µm (6 per mouse, ranging from approximately -1 to +1.5 mm from Bregma) were prepared. Subsequently, tissue was co-stained with αCD31 to visualize the cerebrovasculature. For mice that received Gd-liposomes, tissue was dried overnight and acetone-fixated for 10 min at -20 °C. After air-drying, tissue was hydrated in PBS/0.1 % BSA and incubated with αCD31-alexa648 (1:100 in PBS/0.1 % BSA) for 1 h at room temperature. Tissue was subsequently washed and mounted in DAPI-containing mounting medium (1:15000, (v/v)) for fluorescence microscopy. Tissue of mice that received MPIO was stained with Perls' and αCD31. Shortly, tissue was dried overnight and acetone-fixated for 10 min at room temperature. After the acetone was evaporated, tissue was hydrated in PBS/0.1 % BSA and incubated with biotinylated αCD31 (1:100 in PBS/0.1 % BSA) for 1 h, followed by incubation with HRPstrep (prepared according to the manufacturer's description) for 45 min. DAB was used as chromogen (used according to the manufacturer's description). Tissue was subsequently incubated with Perls' solution as described for the *in vitro* cell experiments, thoroughly washed with Milli-Q, dipped in a nuclear fast red solution, dehydrated and slides were mounted in Entallan.

4.3.9 MRI analysis A voxel-based supervised classification method was employed to identify stroke lesions in all animals [27]. First, two experts manually outlined lesions on T_2 maps in ten animals. Based on the consensus between the expert segmentations, a random forest classifier was then trained on T_2 and anatomical location obtained from non-rigid registration to a template image. Given the classification results, homologous contralesional tissue was depicted manually. These lesion segmentations were subsequently used as regions-of-interest (ROIs). Mean T_1 for mice that received Gd-liposomes, and mean signal intensity (SI) of T_2*-weighted images for mice that received MPIO were calculated within these ipsilesional and contralesional ROIs, and expressed relative to pre-contrast values, i.e., [SI post-contrast/SI pre-contrast] · 100 %.

4.3.10 Statistical analysis SPSS 16.0 was used for statistical analyses. Groups were compared with use of a Student's t-test for independent samples, or a univariate ANOVA with a Bonferroni post-hoc test. Values are presented as mean ± standard deviation. $P < 0.05$ was considered statistically significant.

4.4 RESULTS

4.4.1 Gd-liposomes and MPIO are T_1- and $T_2^{(*)}$-type contrast agents, respectively As a visual guide, schematic representations of Gd-liposomes and MPIO are depicted in **Figure 4.1A** and **B**, with their respective relaxivities r_1 and r_2 at 9.4 T. Gd-liposomes displayed a hydrodynamic diameter of 0.21 µm with a polydispersity index of 0.08. MPIO were 1.05 µm in diameter, according to the manufacturer. Gd-liposomes had an r_1 of 1.6 ± 0.1 $mM^{-1}{\cdot}s^{-1}$ and r_2 of 18 ± 2 $mM^{-1}{\cdot}s^{-1}$, representative for T_1-shortening contrast agents. MPIO showed typical $T_2^{(*)}$-shortening contrast agent properties, with relatively small effect on T_1 (r_1 = 0.3 ± 0.0 $mM^{-1}{\cdot}s^{-1}$), but large effect on T_2 (r_2 = 91 ± 3 $mM^{-1}{\cdot}s^{-1}$).

4.4.2 ICAM-1-targeted Gd-liposomes and MPIO bind specifically to stimulated brain endothelial cells The target specificity of ICAM-1-targeted contrast agent was tested on TNFα-stimulated brain endothelial cells, which showed a twofold increase in ICAM-1 expression compared to non-stimulated cells (data not shown). TNFα-stimulated cells were incubated with IgG-Gd-liposomes or αICAM-1-Gd-liposomes (1 µmol total lipid/ml medium; 4 h), or with IgG-MPIO or αICAM-1-MPIO (10 µg iron/ml medium; 1 h). Images from (fluorescence) microscopy showed that cells treated with either IgG-Gd-liposomes or IgG-MPIO displayed minimal amounts of cell-associated contrast agent, whereas cells treated with αICAM-1-Gd-liposomes or αICAM-1-MPIO showed abundant association **(Figure 4.1C and D)**, indicating specific binding of both ICAM-1-targeted contrast agents *in vitro*.

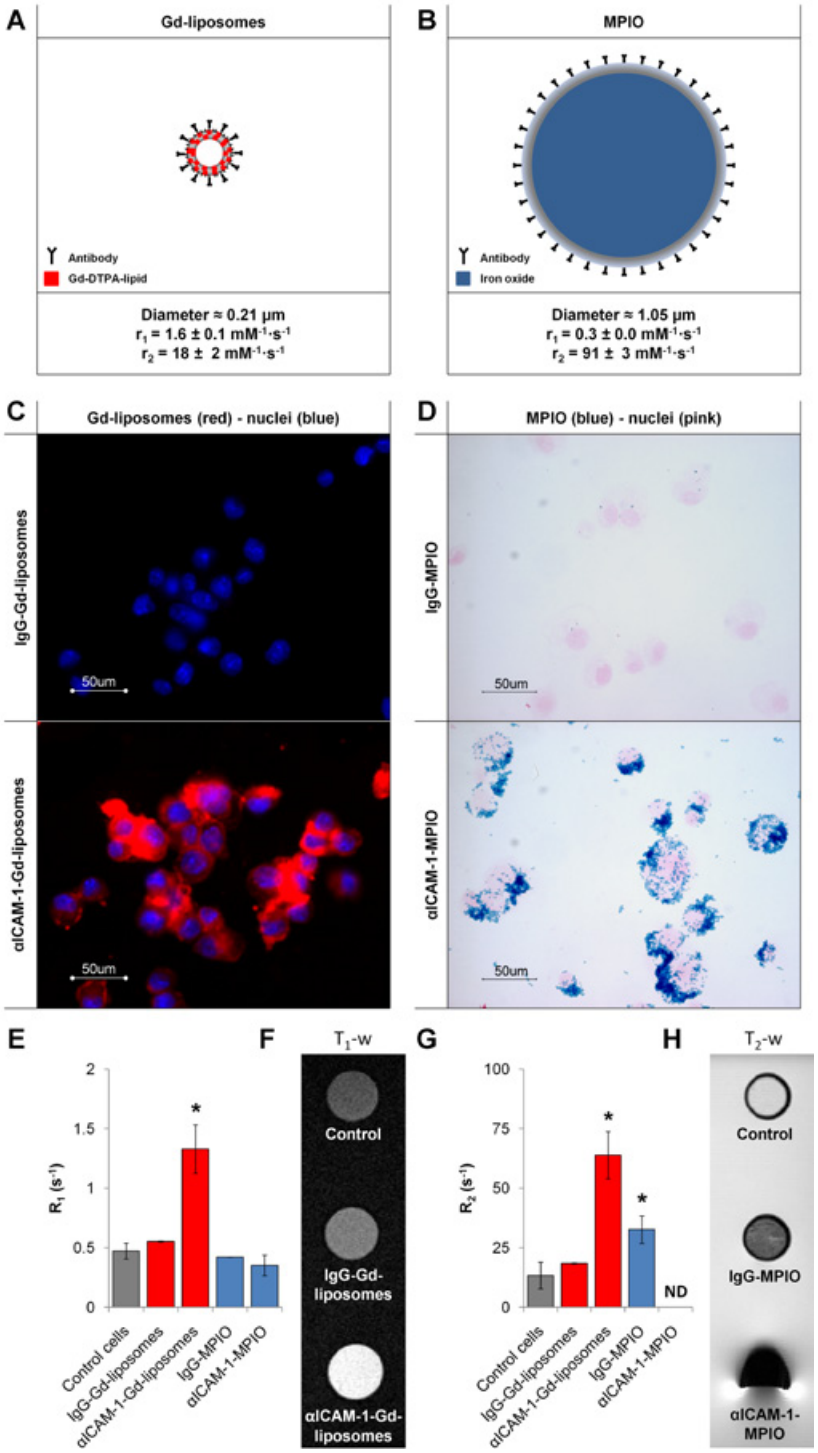

Figure 4.1

Gd-liposomes and MPIO targeted to ICAM-1 bind specifically to inflamed brain endothelial cells (bEnd.5), giving rise to faster MR relaxation and significant contrast effects on MR images. Schematic representation of **(A)** Gd-liposomes and **(B)** MPIO used for this study, with their corresponding diameter and relaxivities. **(C)** Fluorescent microscopy images (40x, scale bars represent 50 µm) of bEnd.5 incubated with IgG-Gd-liposomes (top panel) or αICAM-1-Gd-liposomes (bottom panel) and **(D)** light microscopy images (40x, scale bars represent 50 µm) of cells incubated with IgG-MPIO (top panel) or αICAM-1-MPIO (bottom panel). **(E)** Bar graph with R_1 ($1/T_1$) values of cell pellets, consisting of untreated control cells or cells incubated with IgG-Gd-liposomes, αICAM-1-Gd-liposomes, IgG-MPIO or αICAM-1-MPIO (n = 2 per group). * P < 0.05, bars represent mean ± SD. **(F)** A T_1-weighted Look-Locker image (TR/TE = 2000/3.18 ms) of cell pellets containing control cells or cells incubated with IgG-Gd-liposomes or αICAM-1-Gd-liposomes. **(G)** Bar graph with R_2 ($1/T_2$) values of cell pellets, consisting of untreated control cells or cells incubated with IgG-Gd-liposomes, αICAM-1-Gd-liposomes, IgG-MPIO or αICAM-1-MPIO (n = 2 per group). R_2 values of cells treated with αICAM-1-MPIO were too low to be determined (ND). * P < 0.05, bars represent mean ± SD. **(H)** A T_2-weighted spin echo image (TR/TE = 5000/9 ms) of cell pellets containing control cells or cells incubated with IgG- or αICAM-1-MPIO.

4.4.3 ICAM-1-targeted Gd-liposomes and MPIO increase cellular R_1 and/or R_2 *In vitro* MRI measurements were performed on pellets of TNFα-stimulated brain endothelial cells that were left untreated (control cells) or incubated with IgG-Gd-liposomes, αICAM-1-Gd-liposomes, IgG-MPIO or αICAM-1-MPIO to assess the contrast-generating efficacy on MR images. A significant two- to threefold increase in R_1 was found for cells that were incubated with αICAM-1-Gd-liposomes (1.3 ± 0.2 s^{-1}) compared to IgG-Gd-liposomes-treated (0.6 ± 0.0 s^{-1}) or control cells (0.5 ± 0.1 s^{-1}, **Figure 4.1E** and **F**).

This R_1 effect was not observed for cells incubated with αICAM-1-MPIO (0.4 ± 0.1 s^{-1}) when compared to IgG-MPIO-treated (0.4 ± 0.0 s^{-1}) or control cells. Cells incubated with αICAM-1-Gd-liposomes also showed a significant three- to fourfold increase in R_2 (64 ± 10 s^{-1}) compared to IgG-Gd-liposomes-incubated (18 ± 0 s^{-1}) or control cells (13 ± 6 s^{-1}, **Figure 4.1G**). Cells incubated with IgG-MPIO also showed a significant increase in R_2 (32 ± 6 s^{-1}, twofold increase compared to control cells), but in a lesser extent then αICAM-1-Gd-liposomes. More drastic changes were observed when cells were incubated with αICAM-1-MPIO; these induced such a strong T_2 shortening effect in the cells that R_2 values could not be calculated from the acquired images (**Figure 4.1H**). This meant that the cells displayed an R_2 value over 200 s^{-1}; the highest R_2 value measurable with the applied MRI protocol. Even though a quantitative measure of R_2 was not obtained, it could be concluded that αICAM-1-MPIO-loaded cells generated a more than tenfold increase in R_2 compared to control cells, which was more pronounced than the R_2 effect generated by cells incubated with either αICAM-1-Gd-liposomes or IgG-MPIO.

4.4.4 Brain tissue exposes increased levels of ICAM-1 mRNA and protein expression after stroke To obtain the optimal time point for *in vivo* detection of ICAM-1-expression with ICAM-1-targeted contrast agents, ICAM-1 mRNA levels and protein expression were evaluated at different time points after experimental stroke. mRNA levels were obtained by qPCR of *post mortem* brain tissue samples, while protein expression was visualized by immunohistochemical staining for ICAM-1 and detection with light microscopy. A significant increase in ipsilesional ICAM-1 mRNA levels was observed at 6 h (0.008 ± 0.004) and 24 h post-stroke (0.018 ± 0.004, **Figure 4.2A**), compared to contralesional values (6 h; 0.001 ± 0.000, 24 h; 0.005 ± 0.006) with a threefold increase at 24 h. This early increase in ICAM-1 mRNA in the ipsilesional hemisphere was associated with a marked upregulation of ICAM-1 expression in cortical and subcortical lesion areas at 24 h and 3 days after stroke onset **(Figure 4.2B).** ICAM-1-positive vessel-like structures were still detected at 7 days post-stroke, although to a lesser extent. ICAM-1 mRNA levels in the contralesional hemisphere did not change significantly over time, even though some ICAM-1-positive structures could be observed in the contralesional hemisphere at 24 h and 3 days post-stroke.

4.4.5 *In vivo* molecular MRI of post-stroke neuroinflammation is feasible with αICAM-1-MPIO αICAM-1-Gd-liposomes and αICAM-1-MPIO were subsequently explored for their applicability as target-specific contrast agents for molecular MRI of post-stroke ICAM-1 upregulation at 24 h (i.e., directly after i.v. contrast agent injection) and 48 h after stroke onset (i.e., 24 h after contrast agent injection). Typical examples of post-stroke mouse brain T_1 maps or T_2*-weighted MR images are shown in **Figure 4.3A and C**. The overall increased signal intensity in the lesion area – on pre- and post-contrast images – reflects stroke-induced edema. Minimal global contrast enhancement was observable in the ipsi- as well as contralesional hemispheres **(Figure 4.3A and B)** 1 h after administration of either IgG-Gd-liposomes (ipsilesional post-contrast signal: 96.5 ± 1.6 % (of pre-contrast); contralesional post-contrast signal: 96.7 ± 1.5 % (of pre-contrast) (n = 7)) or αICAM-1-Gd-liposomes (ipsilesional post-contrast signal: 97.2 ± 1.3 % (of pre-contrast); contralesional post-contrast signal: 97.0 ± 0.8 % (of pre-contrast) (n = 7)). On the other hand, evident hypointense structures appeared within 1 h on the T_2*-weighted images after injection of αICAM-1-MPIO (n = 5), but not IgG-MPIO (n = 6) **(Figure 4.3C)**. This contrast effect was restricted to the lesion area, in which a significant change of -7.4 ± 3.4 % in mean T_2*-weighted signal intensity was measured within 1 h after αICAM-1-MPIO injection, as compared to the -1.8 ± 1.9 % signal change in the contralesional hemisphere. Moreover, the ipsilesional αICAM-1-MPIO-induced signal reduction was significantly larger than the effect after IgG-MPIO injection **(Figure 4.3D)**. This indicates that the observed contrast in the αICAM-1-MPIO-injected animals originates from target-specific accumulation. This contrast effect, however, essentially disappeared within 24 h **(Figure 4.3C and D)**. Furthermore, at 24 h post-contrast agent injection, i.e., 48 h post-stroke, an increase in ipsilesional T_2*-weighted signal intensity and T_1 compared to pre-contrast agent injection images was detected in all animals **(Figure 4.3B and D)**. This signal change is opposite to the contrast agent-induced effects, and indicative of endogenous tissue-specific changes in the lesion area.

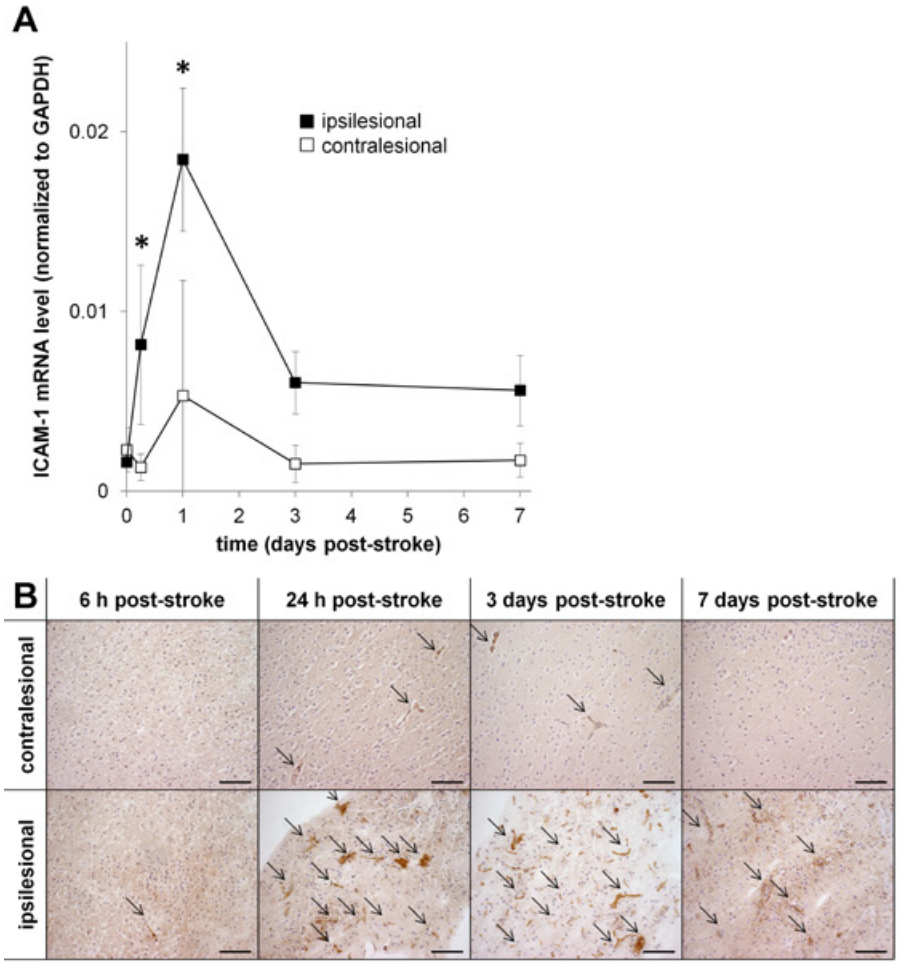

Figure 4.2

Post mortem brain tissue reveals a significant increase in ICAM-1 mRNA levels and protein expression after stroke. **(A)** mRNA levels of ICAM-1 (normalized to GAPDH) at 0 h, 6 h, 24 h, 3 days and 7 days post-stroke for ipsilesional and contralesional brain tissue (n = 4 per time-point, * P < 0.05 compared to contralesional brain tissue). **(B)** Light microscopy images (20x, scale bars represent 100 µm) of ICAM-1 protein expression (brown) in the sensorimotor cortex inside the lesion area and its contralesional counterpart, at 6 h, 24 h, 3 days and 7 days after stroke. Nuclei are depicted in blue. Arrows indicate ICAM-1-positive vessels.

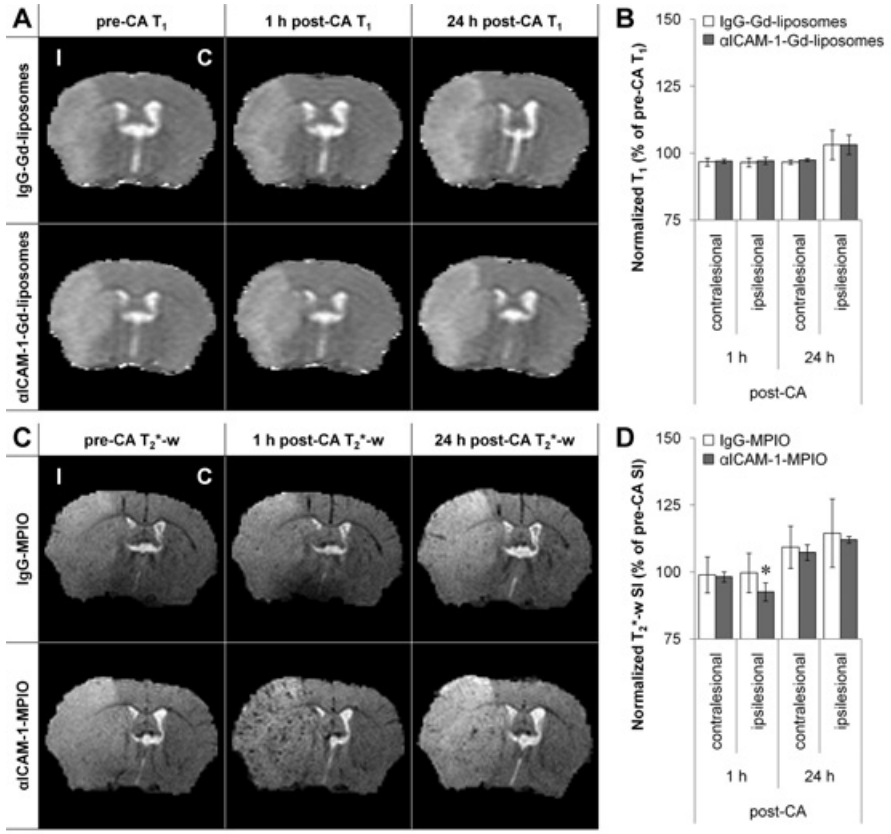

Figure 4.3

In vivo molecular MRI of neuroinflammation after experimental stroke is evidently feasible with αICAM-1-MPIO, but not with αICAM-1-Gd-liposomes. **(A)** Representative pre-contrast agent (CA), and 1 and 24 h post-CA T_1 maps of animals that received IgG-Gd-liposomes or αICAM-1-Gd-liposomes. The ipsilesional and contralesional sides are depicted in the first image with 'I' and 'C', respectively. The lesion is characterized by edema-associated signal increase in pre- and post-CA images. **(B)** Bar graph showing normalized T_1 in ipsilesional and contralesional ROIs at 1 and 24 h post-CA. Values are normalized to mean pre-CA T_1 values within the defined ROI (n = 7 per group). Bars represent mean ± SD. **(C)** Representative pre-CA, and 1 and 24 h post-CA T_2*-weighted images of animals that received IgG-MPIO or αICAM-1-MPIO. The ipsilesional and contralesional sides are depicted in the first image with 'I' and 'C', respectively. The lesion is characterized by edema-associated signal increase in pre- and post-CA images, while a vascular pattern of hypointensities appeared after αICAM-1-MPIO injection. **(D)** Bar graph showing normalized T_2*-weighted signal intensity (SI) in ipsilesional and contralesional ROIs at 1 h and 24 h post-CA. Values are normalized to mean pre-CA T_2*-weighted SI values within the specific ROI (IgG-MPIO; n = 6, αICAM-1-MPIO; n = 5). Bars represent mean ± SD. * P < 0.05 vs. IgG-MPIO.

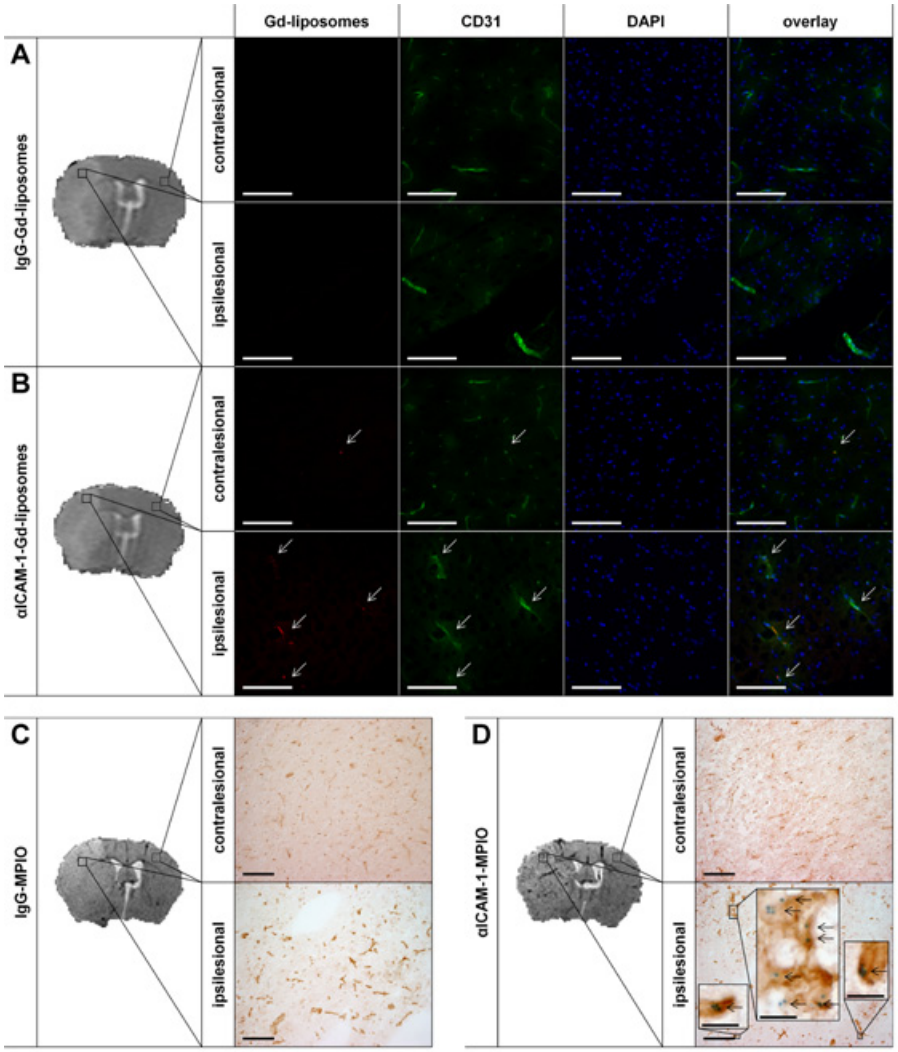

Figure 4.4

αICAM-1-Gd-liposomes and αICAM-1-MPIO specifically target inflamed post-stroke vasculature *in vivo*, but only αICAM-1-MPIO generate specific contrast enhancement on MR images. **(A, B)** *In vivo* T_1-map (first column) and *post mortem* fluorescence microscopy images (20x, scale bars represent 100 µm) of contralesional and ipsilesional brain tissue of a mice that received **(A)** IgG-Gd-liposomes or **(B)** αICAM-1-Gd-liposomes at 48 h after MCAo. Second column shows rhodamine signal of Gd-liposomes (red), third column shows CD31-stained vessels (green), fourth column shows DAPI-stained nuclei (blue) and fifth column shows overlay of all channels. White arrows indicate overlay of Gd-liposome signal and vessel staining. **(C, D)** *In vivo* T_2*-weighted image and *post mortem* light microscopy images (20x, scale bars represent 100 µm) of contralesional and ipsilesional brain tissue of mice that received **(C)** IgG-MPIO or **(D)** αICAM-1-MPIO at 24 h after MCAo. Inserts show magnifications (scale bars represent 10 µm) of detected MPIO indicated with black arrows. MPIO were stained with Perls' (blue), vessels with CD31 (brown) and nuclei with nuclear fast red (pink).

4.4.6 Both αICAM-1-Gd-liposomes and αICAM-1-MPIO specifically target inflamed vasculature *in vivo* To determine contrast agent accumulation and distribution in post-stroke brain tissue, mice were terminated after MRI at 48 h post-stroke for Gd-liposomes (n = 5) or at 24 h post-stroke for MPIO (n = 5), and brain sections were analyzed with (fluorescence) immunohistochemistry. Fluorescence microscopy images of mice that had received IgG-Gd-liposomes did not reveal any rhodamine fluorescence originating from Gd-liposomes **(Figure 4.4A)**, whereas Gd-liposomes were abundantly observed co-localized with blood vessels in ipsilesional, but not contralesional, tissue of mice that were injected with αICAM-1-Gd-liposomes **(Figure 4.4B)**. Similar results were obtained when analyzing brains of mice that had received MPIO. Upon administration of IgG-MPIO, MPIO were not detected in the affected hemisphere **(Figure 4.4C)**, while clear presence of MPIO co-localizing with vessel staining was observed on brain sections of mice that had received αICAM-1-MPIO **(Figure 4.4D)**, in the same ipsilesional regions where *in vivo* contrast enhancement was observed with MRI. No MPIO were detected in the contralesional hemisphere. These results indicate that both ICAM-1-targeted contrast agents, but not IgG-functionalized contrast agents, bind to inflamed cerebrovasculature after stroke.

4.5 DISCUSSION

In this study we report on the suitability of *in vivo* MR imaging of neuroinflammation after a cerebrovascular accident by using contrast agents directed against the endothelial marker ICAM-1. We compared two of the most potent MR contrast agents in their categories, i.e., T_1-shortening Gd-liposomes and $T_2^{(*)}$-shortening MPIO. Molecular MRI was performed at a timepoint of significant stroke-induced ICAM-1 expression, and we found that significant and specific *in vivo* MRI-based detection of ICAM-1 was only achieved with αICAM-1-MPIO. However, *in vitro* studies demonstrated that ICAM-1 expressing endothelial cells could be efficiently labeled and detected with αICAM-1-MPIO as well as αICAM-1-Gd-liposomes. Furthermore, *post mortem* microscopic analysis of brain tissue showed target-specific vascular accumulation of both contrast agent types. Our data demonstrate the feasibility of *in vivo* targeting of stroke-induced ICAM-1

upregulation in the brain and confirm the specificity of both ICAM-1-targeted contrast agents, but signify αICAM-1-MPIO as the most suitable contrast agent for *in vivo* MR imaging of early neuroinflammation after cerebrovascular injury.

The high potency of αICAM-1-MPIO as a molecular MR contrast agent is in line with previous molecular MRI studies using antibody-functionalized MPIO to detect ICAM-1 in radiation-induced brain injury [28] and endothelial VCAM-1 expression in various animal models of central nervous system disease [14, 29-30]. MPIO have a very short blood half-life (order of minutes) [31-32] and therefore a small time window for target binding. Nevertheless, this time window appears to be sufficient for extensive accumulation at vascular sites with increased expression of cell adhesion molecules. Moreover, the rapid blood clearance of MPIO minimizes non-specific contrast effects due to circulating contrast agent. This was demonstrated in our study, in which contrast-induced effects in post-stroke brain tissue were clearly present 1 h after injection with αICAM-1-MPIO, but not with IgG-MPIO. MPIO presence could no longer be detected 24 h after contrast agent injection, despite continued overexpression of ICAM-1, which points toward target-particle dissociation or degradation of the particles.

Despite the clear potential of αICAM-1-MPIO for molecular MRI of neuroinflammation, it may be advantageous to use T_1-shortening contrast agents under some conditions. For instance, in case of high endogenous iron accumulation, e.g., due to hemorrhages or presence of macrophages loaded with iron-containing biological debris. These endogenous iron oxide deposits also induce $T_2^{(*)}$-shortening, which can bias the interpretation of hypointense areas on $T_2^{(*)}$-weighted MR images [33]. This problem may be circumvented by application of T_1-shortening Gd-chelate-based contrast agents, such as Gd-liposomes that have been proven suitable for *in vivo* molecular MRI purposes in a variety of animal models of disease, including tumor angiogenesis [34]. In our study, we showed that specific *in vivo* MRI-based detection of ICAM-1 after stroke was not feasible with ICAM-1-targeted T_1-shortening Gd-liposomes. Previously, ICAM-1-targeted paramagnetic polymerized liposomes have been successfully employed in a mouse model of experimental autoimmune encephalitis [35]. However, to achieve sensitive detection, *post mortem* T_1-weighted MR images were obtained at a very high spatial resolution of 40 µm, which required an acquisition time of 7 h. In our *in vivo* stroke model, we also evaluated the effect of Gd-liposomes. In these liposomal formulations, a high degree of PEGylation ensures a relatively long circulation time (order of hours) by shielding the particles from the mononuclear phagocyte system [36-37] securing a larger time window for the particles to bind to ICAM-1. However, prolonged presence of circulating Gd-liposomes also obscures specific detection of bound Gd-liposomes, which is only feasible after circulating contrast agent has been cleared from the blood [38]. In fact, we observed a small contrast effect in the entire brain at 1 h after injection of αICAM-1-Gd-liposomes or IgG-Gd-liposomes, reflective of global, non-specific presence of Gd-liposomes. In our study, antibodies were coupled to Gd-liposomes, which have been reported to shorten the blood half-life [39], abolishing the hindering effect of circulating Gd-liposomes at 1 h after injection. Nevertheless, clear and specific contrast effects of αICAM-1-Gd-liposomes were not observed acutely or 24 h after injection in post-stroke mice, despite target-specific accumulation as demonstrated from immunohistochemistry.

A plausible explanation for the scarce MR contrast effects by αICAM-1-Gd-liposomes as compared to αICAM-1-MPIO is the intrinsically lower contrast-generating efficacy of the former. T_1 values of cells incubated with αICAM-1-Gd-liposomes showed a measurable threefold increase compared to control and IgG-Gd-liposomes-treated cells, which is in accordance with previous *in vitro* studies using paramagnetic ICAM-1-targeted liposomes [40]. On the other hand, αICAM-1-MPIO induced such a substantial $T_2^{(*)}$ shortening effect that it could not be determined with our T_2 fitting routine, which would have allowed reliable quantification of T_2 up to about 5 ms (R_2 of 200 s^{-1}). To compensate for this difference in contrast-generating efficacy, Gd-liposomes would require injections with much higher concentrations as compared to MPIO for significant target detection. However, a higher dose of Gd-liposomes will also increase the blood-half life [41] and potentially introduces more non-specific accumulation. In our study, we chose dosages that have been successfully applied in mice for previous molecular MRI studies with Gd-liposomes [34, 42] and MPIO [14, 43].

An alternative explanation for the reduced contrast-generating efficiency of Gd-liposomes is possible quenching of the T_1 effect due to internalization and compartmentalization in cells [44], although previous studies have shown conflicting results on internalization of ICAM-1-targeted liposomes [40, 45]. Furthermore, pathology-associated intrinsic changes in tissue contrast as observed in the present study, where the T_1 of lesioned tissue significantly increased between 24 and 48 h post-stroke, would also hinder chronic detection of a T_1-shortening contrast agent.

The current study highlights the applicability of target-specific MPIO as a potent molecular MR contrast agent in studies on brain disorders. Furthermore, our data expose ICAM-1 as a promising target for molecular MR imaging of stroke-induced

neuroinflammation. ICAM-1 is maximally expressed at later time points after stroke as compared to other cell adhesion molecules, such as selectins [18] and VCAM-1 [19], which could considerably expand the potential of molecular imaging strategies for long-term *in vivo* monitoring of neuroinflammation after stroke. Since ICAM-1 may not be solely expressed by endothelial cells and can also be present on different types of leukocytes [46], this could open up additional opportunities for imaging of inflammatory cells. The current study reports on the application of ICAM-1-targeted contrast agents at 24 h after stroke onset, when the infiltration of ICAM-1 presenting leukocytes is still relatively limited [47-48]. Furthermore, specific co-localization with vascular markers suggests predominant association of αICAM-1-contrast agents with the endothelium in the presented data.

4.6 CONCLUSIONS

In conclusion, target-specific MPIO provide a more potent contrast agent platform than Gd-liposomes for *in vivo* molecular MRI of cell adhesion molecules as neuroinflammatory biomarkers after cerebrovascular injury, with high target specificity and high MR sensitivity. In addition to its potential for preclinical studies, recent development of a biodegradable MPIO [49] may open the door to possible clinical applications in the future

4.7 REFERENCES

1. Iadecola C, Anrather J (2011) The immunology of stroke: from mechanisms to translation. Nat Med 17:796-808.
2. Thakur M, Lentle BC (2005) Report of a summit on molecular imaging. Radiology 236:753-755.
3. Gupta H, Weissleder R (1996) Targeted contrast agents in MR imaging. Magn Reson Imaging Clin N Am 4:171-184.
4. Dijkhuizen RM, Nicolay K (2003) Magnetic resonance imaging in experimental models of brain disorders. J Cereb Blood Flow Metab 23:1383-1402.
5. Baird AE, Warach S (1998) Magnetic resonance imaging of acute stroke. J Cereb Blood Flow Metab 18:583-609.
6. Deddens LH, Van Tilborg GA, Mulder WJ, De Vries HE, Dijkhuizen RM (2012) Imaging neuroinflammation after stroke: current status of cellular and molecular MRI strategies. Cerebrovasc Dis 33:392-402.
7. Muller RN, Roch A, Colet J-M, Ouakssim A, Gillis P (2001) Particulate magnetic contrast agents. In The chemistry of contrast agents in medical magnetic resonance imaging, Eds. Merbach AE, Tóth E. John Wiley & Sons, Ltd, pp 417-435.
8. Wijagkanalan W, Kawakami S, Hashida M (2011) Designing dendrimers for drug delivery and imaging: pharmacokinetic considerations. Pharm Res 28:1500-1519.
9. Mulder WJ, Strijkers GJ, Van Tilborg GA, Griffioen AW, Nicolay K (2006) Lipid-based nanoparticles for contrast-enhanced MRI and molecular imaging. NMR Biomed 19:142-164.
10. Laurent S, Boutry S, Mahieu I, Vander Elst L, Muller RN (2009) Iron oxide based MR contrast agents: from chemistry to cell labeling. Curr Med Chem 16:4712-4727.
11. Barber PA, Foniok T, Kirk D, Buchan AM, Laurent S, Boutry S, Muller RN, Hoyte L, Tomanek B, Tuor UI (2004) MR molecular imaging of early endothelial activation in focal ischemia. Ann Neurol 56:116-120.
12. Jin AY, Tuor UI, Rushforth D, Filfil R, Kaur J, Ni F, Tomanek B, Barber PA (2009) Magnetic resonance molecular imaging of post-stroke neuroinflammation with a P-selectin targeted iron oxide nanoparticle. Contrast Media Mol Imaging 4:305-311.
13. Van Kasteren SI, Campbell SJ, Serres S, Anthony DC, Sibson NR, Davis BG (2009) Glyconanoparticles allow pre-symptomatic *in vivo* imaging of brain disease. Proc Natl Acad Sci U S A 106:18-23.
14. Hoyte LC, Brooks KJ, Nagel S, Akhtar A, Chen R, Mardiguian S, McAteer MA, Anthony DC, Choudhury RP, Buchan AM, Sibson NR (2010) Molecular magnetic resonance imaging of acute vascular cell adhesion molecule-1 expression in a mouse model of cerebral ischemia. J Cereb Blood Flow Metab 30:1178-1187.
15. Breckwoldt MO, Chen JW, Stangenberg L, Aikawa E, Rodriguez E, Qiu S, Moskowitz MA, Weissleder R (2008) Tracking the inflammatory response in stroke *in vivo* by sensing the enzyme mye loperoxidase. Proc Natl Acad Sci U S A 105:18584-18589.
16. Zhang RL, Chopp M, Zaloga C, Zhang ZG, Jiang N, Gautam SC, Tang WX, Tsang W, Anderson DC, Manning AM (1995) The temporal profiles of ICAM-1 protein and mRNA expression after transient MCA occlusion in the rat. Brain Res 682:182-188.
17. Shyu KG, Chang H, Lin CC (1997) Serum levels of intercellular adhesion molecule-1 and E-selectin in patients with acute ischaemic stroke. J Neurol 244:90-93.

18. Okada Y, Copeland BR, Mori E, Tung MM, Thomas WS, del Zoppo GJ (1994) P-selectin and intercellular adhesion molecule-1 expression after focal brain ischemia and reperfusion. Stroke 25:202-211.

19. Justicia C, Martin A, Rojas S, Gironella M, Cervera A, Panes J, Chamorro A, Planas AM (2006) Anti-VCAM-1 antibodies did not protect against ischemic damage either in rats or in mice. J Cereb Blood Flow Metab 26:421-432.

20. Everts M, Koning GA, Kok RJ, Asgeirsdottir SA, Vestweber D, Meijer DK, Storm G, Molema G (2003) In vitro cellular handling and *in vivo* targeting of E-selectin-directed immunoconjugates and immunoliposomes used for drug delivery to inflamed endothelium. Pharm Res 20:64-72.

21. Koning GA, Morselt HW, Velinova MJ, Donga J, Gorter A, Allen TM, Zalipsky S, Kamps JA, Scherphof GL (1999) Selective transfer of a lipophilic prodrug of 5-fluorodeoxyuridine from immunoliposomes to colon cancer cells. Biochim Biophys Acta 1420:153-167.

22. Rouser G, Fkeischer S, Yamamoto A (1970) Two dimensional then layer chromatographic separation of polar lipids and determination of phospholipids by phosphorus analysis of spots. Lipids 5:494-496.

23. Wagner EF, Risau W (1994) Oncogenes in the study of endothelial cell growth and differentiation. Semin Cancer Biol 5:137-145.

24. Perls M (1867) Nachweis von Eisenoxyd in gewissen Pigmenten. Virchows Archiv 39:42-48.

25. Oude Engberink RD, Van der Pol SM, Dopp EA, De Vries HE, Blezer EL (2007) Comparison of SPIO and USPIO for *in vitro* labeling of human monocytes: MR detection and cell function. Radiology 243:467-474.

26. Hata R, Mies G, Wiessner C, Fritze K, Hesselbarth D, Brinker G, Hossmann KA (1998) A reproducible model of middle cerebral artery occlusion in mice: hemodynamic, biochemical, and magnetic resonance imaging. J Cereb Blood Flow Metab 18:367-375.

27. Bouts MJ, Tiebosch IA, Zwartbol R, Hoogveld E, Wu O, Dijkhuizen RM (2011) Early prediction of salvageable tissue with multiparametric MRI-based algorithms after experimental ischemic stroke. Proceedings International Society for Magnetic Resonance in Medicine 19: 2141P.

28. Zhu Y, Ling Y, Zhong J, Liu X, Wei K, Huang S (2012) Magnetic reso nance imaging of radiation-induced brain injury using targeted micropar ticles of iron oxide. Acta Radiol 53:812-819.

29. Serres S, Mardiguian S, Campbell SJ, McAteer MA, Akhtar A, Krapitchev A, Choudhury RP, Anthony DC, Sibson NR VCAM-1-targeted magnetic resonance imaging reveals subclinical disease in a mouse model of multiple sclerosis. FASEB J 25:4415-4422.

30. Montagne A, Gauberti M, Macrez R, Jullienne A, Briens A, Raynaud JS, Louin G, Buisson A, Haelewyn B, Docagne F, Defer G, Vivien D, Maubert E (2012) Ultra-sensitive molecular MRI of cerebrovascular cell activation enables early detection of chronic central nervous system disorders. Neuroimage 63:760-770.

31. Yang Y, Yanasak N, Schumacher A, Hu TC (2010) Temporal and noninvasive monitoring of inflammatory-cell infiltration to myocardial infarction sites using micrometer-sized iron oxide particles. Magn Reson Med 63:33-40.

32. Ye Q, Wu YL, Foley LM, Hitchens TK, Eytan DF, Shirwan H, Ho C (2008) Longitudinal tracking of recipient macrophages in a rat chronic cardiac allograft rejection model with non invasive magnetic resonance imaging using micrometer-sized paramagnetic iron oxide particles. Circulation 118:149-156.

33. Vandeputte C, Thomas D, Dresselaers T, Crabbe A, Verfaillie C, Baekelandt V, Van Laere K, Himmelreich U (2011) Characterization of the inflammatory response in a photothrombotic stroke model by MRI: implications for stem cell transplantation. Mol Imaging Biol 13:663-671.

34. Mulder WJ, Strijkers GJ, Habets JW, Bleeker EJ, Van der Schaft DW, Storm G, Koning GA, Griffioen AW, Nicolay K (2005) MR molecular imaging and fluorescence micro scopy for identification of activated tumor endothelium using a bimodal lipidic nanoparticle. FASEB J 19:2008-2010.

35. Sipkins DA, Gijbels K, Tropper FD, Bednarski M, Li KC, Steinman L (2000) ICAM-1 expression in autoimmune encephalitis visualized using magnetic resonance imaging. J Neuroimmunol 104:1-9.

36. Drummond DC, Meyer O, Hong K, Kirpotin DB, Papahadjopoulos D (1999) Optimizing liposomes for deli very of chemotherapeutic agents to solid tumors. Pharmacol Rev 51:691-743.

37. Woodle MC, Matthay KK, Newman MS, Hidayat JE, Collins LR, Redemann C, Martin FJ, Papahadjopoulos D (1992) Versatility in lipid compositions showing prolonged circulation with sterically stabilized liposomes. Biochim Biophys Acta 1105:193-200.

38. Van Tilborg GA, Mulder WJ, Van der Schaft DW, Reutelingsperger CP, Griffioen AW, Strijkers GJ, Nicolay K (2008) Improved magnetic resonance molecular imaging of tumor angiogenesis by avidin-induced clearance of nonbound bimodal liposomes. Neoplasia 10:1459-1469.

39. Paulis LE, Jacobs I, Van den Akker NM, Coolen BF, Geelen T, Nicolay K, Strijkers GJ (2011) *In vivo* molecular MRI of ICAM-1 expression in murine cardiac ischemia/reperfusion using a liposomal nanoparticle. Proceedings International Society for Magnetic Resonance in Medicine 19: 1660P.

40. Paulis LE, Jacobs I, van de Akker N, Geelen T, Molin D, Starmans LW, Nicolay K, Strijkers GJ (2012) Targeting of ICAM-1 on vascular endothelium under static and shear stress conditions using a liposomal Gd-based MRI contrast agent. J Nanobiotechnology 10:25.

41. Abra RM, Hunt CA (1981) Liposome disposition *in vivo*. III. Dose and vesicle-size effects. Biochim Biophys Acta 666:493-503.

42. Van Tilborg GA, Strijkers GJ, Pouget EM, Reutelingsperger CP, Sommerdijk NA, Nicolay K, Mulder WJ (2008) Kinetics of avidin-induced clearance of biotinylated bimodal liposomes for improved MR molecular imaging. Magn Reson Med 60:1444-1456.

43. McAteer MA, Sibson NR, von Zur Muhlen C, Schneider JE, Lowe AS, Warrick N, Channon KM, Anthony DC, Choudhury RP (2007) *In vivo* magnetic resonance imaging of acute brain inflammation using microparticles of iron oxide. Nat Med 13:1253-1258.

44. Kok MB, Hak S, Mulder WJ, Van der Schaft DW, Strijkers GJ, Nicolay K (2009) Cellular compartmentalization of internalized paramagnetic liposomes strongly influences both T_1 and T_2 relaxivity. Magn Reson Med 61:1022-1032.

45. Mastrobattista E, Storm G, van Bloois L, Reszka R, Bloemen PG, Crommelin DJ, Henricks PA (1999) Cellular uptake of liposomes targeted to intercellular adhesion molecule-1 (ICAM-1) on bronchial epithelial cells. Biochim Biophys Acta 1419:353-363.

46. Van de Stolpe A, Van der Saag PT (1996) Intercellular adhesion molecule-1. J Mol Med (Berl) 74:13-33.

47. Zhou W, Liesz A, Bauer H, Sommer C, Lahrmann B, Valous N, Grabe N, Veltkamp R (2012) Postischemic brain infiltration of leukocyte subpopulations differs among murine permanent and transient focal cerebral ischemia models. Brain Pathol 23:34-44.

48. Schilling M, Besselmann M, Leonhard C, Mueller M, Ringelstein EB, Kiefer R (2003) Microglial activation precedes and predominates over macrophage infiltration in transient focal cerebral ischemia: a study in green fluorescent protein transgenic bone marrow chimeric mice. Exp Neurol 183:25-33.

49. Nkansah MK, Thakral D, Shapiro EM (2011) Magnetic poly(lactide-co-glycolide) and cellulose particles for MRI-based cell tracking. Magn Reson Med 65:1776-1785.

MOLECULAR MRI OF ACTIVATED ENDOTHELIUM AND INFILTRATING LEUKOCYTES AFTER STROKE

Based on:
Lisette H. Deddens, Geralda A.F. van Tilborg, Kajo van der Marel, Hedi Hunt, Annette van der Toorn, Max A. Viergever, Helga E. de Vries and Rick M. Dijkhuizen.
Molecular MRI of ICAM-1 expression after experimental stroke: Imaging activated endothelium and infiltrating leukocytes (in preparation)

05

5.1 ABSTRACT

Molecular magnetic resonance imaging (MRI) has shown to be effective for detection of vascular cell adhesion molecules that are exclusively expressed on inflamed endothelium in a variety of cerebral pathologies. In this study, we explored to what extent MR contrast agent targeted to intercellular adhesion molecule-1 (ICAM-1), a cell adhesion molecule that is expressed on endothelium as well as leukocytes, is able to detect and distinguish endothelial- and leukocyte-associated ICAM-1 expression after experimental stroke. Furthermore, we assessed potential interfering effects of ICAM-1-targeted contrast agent on post-stroke lesion growth. To this end, micron-sized particles of iron oxide (MPIO) functionalized with control IgG (IgG-MPIO) or anti-ICAM-1 antibody (αICAM-1-MPIO) were administrated at 1, 2, 3, 7 and 21 days after unilateral transient middle cerebral artery occlusion (MCAo) in mice, followed by *in vivo* MRI and *post mortem* immunohistochemistry detection. At 1 h post-injection, αICAM-1-MPIO induced significant MR contrast effects in the lesion core on post-stroke days 1, 2 and 3, and in the lesion borderzone and contralesional tissue on post-stroke day 2. αICAM-1-MPIO were confined to ICAM-1-positive vessels and occasionally co-localized with leukocytes. No αICAM-1-MPIO were detected on post-stroke day 7. After 21 days, abundant leukocytes and associated αICAM-1-MPIO were immunohistochemically detected in the lesion core. However, MRI-based detection of αICAM-1-MPIO-coupled leukocytes was confounded by pre-contrast MRI hypointensities, possibly due to phagocytosed blood remains. IgG-MPIO did not induce significant MRI contrast effects at 1 h after injection, and were not detected in *post mortem* brain tissue. Lesion development was not affected by injection of αICAM-1-MPIO or IgG-MPIO. We conclude that αICAM-1-MPIO are suitable for *in vivo* MRI of stroke-induced ICAM-1 expression on vascular endothelium and leukocytes at different stages after stroke in mice. However, contrast effects from endogenous blood remains can significantly hamper the detection.

5.2 INTRODUCTION

Molecular magnetic resonance imaging (MRI) is an upcoming field in preclinical imaging, enabling direct measurement and a better understanding of cellular and molecular processes in living organisms [1-6]. Especially, ongoing pathogenic processes in the brain may be optimally visualized in this non-invasive manner. We and others have recently applied molecular MRI for the detection of neurovascular inflammation in rodent models of neurological disorders [7-12]. Such an approach can give more insights into inflammatory events involved in cerebral pathology, and aid in monitoring the efficacy of anti-inflammatory treatment strategies in a longitudinal way. Entities expressed on the luminal side of the cerebral endothelium can be directly targeted with MR contrast agents to which specific ligands are conjugated. For instance, successful detection of enhanced P- and E-selectin expression after experimental brain injuries, e.g., stroke, has been established with use of sialyl Lewis^X (sLe^X)-targeted Gd-chelates [7, 12] and iron oxides [10]. Similarly, vascular cell adhesion molecule-1 (VCAM-1) has been effectively targeted and imaged using antibody-functionalized iron oxides in a variety of brain disorders [8-9, 11]. These targets are typically expressed on the intraluminal side of the endothelial wall, and MR contrast can therefore be attributed to contrast agent bound to its vascular target.

We have recently developed an optimized molecular MRI approach for the detection of stroke-induced upregulation of intercellular adhesion molecule-1 (ICAM-1) [13]. ICAM-1 is a cell adhesion molecule that is upregulated during neurovascular inflammation, and involved in tight endothelial binding and transmigration of leukocytes [14-15]. ICAM-1 has been implicated in stroke pathophysiology, and has been shown to provide an effective therapeutic target for reduction of ischemic lesion development [16]. Experimental studies have demonstrated that injection of antibodies against ICAM-1 significantly reduce infarct size after transient unilateral stroke in rats [17], although a clinical trial using a murine monoclonal anti-human ICAM-1 antibody (Enlimomab) failed to reproduce this effect [18]. In contrast to the abovementioned selectins and VCAM-1, ICAM-1 is not only expressed on (inflamed) endothelium, but also on leukocytes. This provides an interesting opportunity to image endothelial activation as well as leukocyte invasion in relation to stroke pathophysiology and (anti-inflammatory) treatment. However, it remains unknown to what extent molecular MRI of ICAM-1 expression in the brain reflects these specific inflammatory processes that may occur separately as well as jointly. The primary goal of our study was to determine the diagnostic potential of ICAM-1-targeted MPIO for *in vivo* MRI of vascular ICAM-1 expression and leukocyte infiltration at different stages after transient unilateral stroke in mice. In addition, we assessed possible interfering effects of ICAM-1-targeted MPIO on post-stroke lesion development.

5.3 MATERIALS AND METHODS

5.3.1 Preparation of antibody-functionalized MPIO ProMag™ 1 Series, Bind-IT™ MPIO (25 mg MPIO/ml, 26.5 % iron-content) were obtained from Bangs Laboratories, Inc. (Fishers, IN, USA), and extracted from their original buffer by magnetic separation and resuspended in coupling buffer (50 mM 2-(N-morpholino)ethanesulfonic acid (MES); pH 5.2). Prior to the coupling procedure, a monoclonal antibody against mouse ICAM-1 (αICAM-1, YN1/1.7.4) and irrelevant immunoglobulin G antibody (IgG, RTK4530) (BioLegend; San Diego, CA, USA) were buffer-exchanged to coupling buffer by centrifugation, resulting in a final antibody concentration of 1.0 mg/ml. Next, MPIO and αICAM-1 or IgG were added in a 1:1 (v/v) ratio, vortexed and left to incubate for 60 min at room temperature on a roller-bench. Following incubation, antibody-MPIO were buffer-exchanged to storage solution (150 mM NaCl with 0.002 % azide) by magnetic separation and stored at 4 ˚C at a concentration of 12.5 mg MPIO/ml.

5.3.2 Mouse stroke model All animal procedures were approved by the Utrecht University Ethical Committee on Animal Experiments, and experiments were performed in accordance with the guidelines of the European Communities Council Directive. Eight-week-old C57Bl/6 mice, weighing 20 to 25 g (Harlan, Horst, The Netherlands) were anesthetized with isoflurane (3.5 % induction, 1.5-2.0 % maintenance) in air/O_2 (2:1). Body temperature was maintained at 37.0 ± 0.5 ˚C. Transient focal cerebral ischemia was induced by 30 min right middle cerebral artery occlusion (MCAo) with an intraluminal filament [19]. In brief, a 7.0 polypropylene suture with a silicon-coated tip (tip diameter of 0.21 mm, Doccol Corporation, Redlands, CA, USA) was introduced into the right external carotid artery and advanced through the internal carotid artery until a slight resistance was felt, indicating that the MCA was occluded. During occlusion, the common carotid artery was clipped. After 30 min, the filament was withdrawn from the internal carotid artery and the clip was removed from the common carotid artery to allow full reperfusion. Before surgery, mice received a 1 ml subcutaneous injection of saline to compensate for loss of water and minerals, and a subcutaneous injection of 0.1 mg/kg buprenorphine (Temgesic; Schering-Plough, Houten, The Netherlands) for post-surgical analgesia.

5.3.3 *In vivo* MRI Mice underwent *in vivo* MRI on a 9.4 T MR system (Agilent, Palo Alto, Ca, USA) under general isoflurane anesthesia. Multi-spin echo MRI was applied for T_2 mapping (repetition time (TR)/echo time (TE) 2300/12-96 ms; number of echoes (NE) 8; number of acquisitions (NA) 4; matrix size 192 x 96, field-of-view (FOV) 20 x 20 mm^2, 21 slices of 400 μm thickness) to determine lesion size. T_2*-weighted images (3D gradient echo; TR/TE 35/15 ms; NA 8; flip angle (FA) 10˚; matrix size 96 x 80 x 160; FOV 10 x 12 x 20 mm^3) were acquired before and up to 1 h after i.v. injection of IgG-MPIO or αICAM-1-MPIO (5 mg iron/kg body weight). Mice were sacrificed immediately after the last MRI scan by an overdose of isoflurane anesthesia followed by transcardial perfusion with PBS. Fresh brains were quickly excised, snap-frozen with liquid N_2 and stored at -80 ˚C for *post mortem* immunohistochemistry.

5.3.4 *Post mortem* immunohistochemistry For *post mortem* immunohistochemistry, cryosections of 10 μm (6 per mouse, ranging from approximately -1 to +1.5 mm from Bregma) were prepared. Subsequently, tissue was stained for either ICAM-1 or CD45, followed by Perls' staining for MPIO. Therefore, tissue was dried overnight and acetone-fixated for 10 min at room temperature. After the acetone was evaporated, tissue was hydrated in PBS/0.1 % BSA and incubated for 1 h with biotinylated αICAM-1 (10 μg antibody/ml of PBS/0.1 % BSA; αICAM-1-biotin, YN1/1.7.4; BioLegend; San Diego, CA, USA) or biotinylated αCD45 (23 μg antibody/ml of PBS/0.1% BSA; αCD45-biotin, MP33; production in house), followed by incubation with horseradish peroxidase-labeled streptavidin (HRPstrep; DAKO, Glostrup, Denmark; prepared according to the manufacturer's description) for 45 min. Diaminobenzidine solution (DAB; Sigma-Aldrich, St. Louis, MO, USA) was used as chromogen (used according to the manufacturer's description). Tissue was subsequently incubated with Perls' solution (2 N HCl and 2 % ferrocyanide in Milli-Q in 1:1 (v/v) ratio) for 20 min, thoroughly washed with Milli-Q, dipped in a nuclear fast red solution, dehydrated, and slides were mounted in Entallan.

5.3.5 Study I: Diagnostic efficacy of αICAM-1-MPIO To test the efficacy of αICAM-1-MPIO to detect post-stroke ICAM-1 expression on brain endothelium and/or infiltrated leukocytes, 45 mice underwent transient MCAo after which cross-sectional MRI was done at 1, 2, 3, 7, or 21 days. Six mice were excluded from the study: three mice died before MRI acquisition (day 1: n = 1; day 7: n = 2), two mice had no lesion (day 3: n = 1; day 21: n = 1) and one mouse received no contrast agent (day 1: n = 1). After baseline MRI measurements, mice were injected with IgG-MPIO (day 1: n = 6; day 2: n = 5; day 3: n = 4; day 7: n = 4, day 21: n = 4) or αICAM-1-MPIO (day 1: n = 5; day 2: n = 5; day 3: n = 5; day 7: n = 4: day 21: n = 5) for post-contrast MRI.

5.3.6 Study II: Therapeutic efficacy of αICAM-1-MPIO To test the potential of αICAM-1-MPIO to affect lesion development, 24 mice underwent transient MCAo. Six mice died

before MRI acquisition. Repeated MRI was done at day 1 and day 3 after MCAo. At day 1, after baseline MRI, mice received an i.v. injection of saline (n = 6; equal volume as MPIO injections), IgG-MPIO (n = 5) or αICAM-1-MPIO (n = 7). Treatment allocation was randomized. Follow-up MRI was performed 2 days after injection of saline, IgG-MPIO or αICAM-1-MPIO.

5.3.7 Image analysis Brain lesions, identified by signal abnormality on T_2 maps, were outlined manually (Study I) or automatically (Study II). Based on the lesion segmentation for Study I, homologous contralesional tissue was manually outlined on T_2 maps for each animal. Perilesional tissue, i.e., the lesion borderzone, was defined by computationally expanding the lesion segmentation two times with a 3 x 3 2D kernel, with exclusion of ventricles and corpus callosum. The lesional, perilesional and contralesional segmentations were used as regions-of-interest (ROIs). To determine the amount of contrast agent accumulation within these ROIs, mean signal intensity (SI) on T_2*-weighted images was measured at 30 min after MPIO injection for each animal, and expressed as signal reduction as compared with the mean signal intensity pre-contrast agent, according to **(a)**.

(a) $SI_{(pre\text{-}CA)} - SI_{(post\text{-}CA)}$

To calculate within the ROIs the volume percentage of contrast-enhanced (CE) voxels, i.e., voxels that showed contrast-induced hypointensities, hypointense (HI) voxels with more than 2 standard deviations signal difference from pre-contrast T_2*-weighted signal intensity, according to **(b)**, were counted, and the volume of CE voxels was expressed as a percentage of total ROI volume, according to **(c)**.

(b) $SI\ (HI\ voxel) < SI_{(ROI\ pre\text{-}CA)} - 2 \cdot SD_{(ROI\ pre\text{-}CA)}$

(c) $[(volume\ of\ HI\ voxels_{(post\text{-}CA)} - volume\ of\ HI\ voxels_{(pre\text{-}CA)}) / volume\ of\ ROI] \cdot 100\ \%$

The automated lesion segmentation procedure for Study II consisted of a voxel-based supervised classification method that we have previously developed to identify stroke lesions [20]. The ipsilesional hemisphere was manually outlined on the T_2 map by a blinded observer. Hemispheric lesion fraction was calculated according to **(d)**.

(d) $volume_{(lesion)} / volume_{(ipsilesional\ hemisphere)} \cdot 100\ \%$

5.3.8 Statistical analysis Linear mixed model analysis was performed to test for effects of ROI, contrast agent, time point, and their interactions (Study I). For each ROI and time point, post-hoc tests assessed the effects of contrast agent and the pairwise difference between the two contrast agents. P-values were FDR-adjusted for multiple comparisons. $P < 0.05$ was considered significant. All statistical analyses were performed using R software [21] using nlme [22] and multcomp [23] packages. Values are presented as mean ± standard deviation, unless indicated otherwise.

5.4 RESULTS

5.4.1 Lesion development Transient MCAo induced unilateral lesions that were characterized by tissue T_2 prolongation which was particularly evident at days 1, 2 and 3 post-stroke. T_2 changes were more heterogeneous at days 7 and 21 post-stroke, and accompanied by tissue shrinkage due to necrosis. For illustration, typical examples of T_2 maps of coronal brain slices at different post-stroke time points are depicted in **Figure 5.1**.

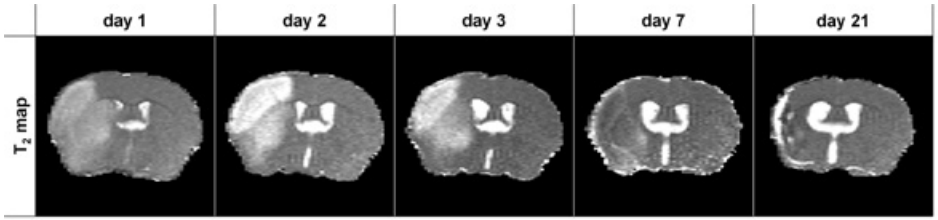

Figure 5.1
Typical examples of unilateral lesions on T_2 maps of a coronal mouse brain slice at different time points post-stroke. Lesioned tissue was characterized by T_2 prolongation at days 1, 2 and 3, which partially (pseudo)normalized at day 7 and 21 along with tissue shrinkage.

5.4.2 *In vivo* MRI of αICAM-1-MPIO binding at different time points post-stroke To test the efficacy of αICAM-1-MPIO to detect post-stroke ICAM-1 expression on brain endothelium and/or infiltrated leukocytes, cross-sectional MRI was done at 1, 2, 3, 7, or 21 days post-stroke. T_2*-weighted images were acquired before and after MPIO injection. Typical examples of pre- and post-contrast T_2*-weighted images are shown in **Figure 5.2**. In the pre-contrast T_2*-weighted images **(Figure 5.2A, C)**, relatively large hypointense regions were discernible in the ipsilesional hemisphere at 7 and 21 days post-stroke, which was not evident at post-stroke days 1, 2 and 3.

Scarce signal reductions could be seen throughout the entire brain after injection of IgG-MPIO at all time points **(Figure 5.2B)**. In contrast, substantial post-contrast hypointensities were observed after injection of αICAM-1-MPIO at day 1, day 2 and, to lesser extent, at day 3 post-stroke **(Figure 5.2D)**. These hypointensities were

largely confined to the ipsilesional hemisphere, and displayed a macroscopical pattern consistent with large cerebral vessels. Contrast enhancement was absent or minimal when αICAM-1-MPIO were injected at 7 days post-stroke. At day 21, pre-contrast hypointense regions enlarged after αICAM-1-MPIO injection, however, without an apparent vascular pattern as seen at days 1, 2 and 3.

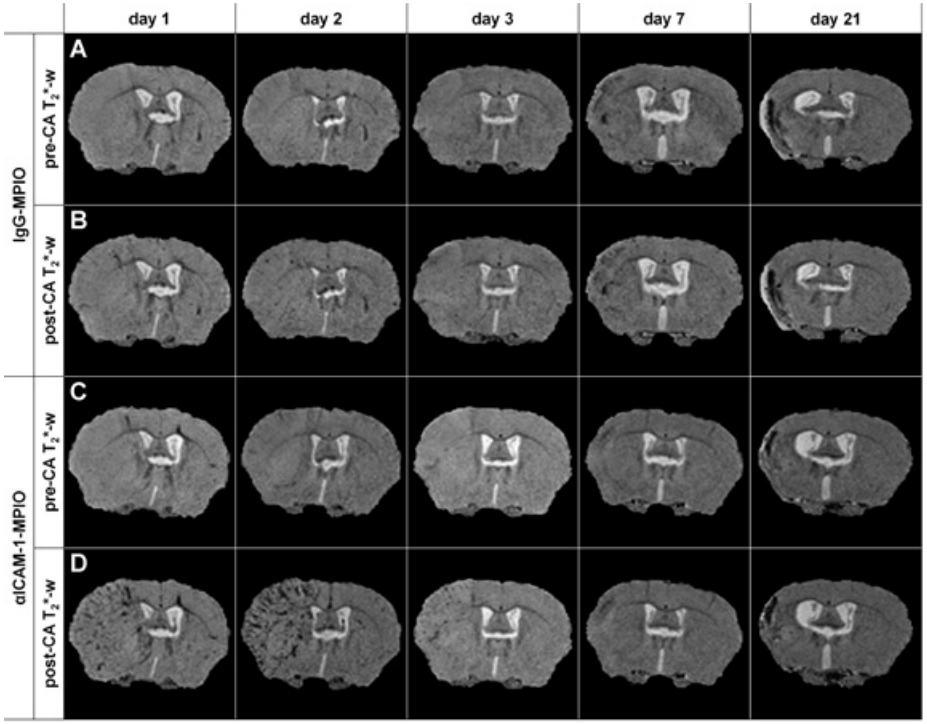

Figure 5.2

In vivo molecular MRI shows increased amount of contrast-enhanced (hypointense) pixels in the lesion territory after injection of αICAM-1-MPIO, but not IgG-MPIO, at days 1, 2 and 3 post-stroke. Ipsilesional hypointense areas on pre-contrast agent (CA) T_2*-weighted images were detectable at days 7 and 21, which did not clearly further enhance after contrast agent injection. **(A, C)** pre-CA T_2*-weighted (T_2*-w) images, and **(B, D)** post-CA T_2*-w images of a coronal brain slice of animals that received **(A, B)** IgG-MPIO or **(C, D)** αICAM-1-MPIO at 1, 2, 3, 7, or 21 days post-stroke.

For quantitative image analysis, contrast-induced T_2*-weighted signal intensity decrease and volume percentage of contrast-induced hypointensities were calculated in regions-of-interest (ROIs), i.e., lesion core, lesion borderzone and contralesional homologous tissue **(Figure 5.3A)**. T_2*-weighted signal intensity after administration

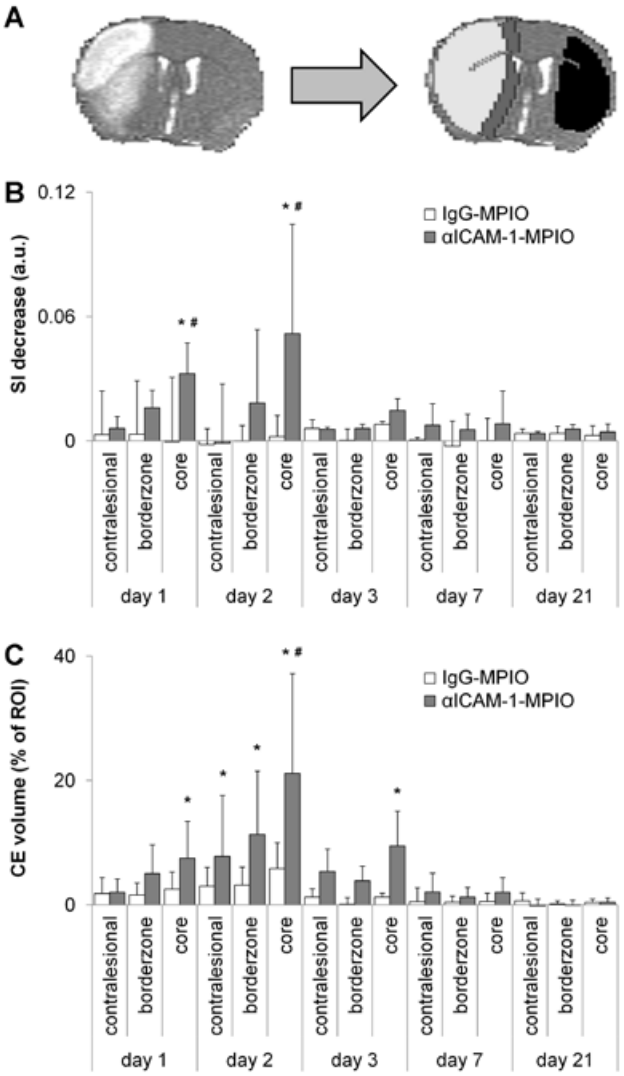

Figure 5.3

αICAM-1-MPIO induced significant T_2*-weighted signal intensity reduction and contrast-enhanced volume subacutely after stroke. **(A)** Typical example of ROI selection based on lesion identification on a T_2-map (left), shown with lesion core (light grey), lesion borderzone (dark grey) and contralesional ROI (black) as overlays (right). Bar graphs showing **(B)** absolute decrease in T_2*-weighted signal intensity (SI), and **(C)** contrast-enhanced (CE) volume, i.e., increase in amount of hypointense voxels, in contralesional, borderzone and core ROIs after injection of IgG-MPIO or αICAM-1-MPIO at different time points after stroke. Bars represent mean + SD. * $P < 0.05$ compared to pre-injection, # $P < 0.05$ compared to IgG-MPIO.

of αICAM-1-MPIO clearly decreased in the ipsilesional hemisphere at post-stroke days 1 and 2, which was statistically significant in the lesion core, as compared to post-IgG-MPIO injection. Post-contrast signal decreases were not significant at days 3, 7 and 21 post-stroke **(Figure 5.3B)**.

Significant increase in the volume percentage of hypointense voxels was observed in the lesion core at days 1, 2 and 3 post-stroke after αICAM-1-MPIO injection (7.5 ± 5.9 %; 21.1 ± 16.1 %; 9.5 ± 5.6 %, respectively). Significantly enlarged volumes of contrast enhancement were also measured in the lesion borderzone (11.3 ± 10.2 %) and contralesional tissue (7.8 ± 9.8 %) at post-stroke day 2. No significant MPIO-induced enlargement of hypointense volume was detected at day 7 or day 21 post-stroke **(Figure 5.3C)**.

5.4.3 Immunohistochemical detection of MPIO in *post mortem* brain tissue

After MRI, *post mortem* brain tissue was immunohistochemically analyzed for presence of ICAM-1, leukocytes (CD45) and MPIO. Light microscopy images of ipsilesional cortical brain tissue of mice that received αICAM-1-MPIO are shown in **Figure 5.4**. At post-stroke days 1 and 2, MPIO were abundantly present in the lesion territory, and strictly confined to ICAM-1-positive structures which displayed vascular morphology. Occasionally, co-localization of MPIO with CD45-positive leukocytes was observed. At post-stroke day 3, detected MPIO were present not only at ICAM-1-positive vasculature but also co-localized with vasculature-confined CD45-positive leukocytes. However, the amount of ICAM-1-positive vessel-like structures as well as MPIO presence were reduced at this stage compared to the earlier post-stroke phases, which is in agreement with the MRI findings. At day 7, MPIO were hardly detected within the brains of analyzed animals. At day 21, massive leukocyte infiltration was evident. ICAM-1 staining was apparent, but without a typical vascular pattern as seen at post-stroke days 1, 2, and 3. Considerable amounts of MPIO were found throughout the lesion core, associated with leukocytes. Tissue from animals that received IgG-MPIO revealed no MPIO presence (data not shown).

5.4.4 Effect of αICAM-1-MPIO on lesion development Despite effective vascular binding in the lesion territory at day 1 after stroke, as demonstrated with *in vivo* MRI and *post mortem* immunohistochemistry, αICAM-1-MPIO did not significantly influence lesion size. Animals that received αICAM-1-MPIO at day 1 displayed similar change in hemispheric lesion fraction at day 3 (-7 ± 29 %), as compared to animals that received IgG-MPIO (-1 ± 29 %) or saline (-2 ± 13 %).

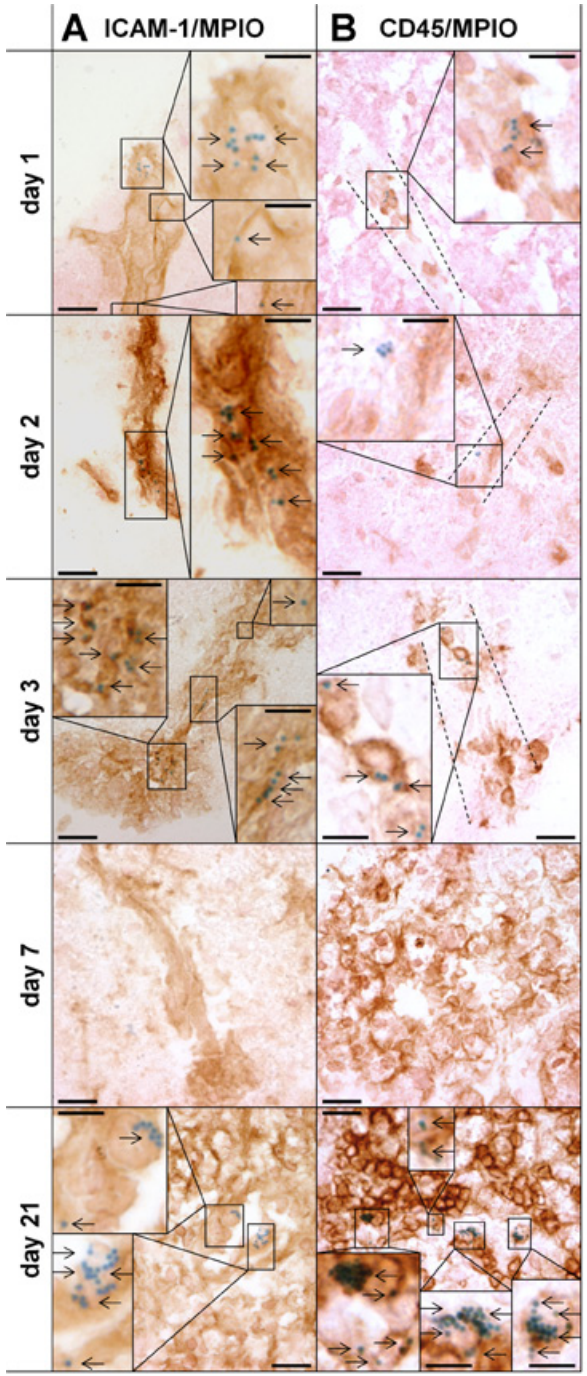

Figure 5.4
Histological sections of the sensorimotor cortex in the lesion territory reveal that αICAM-1-MPIO were confined to ICAM-1-positive vessels, and occassionally co-localize with leukocytes at post-stroke days 1, 2 and 3, but were abundantly associated with leukocytes at day 21. MPIO presence was undetectable at day 7. **(A)** ICAM-1 staining (brown) and MPIO presence (blue), and **(B)** CD45 staining (brown) and MPIO presence (blue). Arrows indicate MPIO presence. Dotted lines indicate cells with vascular morphology. Scale bars represent 25 µm in the overview images and 10 µm in the inserts.

5.5 DISCUSSION

This study aimed to determine the diagnostic potential of ICAM-1-targeted MPIO for *in vivo* MRI of vascular ICAM-1 expression and leukocyte infiltration at different stages after stroke in mice. To this end, IgG-MPIO or αICAM-1-MPIO were injected at 1, 2, 3, 7 and 21 days after transient unilateral MCA occlusion. In addition, we assessed whether αICAM-1-MPIO injection at post-stroke day 1 exerted a possible therapeutic effect by limiting post-stroke lesion development.

We showed that αICAM-1-MPIO binding was clearly detectable with *in vivo* MRI at days 1, 2 and 3 post-stroke in the lesion core, and at day 2 also in the lesion borderzone and contralesional tissue. Immunohistochemisty on *post mortem* brain tissue showed that the αICAM-1-MPIO accumulation at these subacute post-stroke stages was confined to ICAM-1-positive vessel-like structures, and occasionally co-localized with vessel-restricted leukocytes. At day 21, MRI was not able to depict the immunohistochemically detected αICAM-1-MPIO presence, which was mainly co-localized with leukocytes. IgG-MPIO were not detected in brain tissue at any time-point with MRI or immunohistochemistry. Despite effective vascular binding, no therapeutic effect of αICAM-1-MPIO compared to saline or IgG-MPIO injection was measured in this study.

Our study describes two different methods to quantify presence of contrast agent from T_2*-weighted MR images: i) contrast-induced decrease in signal intensity, and ii) increase in volume of contrast-enhanced voxels. Our analyses showed that both approaches rendered comparable results. Nevertheless, the volumetric analysis was more sensitive in detecting small differences. Ideally, a voxel-by-voxel analysis of precisely co-registered pre- and post-contrast images should be performed. However, this was unfeasible due to slight movements of the brain during MRI acquisitions.

The highest degree of αICAM-1-MPIO presence at day 2 in our study corresponds with previous histological studies that reported maximal ICAM-1 expression at this stage after transient MCAo in rodents [13, 24-26]. MPIO presence was confined to ICAM-1-positive vessels, which occasionally co-localized with leukocytes in the vascular space at post-stroke days 1, 2 and 3. We detected no signs of MPIO associated with leukocytes in the extravascular space, which suggests that αICAM-1-MPIO was only linked to blood-borne leukocytes that had not extravasated into the brain parenchyma, but retained on the luminal side of the vasculature. At 21 days after stroke, massive infiltration of leukocytes was evident in lesioned tissue. αICAM-1-MPIO were also abundantly present, but this was not distinctly detected with MRI. A likely explanation for this lack of contrast-enhancement is the strong hypointensity on T_2 maps and T_2*-weighed images before injection of contrast agent. This pre-contrast loss of MRI signal in the lesion area hampers efficient detection of subsequent (signal reducing) MPIO accumulation. The pre-contrast hypointense region corresponded with the area of massive cell infiltration as identified with immunohistochemistry. The MR signal reduction may be explained by high iron content due to phagocytosis of blood remains [27]. Similarly, in a previous study the presence of iron-containing inflammatory cells hampered the detection of engrafted superparamagnetic iron oxide (SPIO)-labeled stem cells in a photothrombotic stroke model in rats [28].

In this study, we employed staining of a general leukocyte marker (CD45) to determine co-localization of MPIO with any type of leukocyte. However, future studies should look into possible differences in ICAM-1 expression and binding between different leukocytes. Our data suggest that αICAM-1-MPIO may also be used for cellular MRI purposes, which typically involve *in vivo* or *in vitro* cellular incorporation of non-targeted contrast agent [1]. However, it should be noted that MPIO may not permanently label cells and dissociate from their target as previously reported [11, 13]. Our data also indicate that αICAM-1-MPIO does not affect lesion development in a similar way as was found with anti-ICAM-1 treatment by Zhang and co-workers [17]. For our molecular MRI study we used 5 mg iron per kg body weight to induce efficient MR contrast with αICAM-1-MPIO, which corresponded with 0.75 mg anti-ICAM-1 monoclonal antibody. Zhang and co-workers have shown that a dose of 2 mg anti-ICAM-1 monoclonal antibody per kg body weight infused 1 h after reperfusion in a rat MCA occlusion model, followed by an extra dose of 1 mg antibody per kg body weight at 22 h after reperfusion, significantly decreased lesion volume with 41 %. The lower dose and later administration of antibody in our study may explain lack of a similar therapeutic effect. Furthermore, antibodies conjugated to MPIO are presented in a multivalent way to increase target efficacy at a relatively low dose of injected particles. This is an optimal particle design for diagnostic purposes, but restricts possible therapeutic potency.

5.6 CONCLUSIONS

To conclude, this study shows that molecular MRI with αICAM-1-MPIO offers a unique approach for *in vivo* imaging of endothelial ICAM-1 expression and vascular leukocyte adhesion after experimental stroke, without significantly affecting lesion development. However, accumulation of cellular infiltrates that contain endogenous iron from blood remains

may significantly hamper the detection of exogenous iron-based contrast agents such as MPIO, particularly at chronic stages after cerebrovascular injury.

5.7 REFERENCES

1. Deddens LH, Van Tilborg GA, Mulder WJ, De Vries HE, Dijkhuizen RM (2012) Imaging neuroinflammation after stroke: current status of cel lular and molecular MRI strategies. Cerebrovasc Dis 33:392-402.
2. Cai K, Caruthers SD, Huang W, Williams TA, Zhang H, Wickline SA, Lanza GM, Winter PM (2010) MR molecular imaging of aortic angiogenesis. JACC Cardiovasc Imaging 3:824-832.
3. Te Boekhorst BC, van Tilborg GA, Strijkers GJ, Nicolay K (2012) Molecular MRI of inflammation in atherosclerosis. Curr Cardiovasc Imaging Rep 5:60-68.
4. Geelen T, Paulis LE, Coolen BF, Nicolay K, Strijkers GJ (2012) Contrast-enhanced MRI of murine myocardial infarction - part I. NMR Biomed 25:953-968.
5. Sosnovik DE, Nahrendorf M, Weissleder R (2007) Molecular magnetic resonance imaging in cardiovascular medicine. Circulation 115:2076-2086.
6. Bogdanov A, Jr., Mazzanti ML (2011) Molecular magnetic resonance con trast agents for the detection of cancer: past and present. Semin Oncol 38:42-54.
7. Barber PA, Foniok T, Kirk D, Buchan AM, Laurent S, Boutry S, Muller RN, Hoyte L, Tomanek B, Tuor UI (2004) MR molecular imaging of early endo thelial activation in focal ischemia. Ann Neurol 56:116-120.
8. Hoyte LC, Brooks KJ, Nagel S, AkhtarA, Chen R, Mardiguian S, McAteer MA, Anthony DC, Choudhury RP, Buchan AM, Sibson NR (2010) Molecular magnetic resonance imaging of acute vascular cell adhesion molecule-1 expression in a mouse model of cerebral ischemia. J Cereb Blood Flow Metab 30: 1178-1187.
9. McAteer MA, Sibson NR, von Zur Muhlen C, Schneider JE, Lowe AS, Warrick N, Channon KM, Anthony DC, Choudhury RP (2007) *In vivo* magnetic resonance imaging of acut e brain inflammation using microparticles of iron oxide. Nat Med 13:1253-1258.
10. Van Kasteren SI, Campbell SJ, Serres S, Anthony DC, Sibson NR, Davis BG (2009) Glyconanoparticles allow pre-symptomatic *in vivo* imaging of brain disease. Proc Natl Acad Sci U S A 106:18-23.
11. Montagne A, Gauberti M, Macrez R, Jullienne A, Briens A, Raynaud JS, Louin G, Buisson A, Haelewyn B, Docagne F, Defer G, Vivien D, Maubert E (2012) Ultra-sensitive molecular MRI of cerebrovascular cell activation enables early detection of chronic central nervous system disorders. Neuroimage 63:760-770.
12. Sibson NR, Blamire AM, Bernades-Silva M, Laurent S, Boutry S, Muller RN, Styles P, Anthony DC (2004) MRI detection of early endothelial activation in brain inflammation. Magn Reson Med 51:248-252.
13. Deddens LH, Van Tilborg GA, Van der Toorn A, Paulis LE, Strijkers GJ, Storm G, Mulder WJ, De Vries HE, Dijkhuizen RM (2012) Micron-sized particles of iron oxide and gadolinium-containing liposomes as targeted contrast agent for molecular MRI of neuroinflammation after stroke: A comparative study. Proceedings International Society for Magnetic Resonance in Medicine 20: 1627P.
14. Van de Stolpe A, Van der Saag PT (1996) Intercellular adhesion molecule-1. J Mol Med (Berl) 74:13-33.
15. Iadecola C, Anrather J (2011) The immunology of stroke: from mechanisms to translation. Nat Med 17:796-808.
16. Frijns CJ, Kappelle LJ (2002) Inflammatory cell adhesion molecules in ischemic cerebrovascular disease. Stroke 33:2115-2122.
17. Zhang RL, Chopp M, Li Y, Zaloga C, Jiang N, Jones ML, Miyasaka M, Ward PA (1994) Anti-ICAM-1 antibody reduces ischemic cell damage after transient middle cerebral artery occlusion in the rat. Neurology 44:1747-1751.
18. Enlimomab Acute Stroke Trial Investigators (2001) Use of anti-ICAM-1 therapy in ischemic stroke: results of the Enlimomab Acute Stroke Trial. Neurology 57:1428-1434.
19. Hata R, Mies G, Wiessner C, Fritze K, Hesselbarth D, Brinker G, Hossmann KA (1998) A reproducible model of middle cerebral artery occlusion in mice: hemodynamic, biochemical, and magnetic resonance imaging. J Cereb Blood Flow Metab 18:367-375.
20. Bouts MJ, Tiebosch IA, Zwartbol R, Hoogveld E, Wu O, Dijkhuizen RM (2011) Early prediction of salvageable tissue with multiparametric MRI-based algorithms after experimental ischemic stroke. Proceedings International Society for Magnetic Resonance in Medicine 19: 2141P.

21. R development core team (2009) {R: A language and environment for statistical computing}. R Foundation for Statistical Computing, Vienna, Austria.

22. Pinheiro J, Bates D, DebRoy S, Sarkar D, R development core team (2011) nlme: Linear and nonlinear mixed effects models. (R package version 3.1-102) [Computer program].

23. Hothorn T, Bretz F, Westfall P (2008) Simultaneous inference in general parametric models. Biom J 50:346-363.

24. Yu Q, Chu M, Wang H, Lu S, Gao H, Li P, Gan Y, Shi H, Liang W, Chen J, Gao Y (2011) Sevoflurane preconditioning protects blood-brain-barrier against brain ischemia. Front Biosci (Elite Ed) 3:978-988.

25. Zhang RL, Chopp M, Zaloga C, Zhang ZG, Jiang N, Gautam SC, Tang WX, Tsang W, Anderson DC, Manning AM (1995) The temporal profiles of ICAM-1 protein and mRNA expression after transient MCA occlusion in the rat. Brain Res 682:182-188.

26. Vemuganti R, Dempsey RJ, Bowen KK (2004) Inhibition of intercellular adhesion molecule-1 protein expression by antisense oligonucleotides is neuroprotective after transient middle cerebral artery occlusion in rat. Stroke 35:179-184.

27. Weber R, Wegener S, Ramos-Cabrer P, Wiedermann D, Hoehn M (2005) MRI detection of macrophage activity after experimental stroke in rats: new indicators for late appearance of vascular degradation? Magn Reson Med 54:59-66.

28. Vandeputte C, Thomas D, Dresselaers T, Crabbe A, Verfaillie C, Baekelandt V, Van Laere K, Himmelreich U (2011) Characterization of the inflammatory response in a photothrombotic stroke model by MRI: implications for stem cell transplantation. Mol Imaging Biol 13:663-671.

MOLECULAR MRI OF ICAM-1 EXPRESSION IN AN ANIMAL MODEL OF MULTIPLE SCLEROSIS

Based on:
Erwin L.A. Blezer, Lisette H. Deddens, Gijs Kooij, Joost Drexhage, Susanne M.A. van der Pol, Arie Reijerkerk, Rick M. Dijkhuizen and Helga E. de Vries.
In vivo MR imaging of intercellular adhesion molecule-1 expression in an animal model of multiple sclerosis
(in preparation)

06

6.1 ABSTRACT

The upregulation of intercellular adhesion molecule 1 (ICAM-1) is an early event during lesion formation in multiple sclerosis (MS) and in experimental autoimmune encephalomyelitis (EAE), a validated animal model of MS. Its expression may serve as a biomarker predicting upcoming disease activity. The objective of this study was therefore to explore if ICAM-1 can be visualized in the course of EAE with *in vivo* magnetic resonance imaging (MRI) using micron-sized particles of iron oxides (MPIO). To this end, αICAM-1-MPIO or control IgG-MPIO were injected at the peak of EAE (14 ± 1 days post-immunization; acute phase) and chronic phase of EAE (26 ± 1 days post-immunization). The permeability of the blood-brain barrier (BBB) was examined using gadobutrol-enhanced MRI. In parallel, cerebellar microvessels were isolated from animals with EAE at different time point and were analyzed for the gene transcripts of ICAM-1 by means of quantitive PCR (qPCR). Brain sections were also immunohistochemically (IHC) analyzed for ICAM-1 expression and the presence of iron particles (Prussian Blue). qPCR and IHC analyses showed that ICAM-1 was abundantly expressed in animals that manifested EAE. Animals injected with αICAM-1-MPIO revealed T_2*-weighted MR hypointensities throughout the brain at 40 minutes after injection. Hypointense pixels were particularly detected in the subarachnoid space between the temporal lobe and the midbrain. Quantitatively, no significant differences in any of the ROIs between the acute and chronic phases of disease could be observed. ICAM-1 upregulation was not necessarily associated with the physical disruption of the BBB. IHC analyses indicated that αICAM-1-MPIO were associated with ICAM-1-positive endothelial cells. This study shows that ICAM-1 expression can be visualized *in vivo* during the progression of EAE, indicating its suitability as a new contrast agent to detect ongoing disease activity and the evaluation of treatment efficacy.

6.2 INTRODUCTION

Multiple sclerosis (MS) is a chronic inflammatory disease of the central nervous system (CNS) characterized by leukocyte infiltrates, leading to demyelination and axonal damage [1-2]. In this process, immune activation of the brain endothelial lining, evidenced by the enhanced expression of cell adhesion molecules such as vascular cell adhesion molecule-1 (VCAM-1) and intercellular cell adhesion molecule-1 (ICAM-1), is a key event [3]. Imaging strategies that enable the *in vivo* detection of these markers, known to precede leukocyte diapedesis, would greatly enhance our understanding of the onset of MS and may provide specific biomarkers for new relapses. Moreover, visualization of a lowered expression may become a novel way to test the efficacy of treatments that are aimed to dampen leukocyte infiltration [4].

Magnetic resonance imaging (MRI) has become the established diagnostic imaging tool in MS. It usually entails the acquisition of T_2-weighted MRI, fluid attenuated inversion recovery (FLAIR) MRI, and gadolinium-based contrast-enhanced MRI to visualize ongoing inflammation. These MR techniques mainly visualize the consequences of leukocyte influx and the resulting inflammatory process, i.e., edema formation, loss of tight junction integrity or myelin destruction. However, ideally, one would like to have techniques available that measure earlier stages of lesion formation, such as early activation of endothelial cells, to provide primary markers for leukocyte influx.

Recently, cellular and molecular MRI have emerged as tools to provide the means to visualize pathogenic processes at the cellular and molecular level. These techniques directly visualize biological entities using targeted probes containing MR contrast agents [5]. These MR modalities have been used to study events involved in the influx of leukocytes, such as the macrophage influx into the CNS with superparamagnetic particles of iron oxide (SPIO), which has been successfully shown in animals with EAE [6-7], as well as in patients with MS [8]. However this is a relative late event in the overall inflammatory process which is preceded by endothelial activation.

Micron-sized particles of iron oxide (MPIO) have been put forward as probes for the detection of inflammatory endothelial markers in the brain [9-10]. The iron oxide core of these large particles (micrometer range) induces strong MR contrast-enhancing effects that allow sensitive detection at relatively low doses. Furthermore, blood clearance is in the order of minutes [11] and any undesirable, non-specific blood pool contrast effect of MPIO is negligible when scans are made after 30-60 min. Finally, the large size of MPIO (~ microns), limits passive leakage over a damaged BBB, a phenomenon which warrants the usage of smaller agents like gadolinium chelates (~ nanometers) or SPIO (tens of nanometers) to study BBB permeability in EAE [6]. Using this approach, VCAM-1 expression has recently been visualized *in vivo* in EAE with VCAM-1-targeted MPIO [12-13].

ICAM-1 is another interesting target for molecular MRI of EAE-induced neurovascular inflammation. Like VCAM-1, ICAM-1 expression levels are increased during early lesion formation both in EAE [14-15] and in MS [16]. Both adhesion molecules are important for the transmigration of leukocytes over the BBB, but there are also

differences. Both are involved in the process of the firm adhesion of T-cells, but ICAM-1 unlike VCAM-1, can mediate the crawling of T-cells against the direction of blood flow to sites of diapedesis. Furthermore, ICAM-1 has been associated with T-cell, and VCAM-1 with macrophage diapedesis across the endothelium [17]. The significance of ICAM-1 in the development of EAE has been shown in ICAM-1-deficient mice [18], and in treatment studies targeted to block ICAM-1 functionality in which the development of EAE is ameliorated [19]. This central role of ICAM-1 in EAE development warrants its position as an important imaging target.

The aim of this study was to determine the potential of MRI to detect expression of ICAM-1 over time in a mouse model of MS using antibody-conjugated MPIO directed to ICAM-1 which have also been used to explore ICAM-1 expression after stroke [10] and radiation-induced brain injury [20]. Our study shows that ICAM-1 expression can be visualized with *in vivo* MRI during the progression of EAE, and that antibody-conjugated MPIO mainly target endothelial cells.

6.3 MATERIALS AND METHODS

6.3.1 Materials ProMag™ 1 Series, Bind-IT™ MPIO (25 mg MPIO/ml, 26.5 % iron-content, 1 µm) were obtained from Bangs Laboratories, Inc. (Fisher`s, IN, USA). Diaminobenzidine solution (DAB+) was obtained from Sigma-Aldrich (St. Louis, MO, USA). A monoclonal antibody against mouse ICAM-1 (αICAM-1, YN1/1.7.4) and irrelevant immunoglobulin G antibody (IgG, RTK4530) were obtained from BioLegend (San Diego, CA, USA). Goat anti-rat IgG (H+L) was obtained from Jackson Immuno Research (Suffolk, UK). Rat anti-mouse CD31 (clone MEC13.3) was obtained from BD Pharmingen (Breda, The Netherlands). A monoclonal antibody against mouse CD31 (αCD31) was produced from hybridoma ER-MP12. Horseradish peroxidase-labeled streptavidin (HRPstrep) was obtained from DAKO (Glostrup, Denmark). Primers were obtained from Ocimum Biosolutions (IJsselstein, The Netherlands). M199 was obtained from Gibco/Life Technologies (Breda, The Netherlands), Fetal Calf Serum (FSC) was obtained from Lonza (Breda, The Netherlands), and Blendzyme II Liberase TM and Bovine Serum Albumine (BSA) from Roche (Woerden, The Netherlands). MOG_{35-55} peptide (MEVG-W-YRSPFSR-V-V-HLYRNGK-amide) was obtained from Cambridge Research Biochemicals (Billingham, UK). Mycobacterium tuberculosis H37Ra as well as Complete Freund's Adjuvant (CFA) were obtained from BD Difco (Alphen aan de Rijn, The Netherlands). Pertussis toxin and dextran were obtained from Sigma-Aldrich (Zwijndrecht, The Netherlands). Euthesate was obtained from Apharmo BV (Arnhem, The Netherlands).

6.3.2 Preparation of antibody-functionalized MPIO MPIO were extracted from their original buffer by magnetic separation, and resuspended in coupling buffer (50 mM 2-(N-morpholino)ethanesulfonic acid (MES); pH 5.2). Prior to the coupling procedure, αICAM-1 or IgG were buffer-exchanged to coupling buffer by centrifugation, resulting in a final antibody concentration of 1.0 mg/ml. Next, MPIO and αICAM-1 or IgG were added in a 1:1 (v/v) ratio, vortexed and left to incubate for 60 min at room temperature on a roller-bench. Following incubation, antibody-MPIO were buffer-exchanged to storage solution (150 mM NaCl with 0.002 % azide) by magnetic separation and stored at 4 °C.

6.3.3 EAE model All animal procedures were approved by the local (Amsterdam/Utrecht) ethical committee on animal experiments, and experiments were performed in accordance with the guidelines of the European Communities council directive. Female 10-weeks-old C57BL/6J mice were obtained from Harlan (Boxmeer, The Netherlands). All mice were kept under pathogen-free conditions. EAE was induced by subcutaneous inoculation of 100 µg MOG_{35-55} peptide in each flank, in an equal volume of CFA containing 3 mg/ml of heat-killed M. tuberculosis, as described before [21]. Mice were subsequently intraperitoneally (i.p.) injected with 200 µl (200 ng) of pertussis toxin, which was repeated 2 days post-immunization (p.i.). Control mice, used for the determination of ICAM-1 mRNA levels on cerebellar capillaries, were immunized with CFA only. All mice were examined daily for clinical signs of EAE and were scored as follows: 0, no disease; 1, limp tail; 2, hind limb weakness; 3, complete hind limb paralysis; 4, hind limb paralysis plus front limb paralysis; and 5, moribund or dead. The model is characterized by three phases. Typically EAE onset is around 9 days after immunization, with peak of disease around 14-15 days p.i., followed by partial recovery of disease. A total of 4 controls and 8 EAE animals were used for determination of mRNA levels of ICAM-1 in cerebellar capillaries. 13 animals were used for the MRI experiments.

6.3.4 Determination of ICAM-1 mRNA levels on isolated brain endothelial cell
Cerebellums were harvested at 9 (before the first clinical signs of EAE: "before") and 15 days p.i. (height of the acute phase of EAE: "acute"). 2 controls and 4 animals with EAE were used for both time points. Cerebellums were homogenized in M199 containing 0.2 % FCS using a pair of tight and loose pestles. Cells and capillaries

were pelleted at 2000 rpm for 10 min at 4 ˚C in a swinging bucket rotor. The pellet was resuspended in 15 % dextran in M199 and centrifuged at 2500 rpm for 25 min at 4 ˚C in a swinging bucket rotor. Subsequently, the microvessel pellet was resuspended in M199, enzymatically dissociated with Blendzyme II Liberase TM for 30 minutes at 37 ˚C and finally washed with M199. Each panning plate (10 cm petri dish) was first coated with 10 ml of 50 mM Tris/HCl pH 9.5 containing 30 µl of goat anti-rat IgG (H+L), at 4 ˚C overnight. Next, the plates were washed with PBS, blocked with 0.2 % BSA and incubated for at least 2 hours at room temperature with 10 ml of 0.2 % BSA containing 40 µl of rat anti-mouse CD31 (clone MEC13.3). Finally, the plates were washed with PBS and endothelial cells were bound for 60 min at room temperature. After washing with PBS (8x), mRNA of panned endothelial cells was harvested. Endothelial cells were lysed using 1 ml of Trizol and stored at -80 ˚C. Quantitive PCR (qPCR) was used to determine the expression of ICAM-1 and CD31. Equal amounts of RNA were converted into cDNA and analyzed for mRNA presence according to the manufacturer's protocol (Applied Biosystems, Bleiswijk, The Netherlands). The Cycle threshold values were used to calculate the relative fold difference in mRNA levels. All experiments were performed using experimental duplicates. Expression levels of ICAM-1 are expressed relative to CD31.

6.3.5 Experimental design MRI Animals were examined with MRI during two characteristic phases of disease, i.e., when animal displayed maximal neurological deficits at the acute phase of EAE (14 ± 1 days p.i.), and at the chronic phase of EAE (26 ± 1 days p.i.: "chronic"). Animals were either injected with αICAM-1- or IgG-MPIO (5 mg iron/kg). Respectively 5 and 3 animals received αICAM-1- or IgG-MPIO during the acute phase of EAE. For the chronic phase this was respectively 3 and 2 animals. All animals were sacrificed at the end of the MR experiment by an i.p. injection with an overdose of pentobarbital (Euthesate) to harvest tissue for immunohistochemistry (IHC). One brain hemisphere and parts of the spleen were snap-frozen with liquid N_2 and stored at -80 ˚C (the other brain hemisphere was used for another study). The spleen was exclusively tested for MPIO presence to verify proper delivery of MPIO into animals.

6.3.6 MRI protocol MR experiments were performed on a 9.4 T horizontal 20 cm bore MR system (Varian Inc., Palo Alto, CA, USA). For *in vivo* experiments, mice were anesthetized with isoflurane (3.5 % induction, 1.5-2.0 % maintenance) in air/O_2 (2:1) or pure O_2 (to reduce intrinsic magnetic susceptibility effects from deoxygenated blood during T_2*-weighted acquisitions). The tail vein was cannulated and connected with a polythene tube (inner Ø 0.28 mm, volume approximately 100-150 µl; Smiths Industries, Kent, UK) for contrast agent delivery during MRI. Animals were positioned in a specially designed cradle and inserted into the magnet. A birdcage volume coil (Ø 70 mm) and an inductively-coupled homebuilt surface coil (Ø 30 mm) were used for radiofrequency transmission and signal detection, respectively. The MR protocol consisted of 3 phases, i.e., a pre-contrast agent phase, a post-MPIO phase, and a post-gadolinium (gadobutrol) contrast agent phase. During the first phase, volume locations for 2D/3D MRI were determined from a transversal scout image. The central position of this volume was positioned directly caudal to the cerebellum. The volume included the upper part of the spinal cord, the cerebellum and the caudal part of the cerebrum. Two subsets of T_2*-weighted images (3D multi gradient echo; TR/TE = 37/(5, 10, 15 and 20) ms; number of acquisitions (NA) = 4; flip angle 10˚; 150 x 150 x 150 μm^3 voxel size; acquisition time = ~ 20 min per set) were acquired. These two subsets were averaged and were designated as the pre-MPIO 3D image. MPIO-conjugates were injected at the end of this part of the protocol. In the post-MPIO injection phase, three subsets of the T_2*-weighted 3D images were collected. The first and second 3D post-MPIO image were averaged (total acquisition time = ~ 40 min), and designated as the post-MPIO 3D image. At the end of this part of the protocol, 2D T_1-weighted images were acquired (gradient echo; TR/TE = 1600/4 ms, 100 x 200 μm^2 in-plane resolution, 43 slices of 450 µm, NA = 4, experimental time = ~ 5 min) and gadobutrol (0.3 mM/kg Gd-DO3A-butriol (Gadovist®)) was injected to investigate BBB integrity. In the post-gadobutrol phase, two additional sets of 2D T_1-weighted images were acquired. The center of k-space was acquired respectively 2.5 and 7.5 minutes after gadobutrol injection. The last T_1-weighted image set was used to measure the extent of BBB permeability.

6.3.7 Immunohistochemistry For IHC, cryosections of 10 µm of brain tissue were air-dried overnight, and acetone-fixated for 10 min. Dry, fixed sections were hydrated for 15 min in PBS containing 0.1 % BSA. Next, sections were incubated with biotinylated αICAM-1 (10 µg antibody/ml) in PBS/0.1 % BSA for 1 h. Subsequently, sections were incubated for 45 min with horseradish peroxidase-labeled streptavidin (HRPstrep, prepared according to the manufacturer's description). Diaminobenzidine solution (DAB) was used as chromogen (used according to the manufacturer's description). Between incubation steps, sections were thoroughly washed with PBS. Tissue was subsequently incubated with Perls' solution (2 N HCl and 2 % ferrocyanide in Milli-Q in 1:1 (v/v) ratio) for 20 min, thoroughly washed with Milli-Q, dipped in a nuclear fast red solution, dehydrated and slides were mounted in Entallan. All steps were performed at room temperature.

6.3.8 MRI analysis MPIO and gadobutrol presence were quantified on the 3D images (MPIO) or 2D T_1-weighted images (gadobutrol). Signal inhomogeneity as a result of surface coil-based detection was corrected using a non-parametric non-uniform intensity normalization procedure. Images acquired at different echo times of the multi echo 3D protocol were combined to increase signal-to-noise ratio. These images were further used in the image analyses pipeline. The averaged 3D image sets acquired in the pre-contrast MR phase were designated as reference image for registration procedures and delineation of regions-of-interest (ROIs). All 2D/3D MR images were rigidly registered to this reference image by maximizing mutual information using Elastix [22]. All subsequent analyses were performed on these registered images. The change in signal intensity as a result of MR contrast agent was calculated by subtracting averaged post-MPIO 3D images from pre-MPIO 3D images, and subtracting pre-gadobutrol 2D T_1-weighted images from post-gadobutrol images. Difference images were only used for qualitative evaluations, as breathing-induced movement occasionally induced voxel-level shifts, especially in the caudal part of the brain. The effect of MPIO/gadobutrol presence on the signal intensity of the MR images was therefore quantified by calculating the percentage of pixels with abnormal pixel intensities in well-defined ROIs (see below for the definition). For each of these ROIs a threshold was determined in the pre-contrast images which was defined as the mean signal intensity minus (MPIO) or plus (gadobutrol) two times the standard deviation of the signal intensity in that area. Pixels in the post-contrast images with intensities below (MPIO) or above (gadobutrol) these thresholds were considered abnormal. The specific ROIs were manually outlined on the 3D reference image using well-defined hallmarks. These ROIs were (see also Figure 6.1):

- Cerebellum: All cerebellar areas starting 12 slices before to 6 slices after the slice with the first caudal to rostral appearing maximum-sized 4th ventricle.
- Brain stem: All brain stem areas in the same volume as above.
- Subarachnoid space: all subarachnoid space between the temporal cortex and the midbrain starting 6 slices before and ending maximally 18 slices after the slice with the first caudal to rostral appearing white matter in the cerebrum.
- Ventricular area: Ventricular area starting 3 slices before to 3 slices after the first caudal to rostral appearance of the conjunction of the lateral and third ventricle. The choroid plexus is located in this area.

ROIs were drawn on every 3rd image in the defined volumes described above. The rationale to choose these areas was the qualitatively assessed presence of MPIO on the 3D images, combined with the knowledge that these brain regions are prone to develop abnormalities in this model [23]. The ventricular area was chosen to visualize contrast leakage through the choroid plexus.

Owing to technical complications (death of an animal during experiment; no administration of MPIO/gadobutrol) some animals had to be excluded from further MRI analysis. Furthermore, individual MR experiments were blindly evaluated on the presence of breathing-induced movement artifacts, which could adversely affect the level of detection thresholds for the analyzed ROI. Especially caudal areas were prone to movement artifacts. Experiments with these abnormalities were also excluded for further analyses. This resulted in the following final numbers of αICAM-1/IgG-MPIO-injected animals: 4/2 (acute phase) and 3/1 (chronic phase) for the cerebellum and brain stem and 5/2 (acute phase) and 3/2 (chronic phase) for the subarachnoid space and ventricular area.

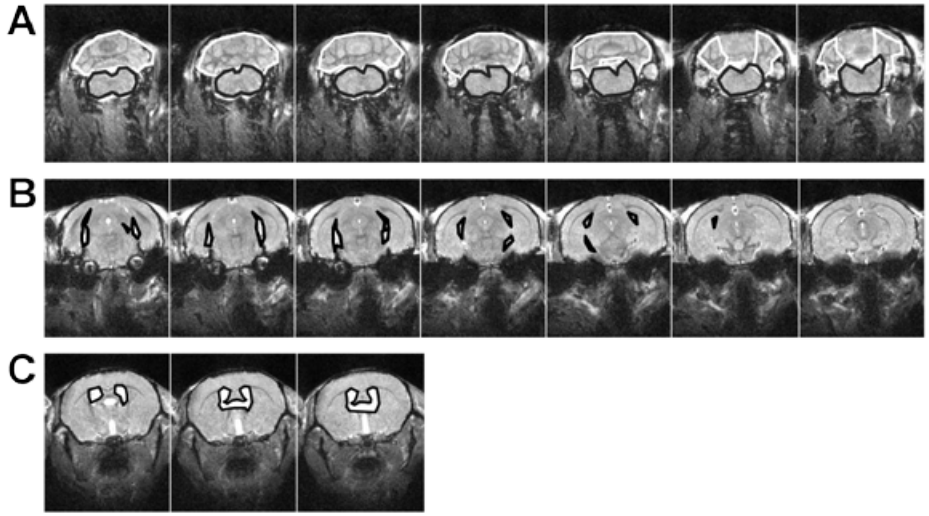

Figure 6.1

Typical example of region of interest (ROI) selection overlayed on a T_2*-weighted image, with **(A)** cerebellum (white) and brain stem (black), **(B)** subarachnoid space (black), and **(C)** ventricular area (black).

6.3.9 Statistical analysis Statistical analyses were performed using the statistical software package SigmaPlot (version 11 Germany). Analyses were performed to evaluate if:

- there was a change in mRNA ICAM-1 expression in the cerebral capillaries of animals with EAE during the different phases of EAE. Data were evaluated by a

one way analysis of variance (ANOVA) for possible significant differences.
- there was a change in abnormal pixels count as a result of the presence of MR contrast agents (MPIO: αICAM-1/IgG; gadobutrol) in the ROIs during the different phases of EAE. Data were evaluated for significant differences by two-way ANOVA) for repeated measures. Factors were: type of contrast agent, abnormal pixels in pre-/post-MR image, and ROIs.
- there was a difference between abnormal pixels count as a result of the presence of MR contrast agents in the ROIs during the different phases of EAE. Data were evaluated for significant differences by two-way ANOVA. Factors were: type of contrast agent, abnormal pixels in pre/post MR image, ROIs and phase of EAE.

When passing the ANOVA tests, data were tested using the Student–Newman–Keuls post-hoc test. $P < 0.05$ was considered to be statistically significant. If not otherwise stated, data are presented as mean ± standard deviation.

6.4 RESULTS

6.4.1 Clinical scores, weight and ICAM-1 expression during EAE progression The time courses of the development of neurological score and body weight are plotted in **Figure 6.2A**. First neurological deficits (partially reduced tail tone; score 0.5) were detected 7 days after immunization. The average EAE scores for animals measured at the acute phase was 2.83 ± 1.03, and 1.20 ± 1.78 for the chronic phase. On average, weight loss preceded neurological scores by one to two days. Quantitative PCR analyses showed that ICAM-1 mRNA expression levels on brain capillaries were significantly increased in the acute phase of EAE **(Figure 6.2B)** compared to the onset of disease and compared to control animals. IHC data showed that ICAM-1 was clearly present throughout the brain, particularly in subarachnoid and periventricular spaces, both in the acute and chronic phases of EAE **(Figure 6.2C)**.

6.4.2 Qualitative *in vivo* MRI assessment shows αICAM-1-MPIO presence in mice with EAE Irrespective of the phase of EAE, all animals injected with αICAM-1-MPIO showed abnormal hypointensities 40 minutes after injection of MPIO. Typical examples of images from animals that received αICAM-1- or IgG-MPIO at the acute phase of EAE are shown in **Figure 6.3A** and **B**, respectively. Predominantly, hypointensities were detected in cerebellum, the subarachnoid space between the temporal cortex and the midbrain, caudate putamen and cortical areas in the cerebrum. Specifically, the latter two areas showed bands of MR hypointensities suggestive of vascular ICAM-1 presence. Occasionally, ventricular areas showed bead-like hypointensities within the cerebrospinal fluid **(inset Figure 6.3A)**. These observations were confirmed in the αICAM-1-MPIO difference images. Comparable patterns of MPIO abnormalities were not observed in animals injected with IgG-MPIO.

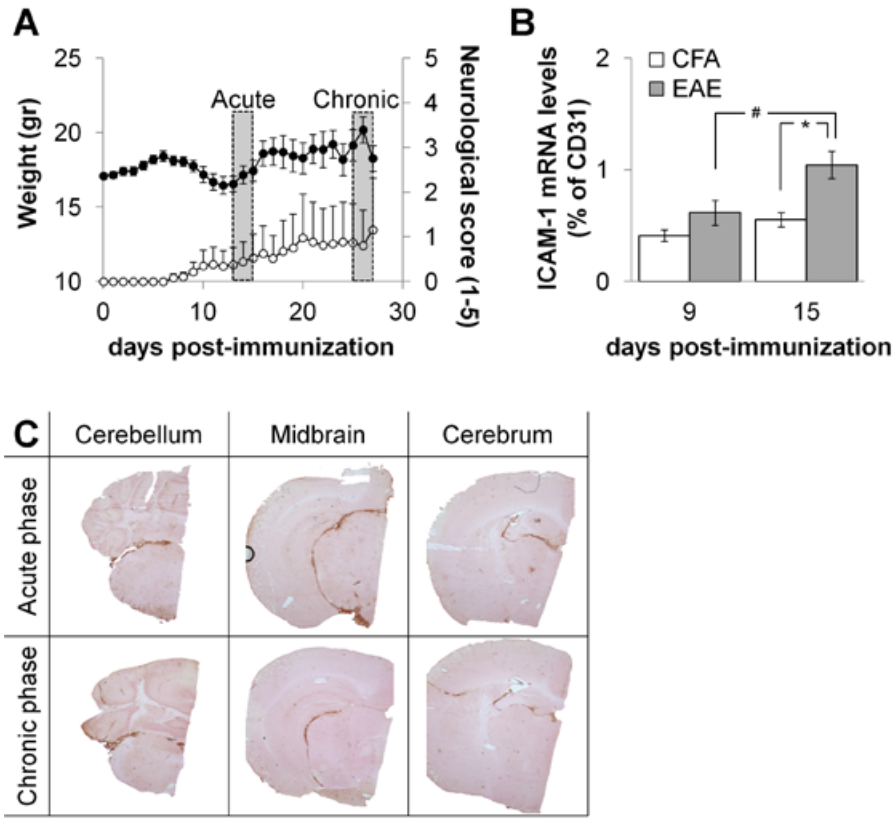

Figure 6.2
Neurological score, weight and ICAM-1 expression during progression of EAE. **(A)** Neurological score (○) and body weight (●) of animals with EAE. Animals were immunized with MOG_{35-55} peptide at day 0. The time periods of injection of MPIO conjugates at the different phases of EAE is indicated with grey bars. Data are presented as mean ± SEM. **(B)** mRNA expression levels of ICAM-1 in isolated brain endothelial cells from CFA-control and EAE mice. Expression levels of ICAM-1 are relative to CD31, which is used as a marker for brain endothelial cells, at two different time points (day 9: before onset EAE; day 15: acute phase of EAE). * $P < 0.05$ versus CFA; # $P < 0.05$ versus acute phase of disease. **(C)** IHC showing presence of ICAM-1 at different phases of EAE. Sections through the cerebellum, midbrain and cerebrum are shown. ICAM-1 (brown) is clearly present in particularly the subarachnoid and periventricular spaces, both in the acute (upper row) as in the chronic (lower row) phase of EAE.

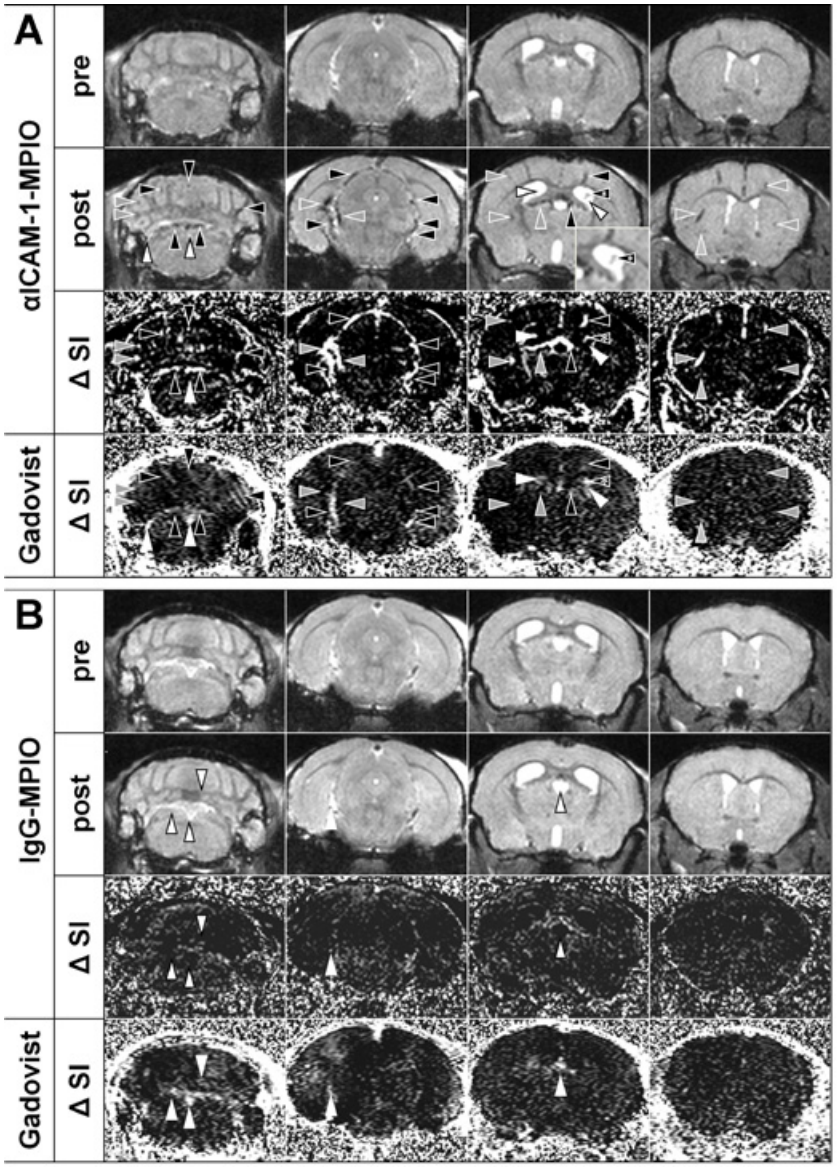

Figure 6.3

Typical examples of MR images of animals injected with **(A)** αICAM-1-MPIO (neurological score 3) and **(B)** IgG-MPIO (neurological score 3.5) at the acute phase of disease. The animal that received αICAM-1-MPIO **(A)** was characterized by focal hypointensities (black/grey arrow heads) throughout the brain, which was confirmed on the MPIO difference images. MPIO hypointensities were not necessarily associated with gadobutrol leakage (grey arrowheads), as shown on the gadobutrol difference image. Ventricular areas could be positive for gadobutrol leakage, but negative for MPIO presence (white arrow heads), although small bead-like hypointensities could be observed within the ventricular liquor (black arrowhead with asterisk). The inset on the post-αICAM-1-MPIO image shows a magnification of this area. No specific MPIO presence was observed after IgG-MPIO administration **(B)** although gadobutrol leakage (white arrow heads) could be observed. Similar observations were observed for animals injected with MPIO during the chronic phase of EAE. (pre: 3D multi gradient echo T_2*-weighted image before injection of MR contrast; post: after injection of MR contrast; Δ SI: difference in signal intensity as a result of MPIO/gadobutrol presence; ► : MPIO positive/gadobutrol positive; ►: MPIO positive/gadobutrol negative; ▷MPIO negative/gadobutrol positive).

Gadobutrol was injected to measure the BBB integrity. Compared to αICAM-1-MPIO presence, gadobutrol leakage was less outspoken on the T_1-weighted difference images. MPIO accumulation was not necessarily accompanied by gadobutrol leakage. Frequently, areas that showed definite αICAM-1-MPIO presence did not show leakage of gadobutrol (grey arrowheads in **Figure 6.3**). The vice-versa effect was less obvious; with the exception of ventricular tissue, there were no clear areas which were positive for gadobutrol leakage and negative for αICAM-1-MPIO presence.

6.4.3 Quantification of MR abnormalities detected with contrast agents The results of the quantitative MRI analyses are shown in **Figure 6.4**. Only the amount of pixels with abnormal signal intensity decrease on the post-contrast (MPIO/gadobutrol) images is displayed.

Theoretically, for a Gaussian distribution of pixel-intensities, approximately 2.5 % of the pixels may be considered abnormal in the pre-MPIO images. In this study this value (averaged for all animals) ranged from 0.79 ± 0.63 % (subarachnoid space) to 2.99 ± 1.19 % (ventricular area). After IgG-MPIO injection, the amount of abnormal pixels did not significantly increase in any of the ROIs for both phases of disease. Animals receiving αICAM-1-MPIO, however, showed a significant increase of abnormal pixels in the subarachnoid space between the temporal cortex and the midbrain for both phases of disease. All other ROIs did not show significant differences. Post-αICAM-1-MPIO abnormal pixel levels were also significantly different from post-IgG-MPIO levels in the subarachnoid space for both phases of EAE. There were no significant differences between the different phases of EAE **(Figure 6.4A)**.

The number of pixels with abnormal signal intensity increase after gadobutrol injection was also calculated **(Figure 6.4B)**. Gadobutrol was injected after MPIO

injection. Pre-injection percentage of abnormal pixels (averaged for all values) ranged between 0.79 ± 0.43 % (cerebellum) and 2.07 ± 0.69 % (ventricular area). Significant differences between pre- and post-gadobutrol levels were observed in the subarachnoid space during the acute phase of EAE for the IgG-MPIO injected animals and in all ventricular areas for all groups. In the subarachnoid space, the level of abnormal pixels after gadobutrol injection during the acute phase of disease was significantly higher in the IgG-MPIO-injected animals compared to the αICAM-1-MPIO group, and compared to levels during the chronic phase of disease.

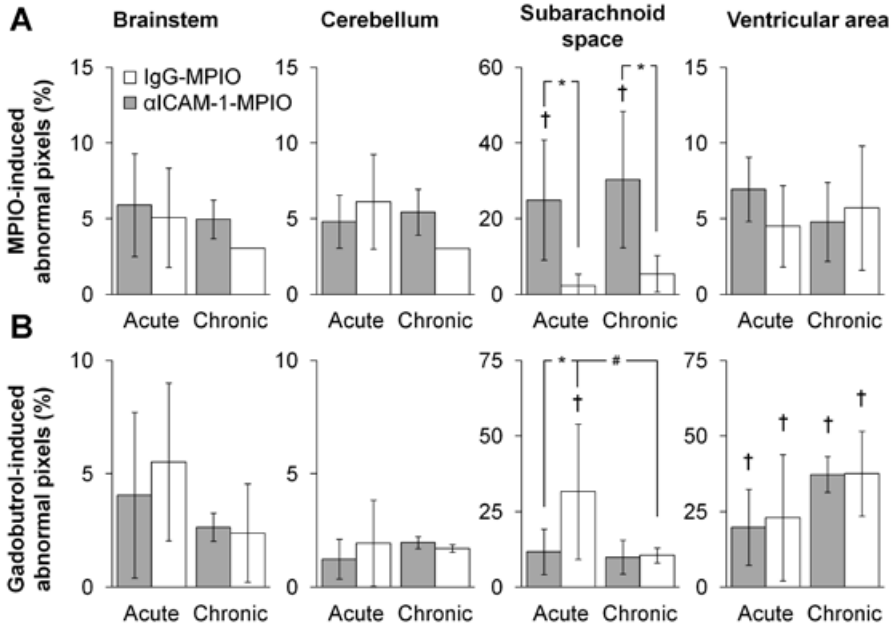

Figure 6.4

Quantification of abnormal pixels after injection of MPIO **(A)** or gadobutrol **(B)**. The percentage abnormal hypointense pixels (lower than mean minus two times standard deviation of the pixel intensity on the pre-injection images) was determined in specific ROIs (see **Figure 6.1**) at the different phases of disease. Specifically the subarachnoid space (note different scale of y-axis) between the midbrain and temporal lobe of the cortex showed clear presence of abnormal pixels after αICAM-1-MPIO injection. Abnormal hyperintense pixels, due to gadobutrol presence (higher than mean plus two times standard deviation of the pixel intensity on the pre-injection images) were mainly detected in the ventricular area († P < 0.05 versus pre injection levels; * P < 0.05 versus IgG; # P < 0.05 versus acute phase of disease).

6.4.4 IHC analyses Both IgG- and αICAM-1-MPIO-injected animals showed presence of MPIO in the spleen (data not shown). Similar to the MRI results, IHC showed that ICAM-1 was massively expressed on blood vessels in the subarachnoid space between the temporal cortex and the midbrain but also on many other vessels throughout the brain **(Figure 6.5)**. MR hypointensities of the αICAM-1-MPIO group coincided with ICAM-1 presence. Individual MPIO could be observed in these animals. Their presence co-localizes with ICAM-1-positive vessel-like structures. MPIO were mainly detected co-localized with cells located at the luminal side of these structures. No MPIO were detected deeper in the brain parenchyma. Also, no MPIO were detected in animals injected with IgG-MPIO (data not shown).

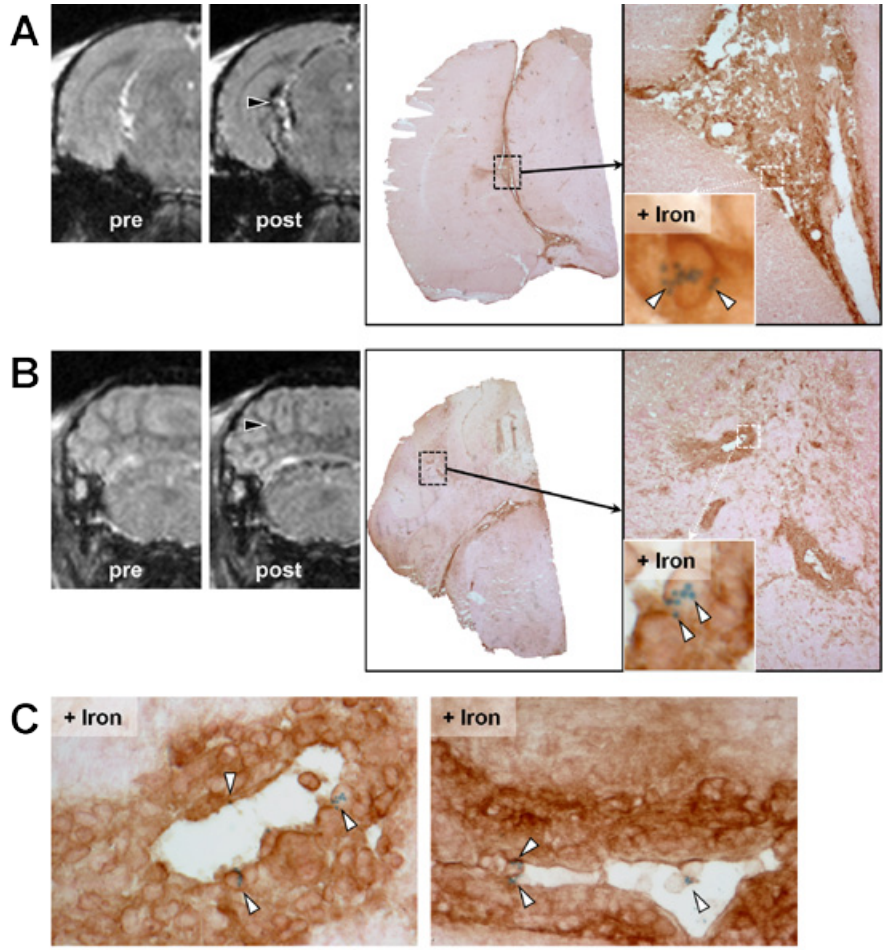

Figure 6.5.

Spatial comparison of αICAM-1-MPIO binding and ICAM-1 presence determined by IHC. Animal (EAE = 3)

injected with αICAM-1-MPIO. Corresponding T_2*-weighted 3D multi-gradient echo images and IHC ICAM-1-/MPIO images are displayed. IHC shows the localization of ICAM-1 (brown) on blood vessels in the subarachnoid space **(A)** or cerebellum **(B)**. Individual MPIO, as determined with Perls' staining (white arrowheads in the '+ Iron' insets), corresponded with the black arrowheads depicted in the post-contrast images, and were confined to ICAM-1-positive vessels. No MPIO were observed in the brain parenchyma, nor in animals injected with IgG-MPIO. **(C)** Typical examples of ICAM-1-positive blood vessels of animals injected with αICAM-1-MPIO showing MPIO presence (white arrow heads) in cells located at the luminal side of these vessels.

6.5 DISCUSSION

In this study, we showed that ICAM-1 mRNA and protein expression levels increased during the progression of EAE, and that this upregulation could be visualized, *in vivo*, with molecular MRI in an animal model of MS. To this end, MPIO conjugated to αICAM-1, an antibody for ICAM-1, were used. Specifically the area between the temporal lobe of the cerebrum and the midbrain showed presence of αICAM-1-MPIO, which was confined to ICAM-1-positive vessel-like structures. αICAM-1-MPIO presence was not necessarily associated with BBB damage. The upregulation of ICAM-1 mRNA levels on cerebellar capillaries of animals with manifest EAE, and the increased protein expression throughout the brain confirmed results found in literature in which the importance of ICAM-1 in early lesion formation during MS [16] or EAE [14-15] has been shown. ICAM-1 is an important imaging target and combined with our results, these data warrant the usage of an ICAM-1 conjugated MR contrast agent to detect this increased ICAM-1 presence in an animal model of EAE.

The current study is the first to explore if ICAM-1 presence can be detected *in vivo* during EAE using MRI. Previously, antibody-conjugated gadolinium-containing liposomes have been used to visualize ICAM-1 in EAE [24] and SPIO [25] have been used to visualize ICAM-1 in EAE. However, the presence of ICAM-1 was only explored with *post mortem* experiments. The only studies aimed to visualize ICAM-1 presence *in vivo* in EAE were preformed with ultrasound techniques, using ICAM-1 antibody conjugated microbubbles [26-27]. Image resolution of the used ultrasound technique was comparable with resolutions of our study. However, the precise spatial localization of ICAM-1 in the brain could not be determined as ultrasound does not provide anatomical information. Furthermore, it is unlikely that ultrasound can be used to study cerebral ICAM-1 presence in humans as the penetration depth of this imaging technique is limited. These disadvantages do not apply for MRI as MRI simultaneously provides anatomical detail of tissue and is in principle not limited by any penetration depth.

We showed that αICAM-1-MPIO were detected in cerebellum, the subarachnoid space between the temporal cortex and the midbrain, caudate putamen and cortical areas in the cerebrum at two characteristic phases of EAE, i.e., during the initial peak of the disease and at the chronic phase when animals showed some regression of disease. Quantification of abnormal pixel intensities showed that there was no difference between these two phases. No MPIO could be detected after administration of IgG-MPIO. Particularly the subarachnoid space between cortex and midbrain, an area richly fenestrated by blood vessels, showed massive αICAM-1-MPIO presence. This has also been reported using the above mentioned ultrasound techniques [27-28], however not for the antibody-conjugated paramagnetic gadolinium-containing liposomes [24]. VCAM-1 expression is also upregulated in this particular area, as has been shown with αVCAM-1-MPIO [13]. It is unclear what the involvement is of this specific area in the pathogenesis of EAE. Interestingly, beads of hypointensities were also observed in the ventricle, suggestive for αICAM-1-MPIO binding to the choroid plexus. An increase of ICAM-1 expression has been reported for epithelial cells during EAE [29], and it could suggest that this area may serve as an alternative entry site for circulating lymphocytes to enter the cerebrospinal fluid. The visualization of bands of MR hypointensities deep inside the cortical areas, which corresponded with vascular ICAM-1 identified by IHC, may be of special interest as cortical pathology has been re-recognized as an important feature in the pathology of MS. The *in vivo* visualization of cortical pathology with conventional MRI is hampered, although advances have been made using inversion recovery-based MR techniques [30]. MPIO-based MRI imaging of ICAM-1 presence in the cortex may therefore offer an attractive alternative tool to study cortical pathology in patients with MS.

The integrity of the BBB was examined with gadobutrol [31] and we observed that many αICAM-1-MPIO-positive areas were not associated with BBB damage. The vice-versa effect, i.e., gadobutrol leakage without MPIO presence, was only observed in the ventricular area. Similar results have been reported with αVCAM-1-MPIO injection [13]. Gadobutrol is a 'passive' agent and its presence in brain parenchyma is typically a result of a disrupted BBB. Apparently, endothelial activation of ICAM-1 and loss of BBB integrity are events that can be dissociated in time in EAE. This stresses the capability of the MPIO constructs to detect early events that are involved in lesion formation during MS. As a technical footnote it is important to mention that gadobutrol was injected after MPIO injection. Consequently, MPIO presence may adversely confound the detection of gadobutrol. However, we used T_1-weighted images with minimal $T_2^{(*)}$-weighting for gadobutrol detection. MPIO mainly exerts its effect on $T_2^{(*)}$-weighted images whereas the T_1 shortening effect is minimal [10]. Still, MPIO presence could be faintly observed on the

pre T_1-weighted gadobutrol images (data not shown) due to the strong T_2*-shortening effect even with the short echo times used (TE = 4 ms).

ICAM-1 associated with endothelial cells is most likely the main target for the αICAM-1-MPIO as we showed that ICAM-1 is robustly expressed on endothelial cells, and MPIO were mainly detected in cells which were confined to blood vessels. Similar to our present results, previous studies showed that ICAM-1-targeted MPIO are associated with CD31-expressing endothelial cells *in vivo*, and ICAM-1-specific binding to endothelial cells has been shown *in vitro* [10, 20]. However, ICAM-1 upregulation is not exclusive for endothelial cells during lesion formation in MS/EAE. Leukocytes also express ICAM-1, as has been reported before for macrophages [32], microglia [33], and T-cells [18]. Interestingly we have recently observed in an animal model of stroke that presence of αICAM-1-MPIO co-localizes with ICAM-1 as well as with CD45-positive leukocytes that are associated with blood vessels (**Chapter 5**). ICAM-1 expression has also been shown for epithelial cells of the choroid plexus [29], and astrocytes [33]. Whether αICAM-1-MPIO is able to visualize ICAM-1 expression on all of these cell types during EAE is unclear. In the current study, MR images were acquired within one hour after administration of MPIO. Given the extreme short half-life of MPIO and the fact that the BBB was not permeable for MPIO, it is unlikely that the post-αICAM-1-MPIO MR images visualize ICAM-1 presence on cells residing in the brain parenchyma, like astrocytes and microglia. However, next to ICAM-1-expressing endothelial cells, leukocytes present on the luminal side of the vasculature may also be labeled with ICAM-1-targeted MPIO in agreement with the results obtained in the animal model of stroke.

6.6 CONCLUSIONS

In conclusion, this study shows the feasibility of αICAM-1-MPIO to measure ICAM-1 presence in a rodent MS model, and specifically for MS it may be used for diagnosis of the early processes of lesion formation and grey matter pathology. For clinical application it is essential that MPIO will be developed which are fully biodegradable and non-toxic. The inert polymer coat of the MPIO used in this study hampers complete biodegradation of the MPIO, and it is most likely that they accumulate in the reticuloendothelial system of cells located in the liver and spleen [11]. Recently the first biodegradable MPIO have been developed and tested using FDA-approved polymers [34]. This opens the deployment of antibody-conjugated MPIO for clinical applications. Eventually, providing clinicians with tools to visualize endothelial activity will further guide them to diagnose MS earlier, but also to tailor and measure effectiveness of treatments for specific time windows and specific patient populations during MS.

6.7 REFERENCES

1. Wu GF, Alvarez E (2011) The immunopathophysiology of multiple sclerosis. Neurol Clin 29:257-278.
2. Lassmann H, Bruck W, Lucchinetti CF (2007) The immunopathology of multiple sclerosis: an overview. Brain Pathol 17:210-218.
3. Alvarez JI, Cayrol R, Prat A (2011) Disruption of central nervous system barriers in multiple sclerosis. Biochim Biophys Acta 1812:252-264.
4. Giovannoni G (2011) Promising emerging therapies for multiple sclerosis. Neurol Clin 29:435-448.
5. Deddens LH, Van Tilborg GA, Mulder WJ, De Vries HE, Dijkhuizen RM (2012) Imaging neuroinflammation after stroke: current status of cellular and molecular MRI strategies. Cerebrovasc Dis 33:392-402.
6. Oude Engberink RD, Blezer EL, Dijkstra CD, van der Pol SM, van der Toorn A, de Vries HE (2010) Dynamics and fate of USPIO in the central nervous system in experimental autoimmune encephalomyelitis. NMR Biomed 23:1087-1096.
7. Floris S, Blezer EL, Schreibelt G, Dopp E, van der Pol SM, Schadee-Eestermans IL, Nicolay K, Dijkstra CD, de Vries HE (2004) Blood-brain barrier permeability and monocyte infiltration in experimental allergic encephalomyelitis: a quantitative MRI study. Brain 127:616-627.
8. Vellinga MM, Vrenken H, Hulst HE, Polman CH, Uitdehaag BM, Pouwels PJ, Barkhof F, Geurts JJ (2009) Use of ultrasmall superparamagnetic particles of iron oxide (USPIO)-enhanced MRI to demonstrate diffuse inflammation in the normal-appearing white matter (NAWM) of multiple sclerosis (MS) patients: an exploratory study. J Magn Reson Imaging 29:774-779.
9. Jefferson A, Wijesurendra RS, McAteer MA, Choudhury RP (2012) Development and application of endothelium-targeted microparticles for molecular magnetic resonance imaging. Wiley Interdiscip Rev Nanomed Nanobiotechnol 4:247-256.
10. Deddens LH, Van Tilborg GA, Van der Toorn A, Paulis LE, Strijkers GJ, Storm G, Mulder WJ, De Vries HE, Dijkhuizen RM (2012) Micron-sized particles of iron oxide and gadolinium-containing liposomes as targeted contrast agent for molecular MRI of neuroinflammation after stroke: A comparative study. Proceedings International Society for Magnetic Resonance in Medicine 20: 1627P.

11. McAteer MA, Schneider JE, Ali ZA, Warrick N, Bursill CA, von zur Muhlen C, Greaves DR, Neubauer S, Channon KM, Choudhury RP (2008) Magnetic resonance imaging of endothelial adhesion molecules in mouse atherosclerosis using dual-targeted microparticles of iron oxide. Arterioscler Thromb Vasc Biol 28:77-83.

12. McAteer MA, Sibson NR, von Zur Muhlen C, Schneider JE, Lowe AS, Warrick N, Channon KM, Anthony DC, Choudhury RP (2007) *In vivo* magnetic resonance imaging of acute brain inflammation using microparticles of iron oxide. Nat Med 13:1253-1258.

13. Serres S, Mardiguian S, Campbell SJ, McAteer MA, Akhtar A, Krapitchev A, Choudhury RP, Anthony DC, Sibson NR (2011) VCAM-1-targeted magnetic resonance imaging reveals subclinical disease in a mouse model of multiple sclerosis. FASEB J 25:4415-4422.

14. Cannella B, Cross AH, Raine CS (1990) Upregulation and coexpression of adhesion molecules correlate with relapsing autoimmune demyelination in the central nervous system. J Exp Med 172:1521-1524.

15. Kithcart AP, Cox GM, Sielecki T, Short A, Pruitt J, Papenfuss T, Shawler T, Gienapp I, Satoskar AR, Whitacre CC (2010) A small-molecule inhibitor of macrophage migration inhibitory factor for the treatment of inflammatory disease. FASEB J 24:4459-4466.

16. Sobel RA, Mitchell ME, Fondren G (1990) Intercellular adhesion molecule-1 (ICAM-1) in cellular immune reactions in the human central nervous system. Am J Pathol 136:1309-1316.

17. Greenwood J, Heasman SJ, Alvarez JI, Prat A, Lyck R, Engelhardt B (2011) Review: leucocyte-endothelial cell crosstalk at the blood-brain barrier: a prerequisite for successful immune cell entry to the brain. Neu ropathol Appl Neurobiol 37:24-39.

18. Bullard DC, Hu X, Schoeb TR, Collins RG, Beaudet AL, Barnum SR (2007) Intercellular adhesion molecule-1 expression is required on multiple cell types for the development of experimental autoimmune encepha lomyelitis. J Immunol 178:851-857.

19. Morrissey SP, Deichmann R, Syha J, Simonis C, Zettl U, Archelos JJ, Jung S, Stodal H, Lassmann H, Toyka KV, Haase A, Hartung HP (1996) Partial inhibition of AT-EAE by an antibody to ICAM-1: clinico-histological and MRI studies. J Neuroimmunol 69:85-93.

20. Zhu Y, Ling Y, Zhong J, Liu X, Wei K, Huang S (2012) Magnetic resonance imaging of radiation-induced brain injury using targeted microparticles of iron oxide. Acta Radiol 53:812-819.

21. Kuijk LM, Klaver EJ, Kooij G, van der Pol SM, Heijnen P, Bruijns SC, Kringel H, Pinelli E, Kraal G, de Vries HE, Dijkstra CD, Bouma G, van Die I (2012) Soluble helminth products suppress clinical signs in murine experimental autoimmune encephalomyelitis and differentially modulate human dendritic cell activation. Mol Immunol 51:210-218.

22. Klein S, Staring M, Murphy K, Viergever MA, Pluim JP (2010) elastix: a toolbox for intensity-based medical image registration. IEEE Trans Med Imaging 29:196-205.

23. Kuerten S, Javeri S, Tary-Lehmann M, Lehmann PV, Angelov DN (2008) Fundamental differences in the dynamics of CNS lesion development and composition in MP4- and MOG peptide 35-55-induced experimental autoimmune encephalomyelitis. Clin Immunol 129:256-267.

24. Sipkins DA, Gijbels K, Tropper FD, Bednarski M, Li KC, Steinman L (2000) ICAM-1 expression in autoimmune encephalitis visualized using magnetic resonance imaging. J Neuroimmunol 104:1-9.

25. Schneider C, Schuetz G, Zollner TM (2009) Acute neuroinflammation in Lewis rats - a model for acute multiple sclerosis relapses. J Neuroimmunol 213:84-90.

26. Reinhardt M, Hauff P, Linker RA, Briel A, Gold R, Rieckmann P, Becker G, Toyka KV, Maurer M, Schirner M (2005) Ultrasound derived imaging and quantification of cell adhesion molecules in experimental autoimmune encephalomyelitis (EAE) by Sensitive Particle Acoustic Quantification (SPAQ). Neuroimage 27:267-278.

27. Linker RA, Reinhardt M, Bendszus M, Ladewig G, Briel A, Schirner M, Maurer M, Hauff P (2005) *In vivo* molecular imaging of adhesion molecules in experimental autoimmune encephalomyelitis (EAE). J Autoimmun 25:199-205.

28. Doerck S, Gobel K, Weise G, Schneider-Hohendorf T, Reinhardt M, Hauff P, Schwab N, Linker R, Maurer M, Meuth SG, Wiendl H (2010) Temporal pattern of ICAM-I mediated regulatory T cell recruitment to sites of inflammation in adoptive transfer model of multiple sclerosis. PLoS One 5:e15478.

29. Engelhardt B, Wolburg-Buchholz K, Wolburg H (2001) Involvement of the choroid plexus in central nervous system inflammation. Microsc Res Tech 52:112-129.

30. Geurts JJ, Barkhof F (2008) Grey matter pathology in multiple sclerosis. Lancet Neurol 7:841-851.

31. Uysal E, Erturk SM, Yildirim H, Seleker F, Basak M (2007) Sensitivity of immediate and delayed gadolinium-enhanced MRI after injection of 0.5 M and 1.0 M gadolinium chelates for detecting multiple sclerosis lesions. AJR Am J Roentgenol 188:697-702.

32. Hofmann N, Lachnit N, Streppel M, Witter B, Neiss WF, Guntinas-Lichius O, Angelov DN (2002) Increased expression of ICAM-1, VCAM-1, MCP-1, and MIP-1 alpha by spinal perivascular macrophages during experimental allergic encephalo-myelitis in rats. BMC Immunol 3:11.

33. Lee SJ, Benveniste EN (1999) Adhesion molecule expression and regulation on cells of the central nervous system. J Neuroimmunol 98:77-88.

34. Nkansah MK, Thakral D, Shapiro EM (2011) Magnetic poly(lactide-co-glycolide) and cellulose particles for MRI-based cell tracking. Magn Reson Med 65:1776-1785.

DISCUSSION

Based on:
Lisette H. Deddens, Geralda A.F. Van Tilborg, Willem J.M. Mulder, Helga E. De Vries and Rick M. Dijkhuizen.
Imaging neuroinflammation after stroke: current status of cellular and molecular MRI strategies.
Cerebrovasc Dis **2012** 33:392-402

07

7.1 A GUIDE TO SUCCESSFUL APPLICATION OF MOLECULAR MRI

This thesis describes the use of different MR contrast agent platforms for the direct detection of pathology-induced upregulation of intraluminally-expressed vascular entities by molecular MRI. We reported on the successful application of molecular MRI of tumor-induced angiogenesis with $\alpha_v\beta_3$-targeted iron oxide-containing nanoemulsions (**Chapter 2**), and stroke- and EAE-induced neurovascular inflammation with ICAM-1-targeted MPIO (**Chapters 4, 5, 6**), but also addressed less successful attempts of molecular MRI of stroke-induced angiogenesis by using PECAM-1-targeted MPIO (**Chapter 3**) and stroke-induced neurovascular inflammation using ICAM-1-targeted Gd-liposomes (**Chapter 4**). Based on our findings, it can be concluded that the key to successful application of molecular MRI seems to lie in the use of an appropriate contrast agent for the pathology of interest, directed to a well-chosen target and assessed with a fine-tuned MRI set-up.

7.1.1 Part I: An appropriate contrast agent The first challenge in molecular MRI is selection of an appropriate contrast agent. One of the aspects that hamper broad applicability of molecular MRI is low MR sensitivity. As compared to other molecular imaging modalities, such as PET, SPECT and optical imaging, molecular MRI requires relatively high amounts of contrast agent. Insufficient local accumulation, nanoparticle degradation and label dilution by cell division may lead to undetectable levels of MR contrast agent. This is particularly the case for Gd-chelates, which typically have a lower contrast efficacy than iron oxides. Furthermore, their T_1 effect is quenched upon compartmentalization in cells, thereby limiting their application [1-2]. One way to overcome this sensitivity issue is to use contrast agents with a high payload of MR contrast, as we have carried out in this thesis by using Gd-liposomes (**Chapter 4**), nanoemulsions (**Chapter 2**), and MPIO (**Chapters 3 – 6**). Nevertheless, this high payload of MR contrast did not always result in sufficient contrast-enhancement on MR images (**Chapter 4**), as other factors, such as intrinsic tissue contrast, may prevent successful detection.

An alternative MRI approach that could circumvent these difficulties involves the use of ^{19}F-containing particles, such as perfluorocarbon (PFC) emulsions, which have already been successfully applied for the *in situ* labeling of circulating monocytes [3]. ^{19}F is not endogenously present in biological tissues and ^{19}F MRI signal can consequently be perceived as a direct, quantitative measure of accumulated contrast agent [3-4]. However, ^{19}F MRI requires a specialized hardware setup and tailored imaging protocols, which is not presently available on every (pre)clinical MRI scanner.

7.1.2 Part II: The pathology of interest One of the other factors that further constrain molecular MRI, in addition to the relatively low potency of most agents to induce MR contrast, is the aforementioned intrinsic tissue contrast. Endogenous sources of MRI contrast, like edema, tissue damage, microbleeds or infiltrating leukocytes, may lead to deficient or erroneous detection of target-specific contrast accumulation [5]. One could anticipate on these endogenous sources of MR contrast by choosing the appropriate contrast agent. For example, MPIO that induce hypointensities would be of use when endogenous hyperintensities (e.g., caused by edema) are present on $T_2^{(*)}$-weighted images. However, MPIO might not be ideal when endogenous hypointensities (e.g., caused by bleeding) already persist (**Chapter 5**).

Endogenous tissue contrast is particularly complicating when pathology-induced changes take place between or during MRI acquisitions. When the presence of target-bound contrast agent is measured at a relatively long time after injection, endogenous changes that take place during this time can confound the detection of differences between pre- and post-contrast agent MR images, as described in **Chapter 4**. This is particularly problematic for agents with a long blood half-life, of which the unbound fraction needs to be cleared to allow specific detection. In case of tunable nanoparticles, such as lipophilic particles as discussed in the **Introduction**, shortening the blood half-life of a particle could be attained by changing the outer layer of the particle, e.g., by using a lower degree of PEGylation of lipophilic nanoparticles, resulting in a faster recognition by the mononuclear phagocyte clearance system [6-7]. Another method to decrease circulation times is the so-called avidin chase as described by Van Tilborg et al [8-9]. In this strategy, biotinylated lipids are introduced in the bilayer of the particle, which can subsequently be rapidly removed by an injection of avidin.

7.1.3 Part III: A well-chosen target Also important for the successful application of molecular MRI is the choice of the target of interest. When dealing with for instance leaky tumor vessels, contrast agent can easily extravasate and accumulate in the tumor tissue, which is known as the enhanced permeability and retention effect (EPR) [10]. Choosing a target that is expressed on endothelial cells, which is directly accessible

from the circulation, ensures a more specific targeting of functionalized MR contrast agent than the passive accumulation due to the EPR effect. When target expression is high, the specific targeting dominates the EPR effect at the tumor vasculature [11-12] (**Chapter 2**). This concept also applies to targeting of a neurovascular entity, although it needs to be considered that leakage over the blood-brain barrier is more restricted in time and size than in other types of vasculature.

Next to a high expression level, it is also of interest that the target is accessible for the injected contrast agent. Even though the target may be expressed on the intraluminal side of the vasculature, the exact location of expression could perturb effective binding. For example, PECAM-1 is expressed on endothelial cell intercellular junctions [13], and might not be accessible for a big construct as αPECAM-1-MPIO (**Chapter 3**). A high payload of contrast agent may therefore not lead to successful detection, as is demonstrated in this thesis, which shows that stroke-induced upregulation of cell adhesion molecules was effectively imaged by MRI with αICAM-1-MPIO (**Chapters 4 and 5**), but not with αPECAM-1-MPIO (**Chapter 3**).

Note must be taken with entities that are not only expressed on endothelial cells, but also on blood-borne cells. This opens up windows of opportunities to perform *in vivo* labeling of blood-borne cells and therefore widen the range of this molecular MRI approach (**Chapter 5**). However, increased expression on other types of cells might also lower the availability of contrast agent to the vascular component, thereby lowering its specific contrast efficacy (**Chapter 3**).

7.1.4 Part IV: A fine-tuned MRI set-up Successful application of molecular MRI is not only based on choosing the right target-specific contrast agent for a specific pathology, but is also dependent on appropriate MR acquisition and data analysis. It is recommended to perform phantom, *in vitro* and *in vivo* pilot studies in which MR parameters are set to maximize possible contrast effects generated by the targeted contrast agent. Increasing spatial resolution may allow the detection of lower numbers of particles due to decreased partial volume effects. However, to retain similar signal-to-noise ratios, acquisition times need to be increased, thereby creating a higher risk of movement artifacts during acquisition.

7.2 CLINICAL TRANSLATION

Molecular MRI can be of future use in the clinic to diagnose stages of disease that are not visible with conventional MR techniques, as suggested by Serres and co-workers [14] and **Chapter 6** of this thesis, and to directly monitor treatment efficacies at these early disease stages. The key to successful translation of molecular MRI to the clinic is availability of an effective and safe FDA-approved contrast agent. An FDA-approved contrast agent harbors non-toxicity and biodegradability and can preferably be administered multiple times to allow longitudinal monitoring of the disease process and assess the efficacy of novel treatments. The most commonly applied clinical MR contrast agents are the FDA-approved low molecular weight paramagnetic Gd-chelates, e.g., Gd-DTPA and Gd-DOTA [15-16], which could be used for molecular MRI purposes. Iron oxides have been approved for clinical use in the past, but it appears that none of these agents are currently available on the market, with the exception of the oral iron oxide contrast agent Lumirem/Gastromark™ [17]. However, synthesis of biodegradable MPIO may open the door to clinical applications of iron oxide-based contrast agent in the future [18].

7.3 FUTURE PERSPECTIVES

A potential innovative way for molecular MRI to monitor the onset of vascular remodeling at a very early stage, may be accomplished with MR reporter genes, which allow non-invasive assessment of expression of a gene of interest together with synthesis of an MR detectable by-product, such as endogenous paramagnetic ferritin [19-21].

Another promising strategy for molecular MRI involves the use of so-called responsive MR contrast agents. Breckwoldt et al [22] applied a Gd-based enzyme-activatable agent that induced enhanced T_1 relaxation upon reaction with myeloperoxidase (MPO) [23], an enzyme secreted by activated neutrophils and macrophages or microglia. The injection of this MPO-responsive agent in mice after endothelin-induced stroke resulted in prolonged contrast enhancement at the lesion site compared to conventional Gd-DTPA, which suggests that contrast enhancement resulted from additional MPO activity.

Currently, a shift towards multimodal imaging nanoprobes is noted, in which contrast agents not only generate contrast on MRI, but can also be detected with PET/SPECT, CT, ultrasound or optical imaging [24]. Combining these different methods can lead

to high contrast agent detection sensitivity combined with a high spatial resolution. The focus and future of molecular MRI should not only involve multimodal imaging nanoprobes, but should extend to multifunctional nanoprobes, so-called theranostic agents [25-27]. These probes combine a diagnostic contrast agent with a therapy solution in one single particle. When one or more theranostic agents have been FDA-approved, this may lead to a change in patient management whereby diagnosis and image-guided drug delivery can be performed in one procedure.

7.4 REFERENCES

1. Kok MB, Hak S, Mulder WJ, Van der Schaft DW, Strijkers GJ, Nicolay K (2009) Cellular compartmentalization of internalized paramagnetic liposomes strongly influences both T_1 and T_2 relaxivity. Magn Reson Med 61:1022-1032.
2. Terreno E, Geninatti Crich S, Belfiore S, Biancone L, Cabella C, Esposito G, Manazza AD, Aime S (2006) Effect of the intracellular localization of a Gd-based imaging probe on the relaxation enhancement of water protons. Magn Reson Med 55:491-497.
3. Flogel U, Ding Z, Hardung H, Jander S, Reichmann G, Jacoby C, Schubert R, Schrader J (2008) *In vivo* monitoring of inflammation after cardiac and cerebral ischemia by fluorine magnetic resonance imaging. Circulation 118:140-148.
4. Marsh JN, Hu G, Scott MJ, Zhang H, Goette MJ, Gaffney PJ, Caruthers SD, Wickline SA, Abendschein D, Lanza GM (2011) A fibrin-specific thrombolytic nanomedicine approach to acute ischemic stroke. Nanomedicine (Lond) 6:605-615.
5. Vandeputte C, Thomas D, Dresselaers T, Crabbe A, Verfaillie C, Baekelandt V, Van Laere K, Himmelreich U (2011) Characterization of the inflammatory response in a photothrombotic stroke model by MRI: implications for stem cell transplantation. Mol Imaging Biol 13:663-671.
6. Drummond DC, Meyer O, Hong K, Kirpotin DB, Papahadjopoulos D (1999) Optimizing liposomes for deli very of chemotherapeutic agents to solid tumors. Pharmacol Rev 51:691-743.
7. Woodle MC, Matthay KK, Newman MS, Hidayat JE, Collins LR, Redemann C, Martin FJ, Papahadjopoulos D (1992) Versatility in lipid compositions showing prolonged circulation with sterically stabilized liposomes. Biochim Biophys Acta 1105:193-200.
8. Van Tilborg GA, Mulder WJ, Van der Schaft DW, Reutelingsperger CP, Griffioen AW, Strijkers GJ, Nicolay K (2008) Improved magnetic resonance molecular imaging of tumor angiogenesis by avidin-induced clearance of nonbound bimodal liposomes. Neoplasia 10:1459-1469.
9. Van Tilborg GA, Strijkers GJ, Pouget EM, Reutelingsperger CP, Sommerdijk NA, Nicolay K, Mulder WJ (2008) Kinetics of avidin-induced clearance of biotinylated bimodal liposomes for improved MR molecular imaging. Magn Reson Med 60:1444-1456.
10. Matsumura Y, Maeda H (1986) A new concept for macromolecular therapeutics in cancer chemotherapy: mechanism of tumoritropic accumulation of proteins and the antitumor agent smancs. Cancer Res 46:6387-6392.
11. Kessinger CW, Togao O, Khemtong C, Huang G, Takahashi M, Gao J (2011) Investigation of *in vivo* targeting kinetics of alpha(v)beta(3)-specific superparamagnetic nanoprobes by time-resolved MRI. Theranostics 1:263-273.
12. Hak S, Helgesen E, Hektoen HH, Huuse EM, Jarzyna PA, Mulder WJ, Haraldseth O, Davies Cde L (2012) The effect of nanoparticle polyethylene glycol surface density on ligand-directed tumor targeting studied *in vivo* by dual modality imaging. ACS Nano 6:5648-5658.
13. Newman PJ (1997) The biology of PECAM-1. J Clin Invest 100:S25-29.
14. Serres S, Mardiguian S, Campbell SJ, McAteer MA, Akhtar A, Krapitchev A, Choudhury RP, Anthony DC, Sibson NR (2011) VCAM-1-targeted magnetic resonance imaging reveals subclinical disease in a mouse model of multiple sclerosis. FASEB J 25:4415-4422.
15. Aime S, Fasano M, Terreno E (1998) Lanthanide(III) chelates for NMR biomedical applications. Chem Soc Rev 27:19-29.
16. Laurent S, Elst LV, Muller RN (2006) Comparative study of the physico-chemical properties of six clinical low molecular weight gadolinium contrast agents. Contrast Media Mol Imaging 1:128-137.

17. Achiam MP, Chabanova E, Logager VB, Andersen LP, Thomsen HS, Rosenberg J (2008) MR colonography with fecal tagging: barium vs. barium ferumoxsil. Acad Radiol 15:576-583.

18. Nkansah MK, Thakral D, Shapiro EM (2011) Magnetic poly(lactide-co-glycolide) and cellulose particles for MRI-based cell tracking. Magn Reson Med 65:1776-1785.

19. Cohen B, Dafni H, Meir G, Harmelin A, Neeman M (2005) Ferritin as an endogenous MRI reporter for noninvasive imaging of gene expression in C6 glioma tumors. Neoplasia 7:109-117.

20. Genove G, DeMarco U, Xu H, Goins WF, Ahrens ET (2005) A new transgene reporter for *in vivo* magnetic resonance imaging. Nat Med 11:450-454.

21. Gilad AA, Winnard PT, Jr., van Zijl PC, Bulte JW (2007) Developing MR reporter genes: promises and pitfalls. NMR Biomed 20:275-290.

22. Breckwoldt MO, Chen JW, Stangenberg L, Aikawa E, Rodriguez E, Qiu S, Moskowitz MA, Weissleder R (2008) Tracking the inflammatory response in stroke *in vivo* by sensing the enzyme myeloperoxidase. Proc Natl Acad Sci U S A 105:18584-18589.

23. Chen JW, Querol Sans M, Bogdanov A, Jr., Weissleder R (2006) Imaging of myeloperoxidase in mice by using novel amplifiable paramagnetic substrates. Radiology 240:473-481.

24. Jarzyna PA, Gianella A, Skajaa T, Knudsen G, Deddens LH, Cormode DP, Fayad ZA, Mulder WJ (2010) Multifunctional imaging nanoprobes. Wiley Interdiscip Rev Nanomed Nanobiotechnol 2:138-150.

25. Pene F, Courtine E, Cariou A, Mira JP (2009) Toward theragnostics. Crit Care Med 37:S50-58.

26. Jokerst JV, Gambhir SS (2011) Molecular imaging with theranostic nanoparticles. Acc Chem Res 44:1050-1060.

27. Yoo D, Lee JH, Shin TH, Cheon J (2011) Theranostic magnetic nanoparticles. Acc Chem Res 44:863-874.

SUMMARY

This thesis describes the use of different MR contrast agent platforms for the direct detection of pathology-induced upregulation of intraluminally-expressed vascular entities by molecular MRI. We particularly focused on the *in vivo* target specificity and MR sensitivity of the agents. The biological targets of our molecular MRI approaches were associated with two types of vascular events that are critically involved in many pathologies; i.e., angiogenesis and neurovascular inflammation.

Chapter 1 introduces the main topic of this thesis: molecular MRI. Concepts as molecular imaging, MRI, MR contrast agents and molecular MRI of angiogenesis and neurovascular inflammation are explained to provide a basic understanding for the following chapters that describe our experimental studies.

In **Chapter 2**, we report on the successful application of iron oxide-containing nanoemulsions targeted to angiogenesis-associated $\alpha_v\beta_3$ integrin to monitor the angiogenic activity of two different xenograft tumor models with varying degrees of angiogenesis. In the case of highly vascularized tumors, contrast agent accumulation was more confined to the periphery of the tumors, where angiogenesis is predominantly occurring. This was in contrast to the situation in less vascularized tumors, where contrast was found throughout the tumor. This demonstrated that this targeted MR contrast agent platform can serve as an *in vivo* biomarker for angiogenesis phenotyping which could guide anti-angiogenesis treatment.

Chapter 3 reports on molecular MRI of angiogenesis associated with ischemic stroke pathology. In this study, PECAM-1-targeted MPIO were assessed for their use as contrast agent for molecular MRI of vascular remodeling after experimental stroke. Even though elevated levels of PECAM-1 were present in lesioned tissue, and *in vitro* essays showed effective labeling by αPECAM-1-MPIO, *in vivo* molecular MRI after stroke revealed no αPECAM-1-MPIO-based contrast enhancement. This was corroborated by absence of αPECAM-1-MPIO in *post mortem* brain tissue. This indicated that this molecular MRI approach is not invariably effective for MRI-based assessment of stroke-induced alterations in expression of cerebrovascular markers.

Assessment of the suitability of two ICAM-1-targeted MR contrast agents, i.e., based on Gd-liposomes or MPIO, for molecular MRI of upregulation of ICAM-1 after stroke, is described in **Chapter 4**. Both ICAM-1-targeted agents bound effectively to activated cerebrovascular cells *in vitro*, generating significant MRI contrast-enhancing effects. Direct *in vivo* MRI-based detection after stroke was only achieved with ICAM-1-targeted MPIO, although both contrast agents showed similar target-specific vascular accumulation. This study demonstrated the potential of *in vivo* MRI of post-stroke ICAM-1 upregulation, and signified target-specific MPIO as most suitable contrast agent for molecular MRI of cerebrovascular inflammation.

In **Chapter 5**, these ICAM-1-targeted MPIO were administrated at different time points post-stroke in mice to determine to what extent different stages of endothelial activation and leukocyte infiltration could be visualized. αICAM-1-MPIO were shown to be suitable for *in vivo* MRI of stroke-induced ICAM-1 expression on vascular endothelium and leukocytes at different stages after stroke in mice. However, contrast effects from endogenous blood remains significantly hampered the detection of co-localized MPIO at later time points.

In **Chapter 6** we explored if ICAM-1-targeted MPIO were able to reveal EAE-induced ICAM-1 upregulation with *in vivo* molecular MRI. ICAM-1-targeted MPIO-induced MR contrast was particularly detected in the subarachnoid space between the temporal lobe and the midbrain. These locations of ICAM-1-induced MR contrast were not necessarily associated with physical disruption of the BBB, which often forms the basis for clinical identification of MS lesions. This indicated its potential suitability as a new contrast agent to detect ongoing disease activity and the evaluation of treatment efficacy.

Chapter 7 concludes this thesis with a discussion on key elements to the successful application of molecular MRI, which involve choice of an appropriate contrast agent for the pathology of interest, directed to a well-chosen target and assessed with a fine-tuned MRI set-up. After FDA-approvement of these contrast agents, molecular MRI could be of future use in the clinic to diagnose stages of disease that are not visible with conventional MR techniques. Furthermore, innovative ways such as MR reporter genes, responsive MR contrast agents and especially multifunctional contrast agents, will broaden the clinical perspectives of molecular MRI.

SAMENVATTING

Dit proefschrift beschrijft het gebruik van verschillende MR contrastmiddelen voor het direct detecteren van door pathologie geïnduceerde opregulatie van intraluminaal geëxpresseerde vasculaire entiteiten door middel van moleculaire MRI. Onze focus lag voornamelijk op de doelgerichtheid en MR sensitiviteit van deze contrastmiddelen onder *in vivo* condities. Onze moleculaire MRI aanpak was gericht op twee typen vasculaire processen die nauw betrokken zijn bij veel ziektebeelden; angiogenese en neurovasculaire inflammatie.

Hoofdstuk 1 introduceert het onderwerp van dit proefschrift: moleculaire MRI. Concepten als moleculaire beeldvorming, MRI, MR contrastmiddelen en moleculaire MRI van angiogenese en neurovasculaire inflammatie worden uitgelegd om een basis te leggen voor de hieropvolgende hoofdstukken met experimentele studies.

In **Hoofdstuk 2** rapporten we over de succesvolle toepassing van ijzeroxide bevattende nanoemulsies die gericht zijn op angiogenese-geassocieerde $\alpha_v\beta_3$ integrine, om de angiogenetische activiteit van twee verschillende xenograft tumoren met variërende mate van angiogenese te monitoren. In het geval van sterk gevasculeerde tumoren, beperkte de opeenhoping van contrastmiddel zich tot de rand van de tumor, waar angiogenese voornamelijk plaatsvindt. Dit was in contrast met tumoren met een minder hoge vaatdichtheid, waar aanwezigheid van het contrastmiddel in de gehele tumor gevonden werd. Dit liet zien dat dit doelgerichte MR contrastmiddel kan dienen als een *in vivo* biomarker voor fenotypering van angiogenese wat een leidraad kan bieden voor anti-angiogenese behandeling.

Hoofdstuk 3 rapporteert over moleculaire MRI van angiogenese geassocieerd met ischemische beroerte. In deze studie werden op PECAM-1 gerichte MPIO getest op hun gebruik als contrastmiddel voor moleculaire MRI van vasculaire veranderingen na experimentele beroerte. Ondanks dat er verhoogde waarden van PECAM-1 aanwezig waren in geïnfarceerd weefsel, en *in vitro* assays effectieve labeling door αPECAM-1-MPIO lieten zien, maakte *in vivo* moleculaire MRI na een beroerte geen op αPECAM-1-MPIO gebaseerde contrastverhoging zichtbaar. Dit werd bevestigd door de afwezigheid van αPECAM-1-MPIO in *post mortem* hersenweefsel. Deze moleculaire MRI aanpak is dus niet altijd even effectief voor bepaling van veranderingen in de expressie van cerebrovasculaire markers na een beroerte.

Hoofdstuk 4 beschrijft de bepaling van de bruikbaarheid van twee op ICAM-1 gerichte MR contrastmiddelen; gebaseerd op Gd-liposomen of MPIO, voor moleculaire MRI van opregulatie van ICAM-1 na een beroerte. Beide op ICAM-1 gerichte middelen bonden effectief aan geactiveerde cerebrovasculaire cellen *in vitro*, waarbij een significant MRI contrastverhogend effect werd gegenereerd. Directe detectie met *in vivo* MRI na een beroerte werd alleen bereikt met ICAM-1-gerichte MPIO, alhoewel beide contrastmiddelen vergelijkbare doelgerichte vasculaire accumulatie lieten zien. Deze studie laat het potentieel van *in vivo* MRI zien om ICAM-1 opregulatie na een beroerte te detecteren en duidt aan dat doelgerichte MPIO het meest bruikbare contrastmiddel is voor moleculaire MRI van cerebrovasculaire inflammatie.

Hoofdstuk 5 beschrijft hoe we deze op ICAM-1 gerichte MPIO op verschillende tijdspunten na een beroerte hebben toegediend in muizen om te bepalen in welke mate verschillende niveau's van endothele activatie en leukocyten infiltratie zichtbaar gemaakt konden worden. Er werd aangetoond dat αICAM-1-MPIO bruikbaar zijn voor *in vivo* MRI van ICAM-1 expressie op vasculair endotheel en leukocyten in verschillende fasen na een beroerte in muizen. Echter, contrast effecten van endogene bloedrestanten hinderden de detectie van gecolocalizeerde MPIO op latere tijdspunten.

In **Hoofdstuk 6** hebben we bekeken of op ICAM-1 gerichte MPIO ook in staat waren om EAE geïnduceerde ICAM-1 opregulatie zichtbaar te maken met *in vivo* moleculaire MRI. MR contrast, geïnduceerd door op ICAM-1 gerichte MPIO, werd voornamelijk gedetecteerd in de subarachnoidale ruimte tussen de temporale kwab en het middenbrein. Deze locaties van door ICAM-1 geïnduceerd MR contrast waren niet noodzakelijkerwijs geassocieerd met fysieke disruptie van de bloed-hersen barrière, wat vaak de basis vormt voor klinische identificatie van MS laesies. Dit laat een potentiële toepassing zien als nieuw contrastmiddel voor het detecteren van de status van het ziektebeeld en de evaluatie van de effectiviteit van therapieën.

Hoofdstuk 7 concludeert dit proefschrift met een discussie over de sleutelelementen van de succesvolle toepassing van moleculaire MRI, waaronder de keuze van een geschikt contrastmiddel voor de specifieke pathologie, gericht op een goed gekozen doel, en de detectie met een selectieve MRI techniek. Na goedkeuring voor gebruik van deze contrastmiddelen in patiënten, kan moleculaire MRI in de toekomst toegepast worden voor klinische diagnoses die momenteel niet mogelijk zijn met conventionele MR technieken. Hierop voortbordurend kunnen innovatieve toepassingen als genetisch geïnduceerde MR signalen, responderende MR contrastmiddelen en in het bijzonder multifunctionele contrastmiddelen de klinische perspectieven van moleculaire MRI verbreden.

LIST OF PUBLICATIONS

PUBLISHED:

Lisette H. Deddens, Geralda A.F. van Tilborg, Annette van der Toorn, Helga E. de Vries and Rick M. Dijkhuizen. PECAM-1-targeted micron-sized particles of iron oxide as MRI contrast agent for detection of vascular remodeling after cerebral ischemia. *Contrast Media Mol Imaging* **2013** (in press)

Lisette H. Deddens, Geralda A.F. van Tilborg, Annette van der Toorn, Kajo van der Marel, Leonie E.M. Paulis, Louis van Bloois, Gert Storm, Gustav J. Strijkers, Willem J.M. Mulder, Helga E. de Vries and Rick M. Dijkhuizen. MRI of ICAM-1 upregulation after stroke: The importance of choosing the appropriate target-specific particulate contrast agent. *Mol Imaging Biol* **2013** (in press)

Peter A. Jarzyna, **Lisette H. Deddens**, Benjamin H. Kann, Sarayu Ramachandran, Claudia Calcagno, Wei Chen, Anita Gianella, Rick M. Dijkhuizen, Arjan W. Griffioen, Zahi A. Fayad and Willem J. M. Mulder. Tumor angiogenesis phenotyping by nanoparticle-facilitated magnetic resonance and near-infrared fluorescence molecular imaging. *Neoplasia* **2012** 14: 964-973

Lisette H. Deddens, Geralda A.F. Van Tilborg, Willem J.M. Mulder, Helga E. De Vries and Rick M. Dijkhuizen. Imaging neuroinflammation after stroke: current status of cellular and molecular MRI strategies. *Cerebrovasc Dis* **2012** 33:392-402

Peter R. Seevinck, **Lisette H. Deddens** and Rick M. Dijkhuizen. Magnetic resonance imaging of brain angiogenesis after stroke. *Angiogenesis* **2010** 13:101-111

Peter A. Jarzyna, Anita Gianella, Torjus Skajaa, Gitte Knudsen, **Lisette H. Deddens**, David P. Cormode, Zahi A. Fayad and Willem J. Mulder. Multifunctional imaging nanoprobes. Wiley *Interdiscip Rev Nanomed Nanobiotechnol* **2010** 2:138-150

IN PREPARATION:

Lisette H. Deddens, Geralda A.F. van Tilborg, Kajo van der Marel, Hedi Hunt, Annette van der Toorn, Max A. Viergever, Helga E. de Vries and Rick M. Dijkhuizen. Molecular MRI of ICAM-1 expression after experimental stroke: Imaging activated endothelium and infiltrating leukocytes.

Erwin L.A. Blezer, **Lisette H. Deddens**, Gijs Kooij, Joost Drexhage, Susanne M.A. van der Pol, Arie Reijerkerk, Rick M. Dijkhuizen and Helga E. de Vries. *In vivo* MR imaging of intercellular adhesion molecule-1 expression in an animal model of multiple sclerosis.

ACKNOWLEDGEMENTS - DANKWOORD

Hem alleen zij d'eer

CURRICULUM VITAE

Lisette Helene Deddens was born on the 3rd of July 1983 in Enkhuizen into the loving family of Geert and Corien Deddens. She grew up in Capelle aan den IJssel, enjoying life with her siblings Suzanne, Bart, Janine and Ruurt. In 2001, she graduated (cum laude) from secondary school at Wartburg College in Rotterdam. In the same year she started her bachelor in Chemistry at the University of Utrecht. After finishing this degree (cum laude) in 2004, she decided to take a year off from the regular tract to go to South Africa to join Operation Mobilisation and follow its missions discipleship training. In the fall of 2005 she picked up her studies again and started the Biomolecular Sciences master at the University of Utrecht. She joined the Department of Bio-Organic Chemistry, led by prof. dr. Hans Kamerling, for her major research project and her MSc thesis. She conducted her minor research project at Unilever R&D in Vlaardingen in the Advanced Measurement and Imaging Group of prof. dr. Hans-Gerd Janssen. Shortly after her graduation (cum laude) in 2007, she started her PhD project at the Image Sciences Institute of prof. dr. ir. Max Viergever at the University Medical Center Utrecht in the Biomedical MR Imaging and Spectroscopy group of dr. Rick Dijkhuizen, in close collaboration with prof. dr. Elga de Vries from the Molecular Cell Biology and Immunology department at the VU University Medical Center in Amsterdam. The results of this project are described in this thesis. In 2009, Lisette received a grant from the Dutch Foundation De Drie Lichten for a half year research visit in dr. Willem Mulder's laboratory at the Translational Molecular Imaging Institute at Mount Sinai School of Medicine in New York City, which resulted in the article presented in Chapter 2 of this thesis. Currently, she works as Field Application Scientist at FortéBio, a division of Pall Life Sciences.

This thesis describes the use of different MR contrast agent platforms for the direct detection of pathology-induced upregulation of intraluminally-expressed vascular entities by molecular MRI. We reported on the successful application of molecular MRI of tumor-induced angiogenesis with $\alpha_v\beta_3$-targeted iron oxide-containing nanoemulsions, and stroke- and EAE-induced neurovascular inflammation with ICAM-1-targeted MPIO, but also addressed less successful attempts of molecular MRI of stroke-induced angiogenesis by using PECAM-1-targeted MPIO and stroke-induced neurovascular inflammation using ICAM-1-targeted Gd-liposomes.